

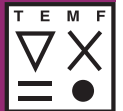
Quasi-3D Quench Simulation for Superconducting Accelerator Magnets

Zur Erlangung des akademischen Grades Doktor-Ingenieur (Dr.-Ing.)
Genehmigte Dissertation von Laura Anna Maria D'Angelo aus Dillenburg
Tag der Einreichung: 30.01.2023, Tag der Prüfung: 28.03.2023

1. Gutachten: Prof. Dr.-Ing. Herbert De Gersem
2. Gutachten: Dr.-Ing. Yvonne Späck-Leigsnering
3. Gutachten: Univ.Doz. Dr.-Ing. Stephan Russenschuck
Darmstadt, Technische Universität Darmstadt



TECHNISCHE
UNIVERSITÄT
DARMSTADT



Electrical Engineering and
Information Technology
Department

Institut für
Teilchenbeschleunigung
und Elektromagnetische
Felder (TEMF)

Theorie
Elektromagnetischer Felder

Quasi-3D Quench Simulation for Superconducting Accelerator Magnets

Accepted doctoral thesis by Laura Anna Maria D'Angelo

Date of submission: 30.01.2023

Date of thesis defense: 28.03.2023

Darmstadt, Technische Universität Darmstadt

Bitte zitieren Sie dieses Dokument als:

URN: urn:nbn:de:tuda-tuprints-231311

URL: <http://tuprints.ulb.tu-darmstadt.de/231311>

Jahr der Veröffentlichung auf TUprints: 2023

Dieses Dokument wird bereitgestellt von tuprints,
E-Publishing-Service der TU Darmstadt

<http://tuprints.ulb.tu-darmstadt.de>

tuprints@ulb.tu-darmstadt.de

Die Veröffentlichung steht unter folgender Creative Commons Lizenz:

Namensnennung – Weitergabe unter gleichen Bedingungen 4.0 International

<https://creativecommons.org/licenses/by-sa/4.0/>

This work is licensed under a Creative Commons License:

Attribution–ShareAlike 4.0 International

<https://creativecommons.org/licenses/by-sa/4.0/>

Erklärungen laut Promotionsordnung

§ 8 Abs. 1 lit. c PromO

Ich versichere hiermit, dass die elektronische Version meiner Dissertation mit der schriftlichen Version übereinstimmt.

§ 8 Abs. 1 lit. d PromO

Ich versichere hiermit, dass zu einem vorherigen Zeitpunkt noch keine Promotion versucht wurde. In diesem Fall sind nähere Angaben über Zeitpunkt, Hochschule, Dissertationsthema und Ergebnis dieses Versuchs mitzuteilen.

§ 9 Abs. 1 PromO

Ich versichere hiermit, dass die vorliegende Dissertation selbstständig und nur unter Verwendung der angegebenen Quellen verfasst wurde.

§ 9 Abs. 2 PromO

Die Arbeit hat bisher noch nicht zu Prüfungszwecken gedient.

Darmstadt, 30.01.2023

Laura Anna Maria D'Angelo

Kurzfassung

Numerische Feldsimulationen spielen eine wichtige Rolle für das Verständnis und die Vorhersage von Quenchereignissen in supraleitenden Beschleunigermagneten. Allerdings werfen sie dabei ein geometrisches wie auch physikalisches Multi-Skalen-Problem auf. So müssen bei der Modellierung der Beschleunigermagnete, die mehrere Meter lang sind, geometrische Details in der Größenordnung von Mikro- bis Millimetern aufgelöst werden. Ein Quenchereignis breitet sich in kürzester Zeit über mehrere geometrische Größenordnungen aus und beeinflusst die Eigenschaften des supraleitenden Materials dabei massiv. Eine volle dreidimensionale Finite-Elemente-Simulation mit ausreichender Genauigkeit des nichtlinearen magneto-thermischen Quenchverhaltens ist schlichtweg unmöglich.

Diese Dissertation präsentiert ein alternatives Vorgehen zur Berechnung und Analyse von dreidimensionalen Effekten, wie sie bei Quenchereignissen auftreten. Dazu wird eine zweidimensionale Finite-Elemente-Methode auf der transversalen Magnetquerschnittsfläche mit einer eindimensionalen Spektrale-Elemente-Methode auf Basis von orthogonalen Polynomen in longitudinaler Richtung kombiniert. Das Resultat ist eine quasi-dreidimensionale Methode mit hybriden Formfunktionen. Diese Methode wird zunächst formuliert, in einer objekt-orientierten Programmstruktur implementiert und anhand von Konvergenzstudien und Referenzsimulationen verifiziert. Für die Anwendung der Methode auf Quenchsimulationen wird dieses quasi-dreidimensionale Gerüst um dedizierte Quenchzustands- und Endwicklungsmodelle sowie Feld-Netzwerkkopplung, relevante Randbedingungen und effiziente nichtlineare Iterationsverfahren erweitert. Schließlich wird dieses quasi-dreidimensionale Simulationsverfahren für die nichtlineare magneto-thermisch stark gekoppelte Quenchsimulation von supraleitenden Kabeln und Magnetspulen angewandt. Vergleiche mit konventionellen dreidimensionalen Finite-Elemente-Lösern zeigen, dass das vorgestellte numerische Verfahren präzisere Ergebnisse liefert und dabei sehr viel weniger Rechenaufwand benötigt. Damit ist die entwickelte quasi-dreidimensionale Simulationsmethode ein wertvolles Werkzeug, um Quenchereignisse in supraleitenden Beschleunigermagneten zu analysieren.

Abstract

Numerical field simulation plays a crucial role in understanding and predicting quench phenomena in superconducting accelerator magnets. However, they impose a geometrical as well as physical multi-scale problem. A model of an accelerator magnet, which is several meters in length, has to resolve geometrical details in the order of micro- to millimeters. A quench propagates over several geometrical orders of magnitude in a very short time, massively affecting the properties of the superconducting material in the process. A full three-dimensional finite element simulation with sufficient accuracy of the nonlinear magneto-thermal quench behavior is therefore far beyond reach.

This dissertation presents an alternative approach to the calculation and analysis of three-dimensional effects arising in quench scenarios. To this end, a two-dimensional finite element method on the transversal magnet cross-section is combined with a one-dimensional spectral element method based on orthogonal polynomials in the longitudinal direction. The result is a quasi-three-dimensional method with hybrid shape functions. This method is formulated, implemented in an object-oriented program structure, and verified by convergence studies and reference simulations. For the application of the method to quench simulations, this quasi-three-dimensional framework is extended by dedicated quench state and end winding models as well as field-circuit coupling, relevant boundary conditions, and efficient nonlinear iteration procedures. Finally, this quasi-three-dimensional simulation approach is applied to the nonlinear magneto-thermal strongly coupled quench simulation of superconducting cables and coils. Comparisons with conventional three-dimensional finite element solvers show that the presented numerical method yields more accurate results while requiring much less computational effort. Thus, the developed quasi-three-dimensional simulation method is a valuable tool to analyze quenching scenarios in superconducting accelerator magnets.

Nomenclatura

Symbols

\vec{A}	Vs/m	magnetic vector potential
\hat{a}_e	Vs	line-integrated magnetic vector potential w.r.t. the e -th line
\vec{B}	T	magnetic flux density
B_{crit}	T	critical magnetic flux density
c_p	J/(kg K)	specific heat capacity
C_V	J/(m ³ K)	volumetric heat capacity
\vec{D}	As/m ²	electric displacement field
\mathcal{E}		number of edge degrees of freedom
\vec{E}	V/m	electric field strength
\vec{H}	A/m	magnetic field strength
H^1		Hilbert space
H_0^1		Hilbert space with compact support
i	A	current
\mathcal{J}		number of nodal degrees of freedom
\vec{J}	A/m ²	electric current density
J_{crit}	A/m ²	critical current density
\vec{J}_e	A/m ²	eddy current density
\vec{J}_m	A/m ²	magnetization current density
L_2		function space of square-integrable functions
L_q		Legendre polynomial of q -th order
LO_q		Lobatto polynomial of q -th order
ℓ_z	m	longitudinal length
\vec{M}	A/m	magnetization
N		maximal polynomial order
N_{FE}		number of finite elements

N_{SE}		number of spectral elements
N_j		nodal shape function for node j
\vec{n}		normal vector
\mathcal{P}_0^N		function space of orthogonal polynomials with maximal order of N
q_{qs}	1	quench state function
q_V	W/m^3	volumetric heat flux
\vec{r}	m	spatial coordinate
S	m^2	area
S_1^0		function space of first-order splines with compact support
T		triangular FE
T_q		Chebyshev polynomial of q -th order
t	s	time
V	m^3	volume, domain
V_h	m^3	computational domain
\mathcal{W}		number of half-turns
W	J	energy
$\vec{w}_j^{(\ell)}$		longitudinal edge shape function of edge j
$\vec{w}_e^{(t)}$		transversal edge shape function of edge e
u	V	voltage
α	$W/(m^2K)$	heat transfer coefficient
∂_n	1/m	partial derivative in normal direction
∂_t	1/s	partial derivative in time
∂_x	1/m	partial derivative in the spatial x -direction
∂_y	1/m	partial derivative in the spatial y -direction
∂_z	1/m	partial derivative in the spatial z -direction
Γ		boundary
ζ		Lagrange multiplier
ϑ	K	temperature
ϑ_{crit}	K	critical temperature
ϑ_{cs}	K	current sharing temperature
ϑ_{fluid}	K	temperature of the ambient fluid

λ	W/(mK)	thermal conductivity
μ	Vs/(Am)	magnetic permeability
μ_0	Vs/(Am)	vacuum permeability
ν	Am/(Vs)	magnetic reluctivity
$\vec{\xi}$	m^{-1}	voltage distribution function
ρ	Ωm	electric resistivity
ϱ_d	kg/m^3	density
σ	S/m	electric conductivity
τ	s	time constant
ϕ	V	electric scalar potential
ϕ_q		modified Lobatto polynomial of q -th order
∇	1/m	Nabla operator

Acronyms

1D	one-dimensional
2D	two-dimensional
3D	three-dimensional
BC	Boundary Condition
BVP	Boundary Value Problem
CAD	Computer-Aided Design
CLIQ	Coupling Loss Induced Quench
DoF	Degrees of Freedom
FE	Finite Element
FEM	Finite Element Method
IFCC	Interfilament Coupling Current
IFCL	Interfilament Coupling Loss
LHC	Large Hadron Collider
MNA	Modified Nodal Analysis
MQS	magnetoquasistatic
MVP	Magnetic Vector Potential
NbTi	Niobium-Titanium

Nb ₃ Sn	Niobium-Three-Tinn
PDE	Partial Differential Equation
Q3D	Quasi-three-dimensional
SE	Spectral Element
SEM	Spectral Element Method

Contents

1. Introduction	1
2. Fundamentals and Starting Point	5
2.1. Fundamentals of Superconductivity for Accelerator Magnets	5
2.2. Review of Numerical Techniques for Multi-Scale Problems	8
2.3. Scientific Contribution	11
3. Quench Modeling in Superconducting Coils	13
3.1. Lead Example	13
3.2. Magnetic Model	15
3.3. Thermal Model	18
3.4. Quench State Model	20
3.5. End Winding Models	21
4. Numerical Ingredients for the Q3D Method	23
4.1. Weak Formulation of the Magneto-Thermal Model	23
4.2. Discretization of the Magneto-Thermal Model	25
4.3. First Ingredient: 2D Finite Element Method	30
4.4. Second Ingredient: 1D Spectral Element Method	34
4.5. Seasoning: Field-Circuit Coupling	41
5. Quasi-3D Method for Quench Simulation	43
5.1. Quasi-3D Discretization of the Magneto-Thermal Model	43
5.2. Idiosyncrasies of the Quasi-3D Method	51
5.3. Quasi-3D Boundary Conditions	54
5.4. Implementation and Program Structure	58
6. Quasi-3D Quench Simulation Studies	63
6.1. Convergence Study	63
6.2. Thermal Simulation of Rutherford Cables	65
6.3. Magnetic Simulation of a Superconducting Cable	69
6.4. Quench Simulation of a Superconducting Multi-Filamentary Wire	72
6.5. Quench Simulation of a Superconducting Coil (Lead Example)	74
7. Summary, Conclusions and Outlook	79
7.1. Summary	79
7.2. Conclusions	80
7.3. Outlook	81
A. Matrix Calculations	83
A.1. 2D FE Matrices	83



A.2. 1D SE Modified Lobatto Matrices	87
B. Physical Data	89
B.1. Magnetic Properties	89
B.2. Thermal Properties	89
Bibliography	93
Danksagung	99
Scientific Contributions	101

1. Introduction

Man's relations to man do not captivate my fancy. It is man's relation to the cosmos – to the unknown – which alone arouses in me the spark of creative imagination.

H. P. Lovecraft

Why does our universe exist and what is its ultimate fate? How is our reality shaped by the Higgs mechanism, super-symmetry, extra dimensions, dark matter and dark energy? Particle accelerators play a key role in answering these existential questions and uncovering the secrets of the universe [Rus10]. For this on-going quest, higher and higher particle energies are striven for, which are necessary to make new discoveries [Qui19]. For example, although the existence of the Higgs boson had been already predicted in 1964, it was not until 2012 that the necessary particle energies could be generated to actually discover the Higgs boson at the Large Hadron Collider (LHC) at CERN [ATL12]. For future experiments, higher luminosities are currently sought at the LHC [Bor17].

Only superconducting magnets are able to provide the necessary high magnetic field strengths to keep such highly energized particles on the accelerator trajectory [Rus10]. Superconducting materials lose their electrical resistivity upon falling below a critical temperature, turning into the so-called superconducting state [BK13]. Then, they are able to carry high currents without generating any heat as opposed to normalconductors such as copper. With these high currents, magnet coils wound from superconducting cables are able to generate much stronger magnetic field strengths than conventional iron-based magnets could provide. These magnetic field strengths are needed to achieve higher particle energies [Rus10].

A major issue with superconducting magnets, however, is the quench phenomenon, which is a sudden shift from superconducting to normalconducting state upon surpassing the critical temperature [Wil83]. Although the superconducting magnets are constantly being cooled by a cryogenic cooling system based on liquid helium, local temperature increases can occur, e.g. due to manufacturing flaws, helium leaks in cooling pipes, power cuts or radiation [Ten13]. The quenched magnet regions, which are then normalconducting, begin to generate heat. This can lead to a domino effect: The normalconducting regions heat up the superconducting regions beyond the critical temperature, turning them also normalconducting and heating up more superconducting material, and so on, resulting into a thermal run-away.

The generated heat in a superconducting magnet correlates to its stored energy, which is very large. For example, the LHC main dipole magnet stores an amount of energy that is almost twice the energy released by an explosion of one kilogram of TNT, and which would be able to melt one liter of copper [Bru+04]. An uncontrolled quench could, therefore, lead to dramatic thermal consequences, in the worst case resulting into a partial melt-away of the magnet coil.

In the 80s and 90s, the quench behaviors of the superconducting magnets of the early accel-

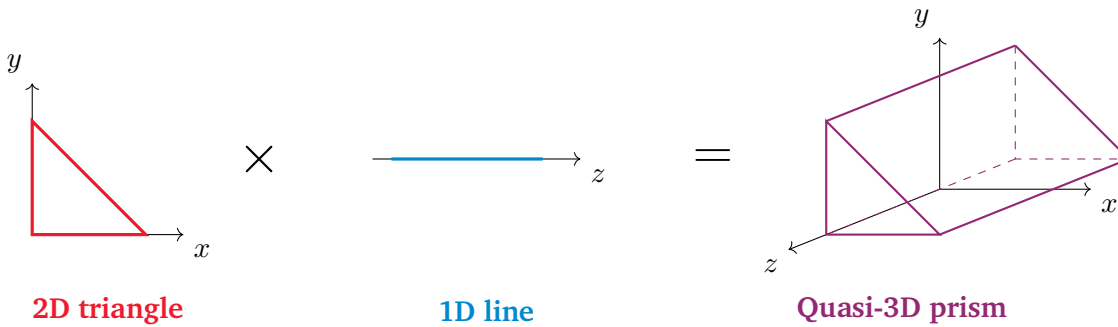


Figure 1.1.: Concept of the Q3D method in a Cartesian coordinate system. Triangular 2D elements are combined with 1D line elements, which results into Q3D prism elements.

erators such as HERA, SSC and RHIC have been estimated by manual calculations [Ten+88; He93; Mur+94]. Today, however, for an in-depth investigation of the quench phenomenon in superconducting accelerator magnets, analytical methods are out of question, as the problem is too complex to be solved manually on a piece of paper. Experimental analysis is also no viable option, since the construction cost of 1.5 to 2 million Euros per magnet [TTS18] is too high, and quench experiments of this magnitude are too dangerous. So, numerical simulations and computational engineering – also called the third paradigm of scientific discovery [Rüd+18] – play a crucial role in improving our understanding of the quench phenomenon, and consequently in designing more reliable and efficient protection systems for accelerator magnets.

However, the quench simulation of superconducting accelerator magnets presents computational engineers with a major challenge by its a multi-scale nature: While a typical accelerator magnet is very long (over 10 m), its diameter is only a fraction thereof (about 0.5 m). Many geometrical details on the micrometer and millimeter scale must be resolved [Bru+04], in particular, the quench phenomenon itself, which occurs on the scale of millimeters. Moreover, quench simulation is a highly multi-physical problem, for which one has to consider mutually-dependent thermal and electromagnetic phenomena as well as special superconducting effects and material characteristics [Rus10].

On the one hand, this makes a three-dimensional (3D) simulation approach simply unfeasible, as the computational costs would be vastly expensive. On the other hand, two-dimensional (2D) simulation approaches considering only the magnet cross-section are often too inaccurate and serve at most for an initial estimate of the quantities of interest [Jan+21].

This thesis contributes to closing the gap between too inaccurate 2D simulation approaches and too costly 3D simulation approaches by establishing a so-called quasi-3D (Q3D) simulation approach tailored for the quench simulation of superconducting accelerator magnets. To this end, a hybrid method is developed, which combines a 2D treatment of the transversal cross-section of the magnet with a one-dimensional (1D) treatment of its longitudinal dimension. More precisely, the geometrical details of the magnet cross-sections are resolved using triangular elements, while the quench phenomenon along the magnet is resolved by line elements. Their combination results into Q3D prism elements as shown in Fig. 1.1, which are able to reproduce the 3D physical effects in the magnet model very well. In this way, an adequate accuracy at reasonable computational costs is achieved, thus providing a remedy to the multi-scale problem of quench simulation of superconducting accelerator magnets.

Thesis Overview

The thesis is structured as follows. Chapter 1 provides an introduction to the challenges of quench simulation of superconducting accelerator magnets.

Chapter 2 summarizes the fundamentals of superconductivity in the context of superconducting magnet coils, and briefly discusses numerical methods and their suitability for the quench simulation of superconducting accelerator magnets. It also summarizes the scientific contributions of this work.

Chapter 3 introduces the magneto-thermal quench modeling for superconducting coils. After presenting a superconducting coil as lead example, the magnetic and thermal models are derived and a magneto-thermal coupling is introduced. A smooth quench state function modeling the transition between normal-conducting and superconducting state is developed based on the observations in [Bot14]. Lastly, end winding models are introduced, which cover for magnetic and thermal coil end effects.

Chapter 4 introduces the numerical ingredients needed for the construction of the Q3D method. First, the weak formulation of the magneto-thermal model is derived and general numerical discretization aspects are discussed, which are common to all numerical methods as the temporal discretization and the nonlinear iteration scheme. Then, the 2D finite element (FE) method (FEM) and the 1D spectral element (SE) method (SEM) are discussed. After an analysis of different orthogonal polynomials regarding their suitability for the Q3D method, the modified Lobatto polynomials, which were first formulated in [FD15], are introduced as optimal choice. Lastly, field-circuit coupling is briefly explained to be employed to connect the end windings of the superconducting coil to each other and to an external circuit.

Chapter 5 introduces the Q3D discretization approach for superconducting accelerator magnets, which is applied on the magneto-thermal model for quench simulation. The resulting systems of equations and all involved discrete quantities are derived. Subsequently, all boundary conditions relevant for quench simulation are discussed in the Q3D context. In the end, the implementation of the Q3D simulation approach as well as the program structure of a Q3D quench simulation tool are explained.

Chapter 6 presents the results of several Q3D quench simulation studies. First, the results of a convergence study are discussed, which verify the Q3D method. Second, the findings of a thermal simulation of a pack of Rutherford cables are presented [DCD20]. Third, superconducting effects in a superconducting cable are computed using a Q3D magnetic simulation [DD21]. Fourth, a quenching scenario in a single superconducting multi-filamentary wire is investigated employing a nonlinear magneto-thermal Q3D simulation approach [DSD22]. Fifth, the findings of a Q3D quench simulation of the superconducting coil previously introduced as lead example are presented.

Finally, conclusions are drawn in Chapter 7.

2. Fundamentals and Starting Point

"Begin at the beginning," the king said, gravely, "and go on till you come to the end; then stop."

Lewis Carroll, *Alice in Wonderland*

This chapter acquaints the reader with the relevant fundamentals on superconductivity regarding superconducting accelerator magnets, and provides a starting point for the Q3D simulation approach.

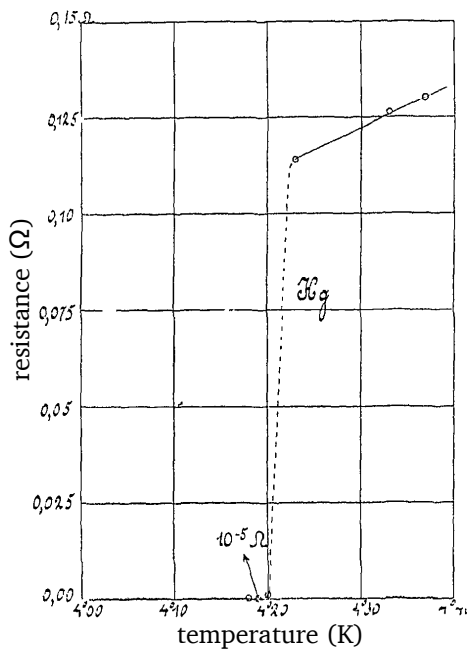
2.1. Fundamentals of Superconductivity for Accelerator Magnets

During cryogenic experiments with liquid helium in the year 1911, the Dutch physicist Heike Kamerlingh-Onnes observed that the electrical resistance of mercury jumps to exactly zero upon falling below a critical temperature of 4.2 K [Kam12], see Fig. 2.1a. With this, the phenomenon of superconductivity and the first superconducting material were discovered. In general, the state of a superconductor depends on the working point described by the parameter triple (ϑ, B, J) , where ϑ is the temperature in K, $B = |\vec{B}|$ is the magnitude of the magnetic flux density \vec{B} in T, and $J = |\vec{J}|$ is the magnitude of the electric current density \vec{J} in A/m² [BK13]. If the working point is below the so-called critical surface, which is defined by the critical temperature ϑ_{crit} , the critical magnetic flux density B_{crit} , and the critical electric current density J_{crit} (see Fig. 2.1b, purple surface), the superconductor is in the superconducting state, otherwise it is normalconducting [BK13].

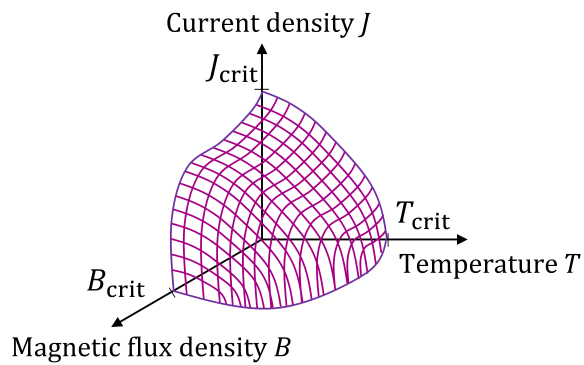
During the superconducting state, a superconductor is able to conduct currents without producing Joule losses. Furthermore, it exhibits perfect diamagnetism, i.e. an external magnetic field \vec{B}_{ext} is completely expelled from the superconductor as long as $|\vec{B}_{\text{ext}}| < B_{\text{crit}}$. This behavior contrasts with a hypothetical perfect conductor, which would freeze the magnetic field in its interior upon reaching a perfectly conducting state. This would lead to different outcomes depending on the previous history of the experiment [BK13]. A superconductor, however, always expels a magnetic field from its interior, regardless whether there already existed one when entering or leaving the superconducting state [BK13]. This is at least true for so-called superconductors of type I. For superconductors of type II, the perfect diamagnetism is hold to a first critical field $B_{\text{crit},1}$. For $B_{\text{crit},1} < |\vec{B}_{\text{ext}}| < B_{\text{crit},2}$, however, the superconductor enters the Shubnikov state, where it is penetrated by a grid of magnetic flux vortices [BK13]. To achieve this diamagnetism, screening currents are induced in the superconductor when exposed to a time-varying magnetic field. These currents generate a magnetization \vec{M} counteracting the external field variation [BK13].

The Quench Phenomenon

The sudden transition from the superconducting to the normalconducting state is called a quench [Wil83]. The quench phenomenon is a major issue in superconducting accelerator magnets,



(a) This historical plot by Heike Kamerlingh-Onnes shows the transition of mercury to the superconducting state upon falling below a critical temperature. Figure taken from [Kam12], axes added.



(b) The critical surface (purple) is spanned by the critical current density J_{crit} , the critical magnetic flux density B_{crit} and the critical temperature T_{crit} . Below this critical surface, a superconducting material is in superconducting state, otherwise it is normalconducting. Beware that the J -axis is scaled logarithmically.

Figure 2.1.: Upon reaching the superconducting state, the electrical resistance instantaneously vanishes (a). This transition depends on the electrical current density, the magnetic flux density and the temperature (b).

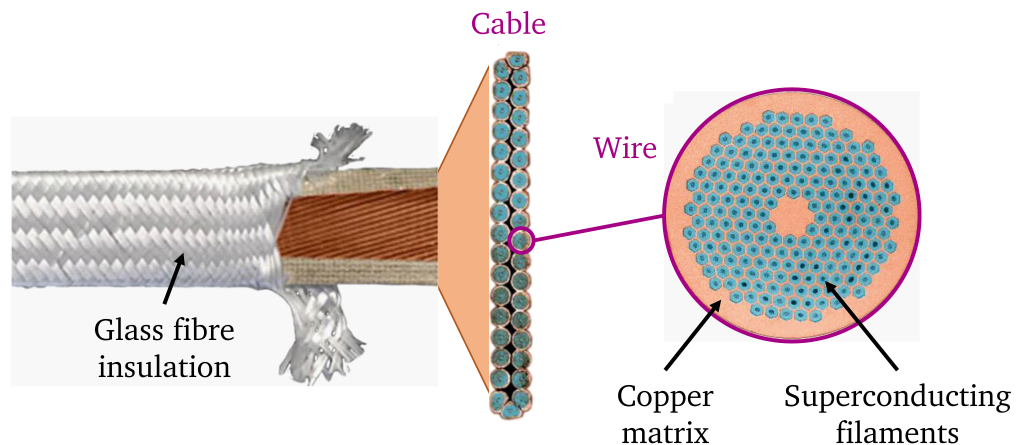


Figure 2.2.: At the left, a Rutherford cable is shown which features multiple wires and is wrapped up in a glass fibre insulation. At the center, the cross-section of the Rutherford cable is shown. At the right, the cross-section of a single wire is seen, consisting of several superconducting filaments embedded in copper. Pictures adapted from [SZ19].

since the affected regions begin to produce Joule losses, i.e. heat losses. These losses are typically very high due to the high currents applied to the magnets. During continuous operation, quench phenomena arise locally and may vanish due to cooling. In the worst case, however, a quench can lead to a thermal run-away resulting into extensive damages or even the destruction of the magnet coil. Hence, a reliable quench protection system is mandatory, which is triggered upon quench detection, i.e. when predefined voltage or resistance thresholds are exceeded [Ste+19]. Today, these thresholds are equipped with a large safety margin leading to frequent and unnecessary shutdowns, which considerably reduce the availability of the whole accelerator machine due to false triggers [Apo15]. To reduce their amount and therefore increase the availability of the accelerator, quench phenomena need to be understood better and the quench detection has to get preciser.

The Interfilament Coupling Phenomenon

The superconducting coils used in accelerator magnets are made of superconducting multi-filamentary cables such as Rutherford-type cables [Bru+04]. Figure 2.2 shows the structure of such a cable: It has a flattened form and consists of compacted multi-filamentary wires, in which approx. 10^5 superconducting filaments made of Niobium-Titanium (NbTi) or Niobium-Three-Tinn (Nb_3Sn) are embedded in a copper matrix [SZ19] for thermal stability reasons [Ver95]. The cable is wrapped up by a thin glass fibre insulation.

If the filaments were embedded in vacuum, the filaments would be electrically isolated from each other. Then, the external magnetic field would induce screening currents into each filament separately, which generate a magnetization completely compensating for the external field in the interior of the filament. This behavior is shown in Fig. 2.3a, where the transversal cross-section of three superconducting filaments in a non-conducting medium with electrical conductivity $\sigma = 0$ is seen. The external magnetic flux density \vec{B}_{ext} induces screening currents, which are shown in blue and red for the major in-coming and out-coming current part, respectively, and in purple for the minor transversal current part. This screening current distribution yields a magnetization \vec{M}

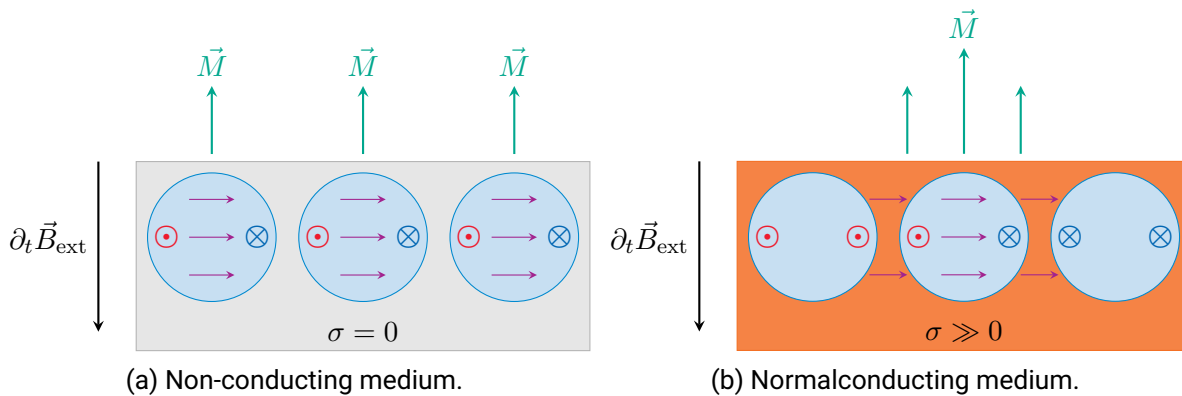


Figure 2.3.: Behavior of the screening currents in superconducting filaments (blue) in the case of a non-conducting medium (gray) and of a normalconducting medium (orange), respectively, when an external magnetic flux density (black arrow) is applied. The symbols \odot and \otimes indicate whether a current flows from the paper plane to the observer or vice versa, respectively. The purple arrows illustrate the transversal flow of the screening currents. Green arrows indicate the magnetization yielded by the respective screening current distribution.

for each filament as shown in Fig. 2.3a.

However, copper is a normalconducting medium with a high electrical conductivity $\sigma \gg 0$. As a consequence, a part of the induced screening currents in the filaments migrates through the copper medium into the other filaments, causing the filament currents to couple with each other. These currents are called interfilament coupling currents (IFCCs) [Ver95]. Figure 2.3b shows this phenomenon, which leads to a different current distribution and, thus, magnetization distribution compared to the non-conducting case in Fig. 2.3a. Furthermore, it causes heat losses in form of interfilament coupling losses (IFCLs) [Ver95]. During normal operation, these heat losses are disadvantageous, but in case of a quench, they can be exploited to heat up the entire magnet as done in the quench protection system CLIQ [Rav+14]. Similarly, interstrand coupling currents occur between the strands of a superconducting cable and also lead to heat losses [Ver95]. For the quench simulation, it is, therefore, important to take these phenomena into account.

2.2. Review of Numerical Techniques for Multi-Scale Problems

As discussed in Chapter 1, the quench simulation of superconducting accelerator magnets is particularly challenging for computational engineers due to the imposed multi-scale and multi-physical properties of the problem. For example, Fig. 2.4a shows the cross-section of the LHC main dipole, which is around 0.5 m wide. It consists of an iron yoke around two beam pipes, which are surrounded by a superconducting coil configuration. In Fig. 2.4b, a part of the superconducting coil is seen, where the white rectangles represent superconducting cables and the black trapezoids are copper keystones, which contribute to the shape of the coil. Three superconducting cables are shown in detail in Fig. 2.4c. They are wrapped by a glass fibre insulation (thick black lines), and consist by several superconducting multi-filamentary wires (circles). In these wires, a multitude of superconducting filaments are embedded, whose dimensions are on the scale of micrometers.

Obviously, the magnet shown in Fig. 2.4 features many geometrical details, which are on the

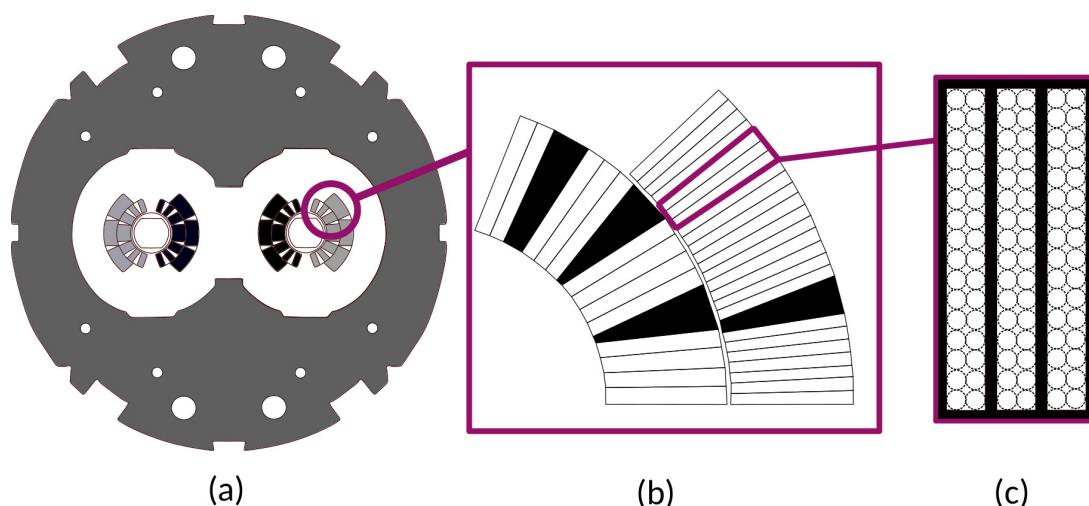


Figure 2.4.: The cross-section of the LHC main dipole (a) consists of an iron yoke around two beam pipes, which are surrounded by superconducting coils [Bru+04]. The coil configuration (b) consists of superconducting cables (white) and copper keystones (black) [Ver95]. The cables (c) are wrapped by a glass fibre insulation (thick black lines), and consist of several superconducting multi-filamentary wires (circles).

scale of millimeters, and also the quench phenomenon occurs on the scale of millimeters. Moreover, the superconducting filaments in a wire are on the scale of micrometers, see Fig. 2.2. At the same time, this magnet is over 10 m long [Bru+04]. A numerical method for quench simulation has to overcome this high ratio between the spatial dimensions of superconducting accelerator magnets. In the following, selected numerical methods and modeling approaches are introduced and their suitability for tackling this multi-scale challenge is discussed.

Homogenization Approaches

Homogenization approaches are modeling techniques used to handle spatial scales of different magnitudes, on which physical phenomena occur. In the simplest realization, geometrical objects in a certain scale of magnitude are not modeled explicitly, but the related physical effects are included into the model in a mathematical way. For example, the superconducting filaments in a superconducting wire, which are on the scale of micrometers, are typically not modeled explicitly, but the wires are homogenized to a bulk material with averaged material properties [Bor+18]. The IFCCs arising in the wire are then included into the model by an additional magnetization term in the magnetic formulation based on the characteristic time constant for the IFCC phenomenon [Ver95]. In this way, the micrometer scale is removed from the model, thus greatly reducing the computational effort for the simulation of the superconducting cable at the cost of modeling accuracy. While this approach works well for the superconducting filaments and the IFCC phenomenon, the quench phenomenon cannot be dealt with by such a homogenization approach.

Finite Element Methods

Finite element (FE) methods (FEM) are nowadays widely used in several commercial and open-source simulation softwares, e.g. [COM], [Das19] and [DG19]. They have been first applied in

1956 in structural mechanics and aeronautical sciences [Tur+56]. The idea is to subdivide the computational domain into multiple elements, creating a mesh on whose entities the solution is computed. In this way, the geometrical complexity of the magnet's cross-section can be very well resolved by FEs. In the context of the FEM, a mesh of high quality is quasi-uniform, i.e. the elements are roughly the same size, or at least the mesh size varies only gradually over the domain [Bra12]. Considering the geometrical details in the magnet's cross-section and the small quench phenomenon size along the magnet's length, the use of a three-dimensional (3D) FEM would lead to a very fine discretization of the domain and, thus, to unreasonably long computational times and extraordinary high demands for computational memory [Tro+19]. Hence, the computational domain is often reduced to the two-dimensional (2D) magnet cross-section. This simplified 2D cross-sectional model is then solved much more computationally efficient than the complex 3D model [Bor+18]. Naturally, the neglect of the longitudinal dimension leads to inaccurate simulation results. This is especially true for self-protected superconducting magnets, where the stored energy has to be dissipated within the magnet coils [Jan+21]. In this case, it is absolutely essential to take the thermal diffusion and quench development in all three spatial dimensions into account [Jan+21].

Spectral Element Methods

Another class of numerical methods are spectral methods. They use global higher-order basis functions to resolve the solution on a simple reference domain such as a line, a quadrangle or a cuboid [Can+06]. The original domain has to be mapped on this reference domain, which gets more complicated the more complex the original domain is. In 1984, following the idea of the FEM, the method has been expanded on several elements, which lead to the spectral element (SE) method (SEM) [Pat84]. The idea is to divide the complicated geometry in multiple domains, which in turn can be mapped easier on the reference entity [Kop09]. The quench phenomenon along the magnet's length could be resolved very well in this way. Still, the cross-section of an accelerator magnet consists of too many details to construct an efficient 3D SEM for the purpose of quench simulation.

Quasi-3D Methods

So-called quasi-3D (Q3D) methods combine the benefits of the FEM and SEM. To this end, a symmetry plane of the model is exploited to reduce the 3D geometry to a 2D cross-section, on which a 2D FEM is applied. In the third spatial dimension, a 1D SEM is employed to take asymmetrical physical effects and material distributions into account. This approach has similarities to anisotropic p -refinement [OB90], graded meshing [ASW96], and FEMs utilizing prismatic FEs and anisotropic hp -refinement [Jor+12]. In the latter case, the discretization is primarily h -refined in the xy -plane, while being p -refined in z -direction [Jor+12]. In comparison, Q3D methods have the advantages that the SE discretization converges exponentially (instead of only polynomially) and that the Q3D matrices can be assembled very efficiently thanks to their natural Kronecker tensor product structure.

In previous works of the author, a rotational Q3D method using axisymmetrical 2D FE in the cross-sectional plane and trigonometrical functions in the azimuthal direction has been utilized successfully for the simulation of cylindrical induction-heating devices [DD17] and high-voltage arresters [DSD19]. For the case of superconducting accelerator magnets, this thesis develops a translational Q3D method, where the transversal cross-section is discretized with a 2D FEM

and the longitudinal direction is resolved by a 1D SEM using orthogonal polynomials, resulting into Q3D prism elements, see Fig. 1.1. Herein, a 2D triangular FE in the xy -plane is combined with a 1D SE line in the z -direction, yielding a Q3D prism in the 3D space. This numerical simulation approach is very well suited to tackle the multi-scale problem of quench simulation of superconducting accelerator magnets and is the focus of this thesis.

2.3. Scientific Contribution

The scientific contributions of this thesis are summarized as follows. A list of related journal publications and conference contributions is found in the curriculum vitae in the appendix.

Derivation & Construction of Efficient Q3D Nodal and Edge Formulations

The Q3D formulations are derived for the thermal problem based on the heat conduction equation and the magnetic problem based on the magnetoquasistatic equation, respectively. The discrete quantities are written out in terms of the reference element approach [Bra12] for nodal and edge elements. Furthermore, the Q3D discrete quantities are brought to a Kronecker tensor product form allowing for a concise notation and an efficient assembly.

Different orthogonal polynomial bases are analyzed and compared to each other in regard to their suitability for the longitudinal component of the Q3D method. Finally, the modified Lobatto polynomials [FD15] are selected, for which this thesis proposes an efficient nonlinear iteration scheme to tackle the strongly coupled co-simulated nonlinear magneto-thermal problem.

Establishment of a Q3D Simulation Approach for Quench Simulation

A complete Q3D simulation approach including nonlinear material characteristics, multi-physical coupling, field-circuit coupling, the IFCC phenomenon and relevant boundary conditions is established for the quench simulation of superconducting coils. For the sharp transition between superconducting and normalconducting state, a smooth quench state model is developed based on the current sharing phenomenon in multi-filamentary superconducting cables and related observations regarding the maximum heat loss density [Bot14].

Implementation & Numerical Verification of the Q3D Simulation Approach

The Q3D simulation approach is implemented in an object-oriented programming framework in MATLAB [MAT20], for which a suitable software structure is developed. The Q3D method is numerically verified by consistency checks, convergence studies and 3D reference simulations. Several functionalities for a convenient setup, efficient execution and diverse post-processing of a quench simulation are implemented.

Application to Quench Simulation & Comparison to 3D Simulation Approaches

The proposed Q3D simulation approach is applied successfully to several quenching scenarios, and compared against 3D reference simulations. The implemented simulation studies include thermal and magnetic simulations of superconducting multi-filamentary cables as well as coupled magneto-thermal quench simulations of superconducting cables and coils.

3. Quench Modeling in Superconducting Coils

Mercury has passed into a new state, which on account of its extraordinary electrical properties may be called the superconductive state.

Heike Kamerlingh-Onnes

Quench simulation requires the modeling of multiple effects as it involves mutually-dependent electromagnetic and thermal phenomena. To this end, this chapter acquaints the reader with the relevant physics, and presents the mathematical models which have to be solved numerically.

3.1. Lead Example

A superconducting coil consists of a number of \tilde{W} windings, which are wound back and forth in longitudinal direction, see Fig. 3.1. To apply the Q3D method for the simulation of such coils, the end windings are neglected in a first step, since they obviously break the translational symmetry requirement of the method, see Fig. 3.1, where the Q3D domain is marked in purple. This is a valid approximation, if the coil is very long compared to its diameter, which is typically the case for dipole and quadrupole accelerator magnets [Sch10]. Since the goal of the Q3D method is to reproduce 3D effects as accurately as possible, the coil end effects are taken into account nonetheless by separate end winding models, see Sec. 3.5.

In the following, the Q3D model of a superconducting coil with $\tilde{W} = 12$ windings and a length of ℓ_z in m will serve as a lead example, see Fig. 3.2. Instead of counting full windings, the number $\mathcal{W} = 2\tilde{W}$ of half-turns is counted, which is the number of direction reversals of the cable. This number coincides with the number of cable cross-sections seen in the xy -plane of the Q3D model, and is $\mathcal{W} = 24$ for the lead example seen in Fig. 3.2.

Domain Notation

Figure 3.2 shows the notation of the individual volumes and boundaries of the lead example. Herein, the cable volumes are denoted with V_w , $w = 1, \dots, \mathcal{W}$ and are wrapped by a thin glass fibre insulation V_{ins} . Together, they form the coil, which is placed in a vacuum domain V_0 . The total domain is denoted with $V = V_0 \cup V_{\text{ins}} \cup V_w$, $w = 1, \dots, \mathcal{W}$ and its boundary consists of non-overlapping surfaces $\Gamma_{\text{Dir}} \cup \Gamma_{\text{Neum}} \cup \Gamma_w^+ \cup \Gamma_w^- = \partial V$, $w = 1, \dots, \mathcal{W}$, where Γ_w^+ and Γ_w^- denote the front and back surfaces of the cables V_w . In V , the magnetic problem is solved, see Sec. 3.2. The thermal model is computed in a sub-domain of $V \supset V' = V_{\text{ins}} \cup V_w$, $w = 1, \dots, \mathcal{W}$ with non-overlapping surfaces $\Gamma_{\text{iso}} \cup \Gamma_{\text{adi}} \cup \Gamma_{\text{con}} \cup \Gamma_w^+ \cup \Gamma_w^- = \partial V'$, $w = 1, \dots, \mathcal{W}$, excluding the vacuum domain. The convection effects of the liquid helium flowing around the coil are considered by applying Robin boundary conditions on Γ_{con} , see Sec. 3.3.

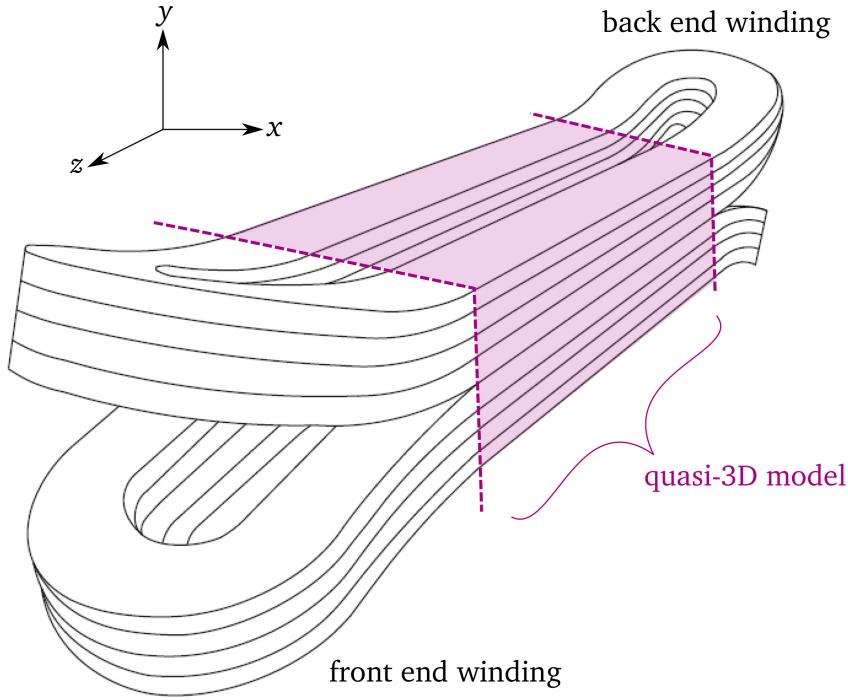


Figure 3.1.: Sketch of a 3D superconducting magnet coil. The central geometry fulfills the translational symmetry requirement, and serves as Q3D model. The coil end effects are modeled separately. Figure adapted from [SZ19].

Homogenization Approach

A single wire of a superconducting multi-filamentary cable (see Fig. 2.2) has a diameter of 0.1-3 mm, and consists of around 10^5 superconducting filaments with a diameter in the range of 1-20 μm [SZ19]. Obviously, an explicit discretization of the individual wires, let alone the filaments, is not a feasible option in terms of computational costs. Hence, a homogenization approach is employed, where the cable cross-section is homogenized to a bulk taking the proportions of the different materials into account [Bor+18]. To this end, a copper-to-superconductor-ratio parameter $\kappa_{\text{Cu}/\text{SC}}$ is defined, such that the effective value for an arbitrary material property X in a cable is given as

$$X_{\text{eff}} = \frac{|S_{\text{wire}}|}{|S_w|} \left(\frac{\kappa_{\text{Cu}/\text{SC}}}{\kappa_{\text{Cu}/\text{SC}} + 1} X_{\text{Cu}} + \frac{1}{\kappa_{\text{Cu}/\text{SC}} + 1} X_{\text{SC}} \right), \quad (3.1)$$

where X_{Cu} and X_{SC} stand for the respective material characteristics of copper and the superconducting material, respectively [Bor+18]. Furthermore, $|S_{\text{wire}}|$ denotes the wire cross-section area and $|S_w|$ the w -th half-turn cross-section area, such that the factor $\frac{|S_{\text{wire}}|}{|S_w|}$ represents the ratio of wire-to-vacuum-material in the cable [Bor+18]. Then,

$$\kappa_{\text{Cu}} = \frac{|S_{\text{wire}}|}{|S_w|} \frac{\kappa_{\text{Cu}/\text{SC}}}{\kappa_{\text{Cu}/\text{SC}} + 1}, \quad (3.2)$$

$$\kappa_{\text{SC}} = \frac{|S_{\text{wire}}|}{|S_w|} \frac{1}{\kappa_{\text{Cu}/\text{SC}} + 1} \quad (3.3)$$

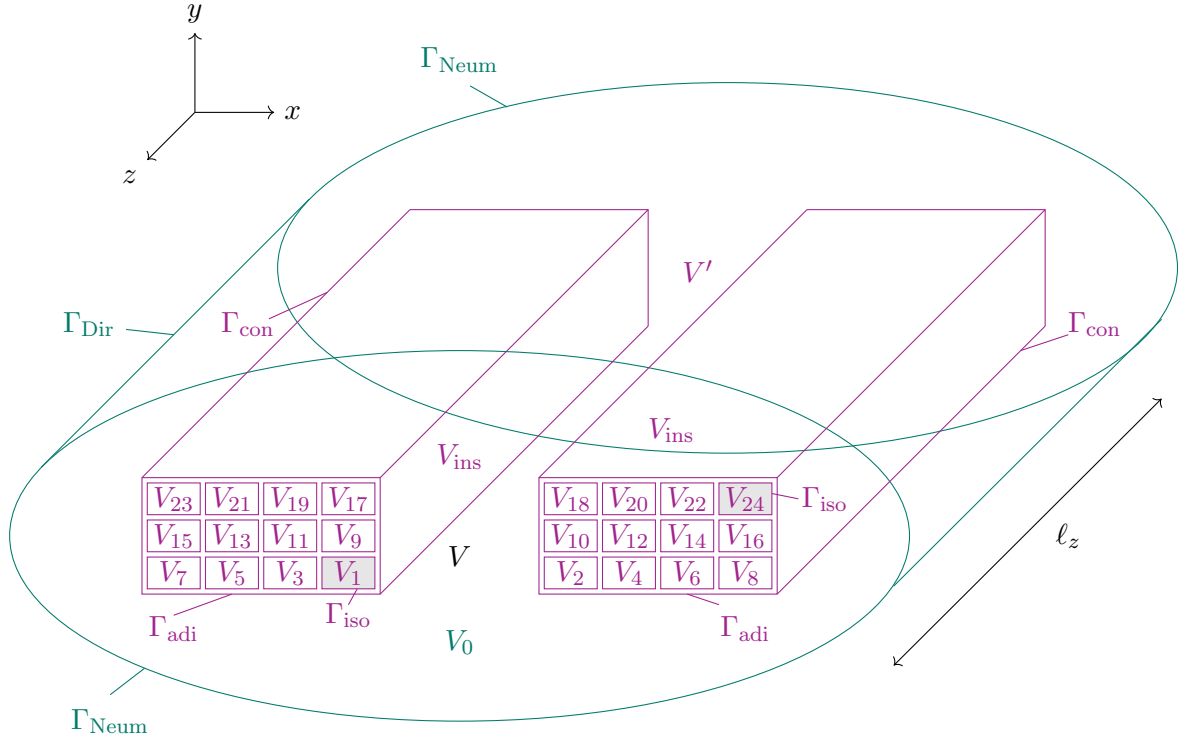


Figure 3.2.: Sketch of the lead example, i.e. a superconducting coil with $\mathcal{W} = 24$ half-turns in an elliptic vacuum domain. The total domain is denoted with V and includes both green and purple parts. The sub-domain $V' \subset V$ is represented only by the purple entities.

denote the proportions of copper and superconducting material in a half-turn, respectively.

3.2. Magnetic Model

Maxwell's Theory

For the quench simulation of superconducting coils, the electromagnetic phenomena are modeled by two of Maxwell's equations [Jac98],

$$\nabla \times \vec{E}(\vec{r}, t) = -\partial_t \vec{B}(\vec{r}, t) \quad \text{Faraday's law,} \quad (3.4)$$

$$\nabla \times \vec{H}(\vec{r}, t) = \vec{J}(\vec{r}, t) + \partial_t \vec{D}(\vec{r}, t) \quad \text{Ampère's law.} \quad (3.5)$$

Herein, $\vec{E} : \mathbb{R}^3 \times \mathbb{R} \mapsto \mathbb{R}^3$ is the electric field strength in V/m, $\vec{B} : \mathbb{R}^3 \times \mathbb{R} \mapsto \mathbb{R}^3$ is the magnetic flux density in T, \vec{H} is the magnetic field strength in A/m, $\vec{J} : \mathbb{R}^3 \times \mathbb{R} \mapsto \mathbb{R}^3$ is the electric current density in A/m², and $\vec{D} : \mathbb{R}^3 \times \mathbb{R} \mapsto \mathbb{R}^3$ is the electric flux density in As/m². All quantities depend on the spatial coordinate \vec{r} in m and the time t in s. The macroscopic fields \vec{H} and \vec{B} are connected through the magnetic permeability μ in H/m by [Jac98]

$$\vec{B}(\vec{r}, t) = \mu(\vec{r}, \vec{H}) \vec{H}(\vec{r}, t). \quad (3.6)$$

This quantity can be decomposed into

$$\mu(\vec{r}, t) = \mu_0 \mu_r(\vec{r}, \vec{H}) \quad (3.7)$$

with the vacuum permeability $\mu_0 = 4\pi \cdot 10^{-7}$ H/m and the unitless relative permeability μ_r . Alternatively, the relation (3.6) is often expressed via the magnetic reluctivity $\nu = \mu^{-1}$ in m/H as

$$\vec{H}(\vec{r}, t) = \nu(\vec{r}, \vec{H}) \vec{B}(\vec{r}, t). \quad (3.8)$$

In addition, \vec{J} is connected to \vec{E} via Ohm's law [Jac98]

$$\vec{J}(\vec{r}, t) = \sigma(\vec{r}, \vartheta) \vec{E}(\vec{r}, t), \quad (3.9)$$

where σ is the electric conductivity in S/m depending on the temperature ϑ in K [Rus10].

Using the lemmata of Poincaré [Rus10], it is possible to express \vec{E} and \vec{B} in terms of the electric scalar potential ϕ in V and the magnetic vector potential (MVP) \vec{A} in Vs/m as

$$\vec{E}(\vec{r}, t) = -\nabla\phi(\vec{r}, t) - \partial_t\vec{A}(\vec{r}, t), \quad (3.10)$$

$$\vec{B}(\vec{r}, t) = \nabla \times \vec{A}(\vec{r}, t). \quad (3.11)$$

Maxwell's equations (3.4)–(3.5) are invariant under the gauge transformations

$$\phi^*(\vec{r}, t) = \phi(\vec{r}, t) - \partial_t\Lambda(\vec{r}, t), \quad (3.12)$$

$$\vec{A}^*(\vec{r}, t) = \vec{A}(\vec{r}, t) + \nabla\Lambda(\vec{r}, t), \quad (3.13)$$

where Λ is an arbitrary scalar field, meaning that the observable physical fields \vec{E} and \vec{B} are not influenced by the choice of Λ . Because of the arbitrariness of Λ , the electric scalar potential ϕ is only unique up to a constant and the magnetic vector potential \vec{A} is only unique up to a gradient field [Ham99]. While the definition of a ground potential already resolves this issue for ϕ , a gauge condition is necessary for \vec{A} . In this work, the Coulomb gauge

$$\nabla \cdot \vec{A}(\vec{r}, t) = 0 \quad (3.14)$$

is utilized, which is motivated from Helmholtz' theorem stating that a vector field is uniquely determined by its sources and curls [Rus10].

Magnetoquasistatic Formulation

Due to $\partial_t\vec{D} \ll \vec{J}$ in superconducting coils, Ampère's law (3.5) is reduced to

$$\nabla \times \vec{H}(\vec{r}, t) = \vec{J}(\vec{r}, t). \quad (3.15)$$

Using (3.8) and (3.11), one obtains the MQS formulation in terms of the MVP \vec{A} in a 3D domain $V \subset \mathbb{R}^3$, reading

$$\nabla \times \left(\nu(\vec{r}, \vec{H}) \nabla \times \vec{A}(\vec{r}, t) \right) = \vec{J}(\vec{r}, t) \quad \text{in } V. \quad (3.16)$$

The current density on the right-hand side is composed of two parts,

$$\vec{J}(\vec{r}, t) = \vec{J}_m(\vec{r}, t) + \vec{J}_e(\vec{r}, t). \quad (3.17)$$

The magnetization current density

$$\vec{J}_m(\vec{r}, t) = \nabla \times \vec{M}_{\text{IFCC}}(\vec{r}, t) \quad (3.18)$$

models the IFCC phenomenon that generates a magnetization

$$\vec{M}_{\text{IFCC}}(\vec{r}, t) = -\nu(\vec{r}, \vec{H})\tau(\vec{r}, \vartheta) \partial_t \vec{B}(\vec{r}, t). \quad (3.19)$$

Here, τ is a given characteristic IFCC time constant in s [Ver95], which depends on the temperature ϑ in K, since the IFCC effect does not occur in normalconducting regions ($\vartheta > \vartheta_{\text{crit}}$). With (3.11), the IFCC magnetization current density (3.18) is expressed in terms of the MVP as

$$\vec{J}_m(\vec{r}, t) = -\nabla \times \left(\nu(\vec{r}, \vec{H})\tau(\vec{r}, \vartheta) \nabla \times \partial_t \vec{A}(\vec{r}, t) \right). \quad (3.20)$$

The current density component \vec{J}_e follows Ohm's law (3.9). With (3.10), it is expressed in terms of the MVP and the electric scalar potential as

$$\vec{J}_e(\vec{r}, t) = -\sigma(\vec{r}, \vartheta) \partial_t \vec{A}(\vec{r}, t) - \sigma(\vec{r}, \vartheta) \nabla \phi(\vec{r}, t). \quad (3.21)$$

The first term describes eddy currents as a consequence of time-varying magnetic fields, while the second term models impressed currents. The negative gradient of the electric potential is rewritten as

$$-\nabla \phi(\vec{r}, t) = \sum_{w=1}^{\mathcal{W}} u_w(t) \vec{\xi}_w(\vec{r}), \quad w = 1, \dots, \mathcal{W} \quad (3.22)$$

in terms of a voltage drop u_w in V along the w -th half-turn of the coil [SDW13]. Herein,

$$\vec{\xi}_w(\vec{r}) = \frac{T_w(\vec{r})}{\ell_w} \vec{e}_z, \quad w = 1, \dots, \mathcal{W} \quad (3.23)$$

is the voltage distribution function in m^{-1} , where ℓ_w denotes the half-turn's length in m and

$$T_w(\vec{r}) = \begin{cases} 1 & \text{if } \vec{r} \in V_w, \\ 0 & \text{if } \vec{r} \notin V_w, \end{cases} \quad w = 1, \dots, \mathcal{W} \quad (3.24)$$

is the characteristic function for V_w , the volume of the w -th half-turn [SDW13]. For non-overlapping domains V_w , it holds $\vec{\xi}_w \cdot \vec{\xi}_v = 0$ for $v \neq w$. The current flowing through the v -th half-turn is linked to the MVP and the voltage drop by [SDW13]

$$i_v(t) = \int_V \vec{J}_e(\vec{r}, t) \cdot \vec{\xi}_v(\vec{r}) dV. \quad (3.25)$$

Due to the serial connection of the coil windings and the alternating winding direction of the half-turns, it holds

$$i_v(t) = (-1)^v i_{\text{src}}(t), \quad v = 1, \dots, \mathcal{W}, \quad (3.26)$$

where i_{src} is the source current in A. Additionally, boundary conditions (BCs) apply on the domain's boundary $\partial V = \Gamma_{\text{Dir}} \cup \Gamma_{\text{Neum}}$,

$$\vec{B}(\vec{r}, t) = \vec{B}_{\text{ext}}(\vec{r}, t) \quad \text{on } \Gamma_{\text{ext}} \quad (3.27a)$$

$$\vec{n} \times \vec{A}(\vec{r}, t) = 0 \quad \text{on } \Gamma_{\text{Dir}}, \quad (3.27b)$$

$$\vec{n} \times \vec{H}(\vec{r}, t) = 0 \quad \text{on } \Gamma_{\text{Neum}}, \quad (3.27c)$$

where \vec{n} is the outward-pointing normal vector with respect to the boundary, and \vec{B}_{ext} represents an external magnetic field. Mathematically, (3.27a) is an inhomogeneous Dirichlet BC, while (3.27b) is a homogeneous Dirichlet BC, which forces the normal component of the magnetic field to vanish at the boundary Γ_{Dir} . Furthermore, an initial condition

$$\vec{A}(\vec{r}, t = 0) = \vec{A}_0(\vec{r}) \quad \text{in } V \quad (3.28)$$

with the initial MVP \vec{A}_0 holds. Despite of defining BCs, the MVP is not unique, as already discussed. To resolve this issue, the Coulomb gauge condition (3.14) is utilized. In the end, the nonlinear magnetic boundary value problem (BVP) of the quench model is obtained:

MAGNETIC MODEL:

$$\nabla \times \left(\nu(\vec{r}, \vec{H}) \nabla \times \vec{A}(\vec{r}, t) \right) = \vec{J}_{\text{m}}(\vec{r}, t) + \vec{J}_{\text{e}}(\vec{r}, t) \quad \text{in } V, \quad (3.29a)$$

$$\vec{J}_{\text{m}}(\vec{r}, t) = -\nabla \times \left(\nu(\vec{r}, \vec{H}) \tau(\vartheta) \nabla \times \partial_t \vec{A}(\vec{r}, t) \right), \quad (3.29b)$$

$$\vec{J}_{\text{e}}(\vec{r}, t) = -\sigma(\vec{r}, \vartheta) \partial_t \vec{A}(\vec{r}, t) + \sigma(\vec{r}, \vartheta) u_w(t) \vec{\xi}_w(\vec{r}, t), \quad (3.29c)$$

$$i_{\text{src}}(t) = (-1)^v \int_V \vec{J}_{\text{e}}(\vec{r}, t) \cdot \vec{\xi}_v(\vec{r}) dV, \quad (3.29d)$$

$$\nabla \cdot \vec{A}(\vec{r}, t) = 0 \quad \text{in } V, \quad (3.29e)$$

$$\vec{B}(\vec{r}, t) = \vec{B}_{\text{ext}}(\vec{r}, t) \quad \text{on } \Gamma_{\text{ext}}, \quad (3.29f)$$

$$\vec{n} \times \vec{A}(\vec{r}, t) = 0 \quad \text{on } \Gamma_{\text{Dir}}, \quad (3.29g)$$

$$\vec{n} \times \vec{H}(\vec{r}, t) = 0 \quad \text{on } \Gamma_{\text{Neum}}, \quad (3.29h)$$

$$\vec{A}(\vec{r}, t = 0) = \vec{A}_0(\vec{r}) \quad \text{in } V, \quad (3.29i)$$

for $v, w = 1, \dots, W$ and a given source current i_{src} .

3.3. Thermal Model

Heat is transferred either by conduction, convection or thermal radiation [VDI10]. For the quench problem, heat conduction within the cables and convective heat transfer within the cooling medium play the main role for the temperature dynamics. The heat transfer is described by the transient

heat conduction equation

$$-\nabla \cdot (\lambda(\vartheta) \nabla \vartheta(\vec{r}, t)) + C_V(\vartheta) \partial_t \vartheta(\vec{r}, t) = q_V(\vec{r}, t) \quad \text{in } V' \quad (3.30)$$

with $\vartheta : \mathbb{R}^3 \times \mathbb{R} \rightarrow \mathbb{R}$ as the scalar temperature field in K, λ as thermal conductivity in W/(mK), $C_V = \rho_d c_p$ as the volumetric heat capacity in J/(m³ K), which is composed of the density ρ_d in kg/m⁻³ and the specific heat capacity c_p in J/(kg K), and q_V as volumetric heat flux density in W/m³, representing a heat excitation density in the domain [VDI10]. Note that the material properties depend on the temperature, which makes the problem nonlinear.

In addition to the PDE (3.30), BCs apply on the domain's boundary $\partial V = \Gamma_{\text{iso}} \cup \Gamma_{\text{adi}} \cup \Gamma_{\text{con}}$,

$$\vartheta(\vec{r}, t) = \vartheta_{\text{iso}}(\vec{r}, t) \quad \text{on } \Gamma_{\text{iso}}, \quad (3.31a)$$

$$-\lambda(\vec{r}, t) \partial_n \vartheta(\vec{r}, t) = 0 \quad \text{on } \Gamma_{\text{adi}}, \quad (3.31b)$$

$$-\lambda(\vec{r}, t) \partial_n \vartheta(\vec{r}, t) = \alpha(\vec{r}, \vartheta) (\vartheta(\vec{r}, t) - \vartheta_{\text{fluid}}) \quad \text{on } \Gamma_{\text{con}}. \quad (3.31c)$$

Herein, $\partial_n = \vec{n} \cdot \nabla$ is the partial derivative in normal direction, (3.31a) describes an isothermal BC, i.e. a fixed temperature ϑ_{iso} on the boundary Γ_{iso} ; (3.31b) represents an adiabatic BC, meaning that the heat flux vanishes on the boundary Γ_{adi} ; and (3.31c) takes the convective heat transfer through the ambient boundary Γ_{con} into account, where α is the heat transfer coefficient in W/(m²K) and ϑ_{fluid} is the temperature of the ambient fluid in K. Furthermore, an initial condition with the initial temperature distribution ϑ_0 holds,

$$\vartheta(\vec{r}, t = 0) = \vartheta_0(\vec{r}) \quad \text{in } V. \quad (3.32)$$

Together, (3.30), (3.31) and (3.32) form the thermal BVP:

THERMAL MODEL:

$$-\nabla \cdot (\lambda(\vec{r}, \vartheta) \nabla \vartheta(\vec{r}, t)) + C_V(\vec{r}, \vartheta) \partial_t \vartheta(\vec{r}, t) = q_V(\vec{r}, t) \quad \text{in } V', \quad (3.33a)$$

$$\vartheta(\vec{r}, t) = \vartheta_{\text{iso}}(\vec{r}, t) \quad \text{on } \Gamma_{\text{iso}}, \quad (3.33b)$$

$$-\lambda(\vec{r}, \vartheta) \partial_n \vartheta(\vec{r}, t) = 0 \quad \text{on } \Gamma_{\text{adi}}, \quad (3.33c)$$

$$-\lambda(\vec{r}, \vartheta) \partial_n \vartheta(\vec{r}, t) = \alpha(\vec{r}, \vartheta) (\vartheta(\vec{r}, t) - \vartheta_{\text{fluid}}) \quad \text{on } \Gamma_{\text{con}}, \quad (3.33d)$$

$$\vartheta(\vec{r}, t = 0) = \vartheta_0(\vec{r}) \quad \text{in } V'. \quad (3.33e)$$

The thermal model (3.33) is coupled to the magnetic model (3.29) through the heat losses generated by the different current components in (3.17),

$$q_V(\vec{r}, t) = q_m(\vec{r}, t) + q_e(\vec{r}, t) \quad (3.34)$$

with the IFCL density arising through the IFCC magnetization currents,

$$q_m(\vec{r}, t) = \nu(\vec{r}, \vec{H}) \tau(\vec{r}, \vartheta) \left\| \nabla \times \partial_t \vec{A}(\vec{r}, t) \right\|^2, \quad (3.35)$$

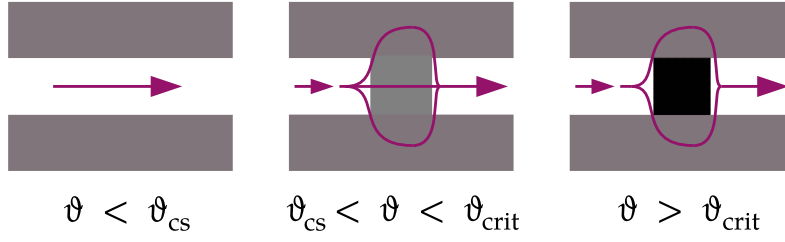


Figure 3.3.: Current sharing phenomenon in a multi-filamentary superconducting cable. Superconducting regions are depicted in white, normalconducting regions in shades of gray indicating their electrical conductivity. Arrows visualize the source current flow.

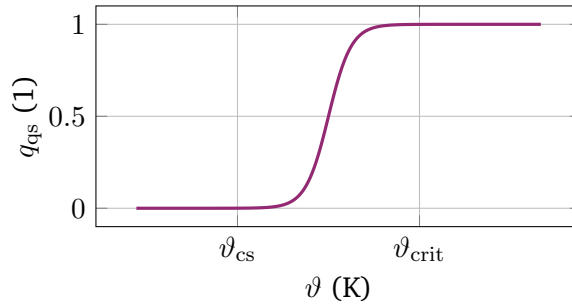


Figure 3.4.: Smooth quench state model based on the current sharing and critical temperature of the superconductor [DSD22].

and the Ohmic loss density due to the eddy currents and the voltage drop along the w -th half-turn,

$$q_e(\vec{r}, t) = \sigma(\vec{r}, \vartheta) \left\| \partial_t \vec{A}(\vec{r}, t) \right\|^2 + \sigma(\vec{r}, \vartheta) \left\| u_w(t) \vec{\xi}_w(\vec{r}) \right\|^2. \quad (3.36)$$

3.4. Quench State Model

Depending on whether a specific region in the model is currently superconducting or normalconducting, different effects and material characteristics apply. In superconducting regions, the IFCCs (3.20), and thus IFCLs (3.35), have to be taken into account, which are characterized by the IFCC time constant τ . In normalconducting regions, Ohmic currents (3.21) and Ohmic heat losses (3.36) arise, which are characterized by the electric conductivity σ . Upon quenching, the governing effects and material characteristics change.

To model this transition of physical phenomena, a temperature-dependent quench state function $q_{qs}(\vartheta) : \mathbb{R} \mapsto [0, 1]$ is defined [DSD22]. This function takes the current sharing phenomenon [Sha15] into account which occurs in superconducting multi-filamentary wires, as shown in Fig. 3.3. If the temperature in a superconducting filament rises above a current sharing temperature ϑ_{cs} , the filament starts to quench, i.e. its resistivity rises. The source current in this filament begins to favor paths in the surrounding copper matrix, although a part of the current still flows through the partly quenched filament segment. However, when the temperature surpasses the critical temperature ϑ_{crit} , the filament segment is shifted completely to normalconducting state. As the electrical conductivity of NbTi and Nb₃Sn is lower than of copper, the source current will mainly flow around the quenched spot via the copper matrix.

Thus, for $\vartheta \leq \vartheta_{cs}$, no Joule losses arise, while for $\vartheta \geq \vartheta_{crit}$, the maximum Joule losses are generated. For $\vartheta_{cs} < \vartheta < \vartheta_{crit}$, the Joule losses increase linearly [Bot14]. Based on these observations, the quench state function is constructed as a sigmoidal function,

$$q_{qs}(\vartheta) = \left(1 + \exp \left(-16 \frac{\vartheta - \vartheta_{crit}}{\vartheta_{crit} - \vartheta_{cs}} + 8 \right) \right)^{-1}, \quad (3.37)$$

which is shown in Fig. 3.4. This smooth function is preferred over a simpler linear ramp function to avoid discontinuities which could disturb the convergence of the nonlinear iteration procedure. With this, τ and σ can be modeled as quench-state-dependent materials by

$$\tau(\vec{r}, \vartheta) = (1 - q_{qs}(\vartheta)) \kappa_{SC} \tau_{SC}, \quad (3.38)$$

$$\sigma(\vec{r}, \vartheta) = q_{qs}(\vartheta) \kappa_{Cu} \sigma_{NC}(\vec{r}, \vartheta) \quad (3.39)$$

with τ_{SC} as IFCC time constant of the superconductor, and σ_{NC} as the effective electrical conductivity of the material in normalconducting state. In this way, the IFCC effects are dominant in superconducting regions (through τ), while the Ohmic effects dominate in the normalconducting and quenched regions (through σ). Regions with $\vartheta_{cs} < \vartheta < \vartheta_{crit}$ are in the intermediate current sharing state, where both effects take part.

3.5. End Winding Models

The half-turns in the coil model are numbered from $w = 1, \dots, \mathcal{W}$ such that the first half-turn ($w = 1$) is the outermost half-turn, followed by the half-turn on the other side of the coil package ($w = 2$) which is directly connected to that first half-turn, followed by the next half-turn ($w = 3$) connected to the second one, and so on, until the last half-turn ($w = \mathcal{W}$) is reached. Figure 3.5 shows this winding scheme for an exemplary coil with $\mathcal{W} = 4$ half-turns. The respective domains are analogously enumerated and denoted as V_w , while the back surfaces ($\vec{n} = -\vec{e}_z$) and front surfaces ($\vec{n} = +\vec{e}_z$) are called Γ_w^- and Γ_w^+ , respectively, where \vec{n} is the outward-pointing normal vector with respect to the volume V_w . In a multi-layered coil as in the lead example shown in Fig. 3.2, the numbering scheme starts at the inner- and undermost half-turn on the left coil package side. When a layer is numbered through, the lastly numbered half-turn of this layer connects to the innermost half-turn of the layer on top of that in the other coil package side, see also Fig. 3.2.

The half-turns are electrically isolated from each other in transversal direction, i.e. there is no transversal current flow. Thermally, they are separated by a thin glass fibre insulation layer with a very low thermal conductivity. This results into a very low transversal heat flux and, thus, a steep temperature drop across the insulation layers [SWS22].

Connecting Half-Turns by Circuit Links

For the magnetic model, the respective half-turns are connected to each other by establishing circuit links between them. In this context, each half-turn domain V_w is treated as a solid conductor [SDW13] with a voltage drop u_w from Γ_w^+ to Γ_w^- for odd w and Γ_w^- to Γ_w^+ for even w , respectively. Following the winding scheme mentioned before, a serial connection of solid conductors from $w = 1$ to $w = \mathcal{W}$ is obtained. At Γ_1^+ and $\Gamma_{\mathcal{W}}^+$, the model is connected to an external circuit which can consist of arbitrary lumped elements [SDW13]. In the simplest case,

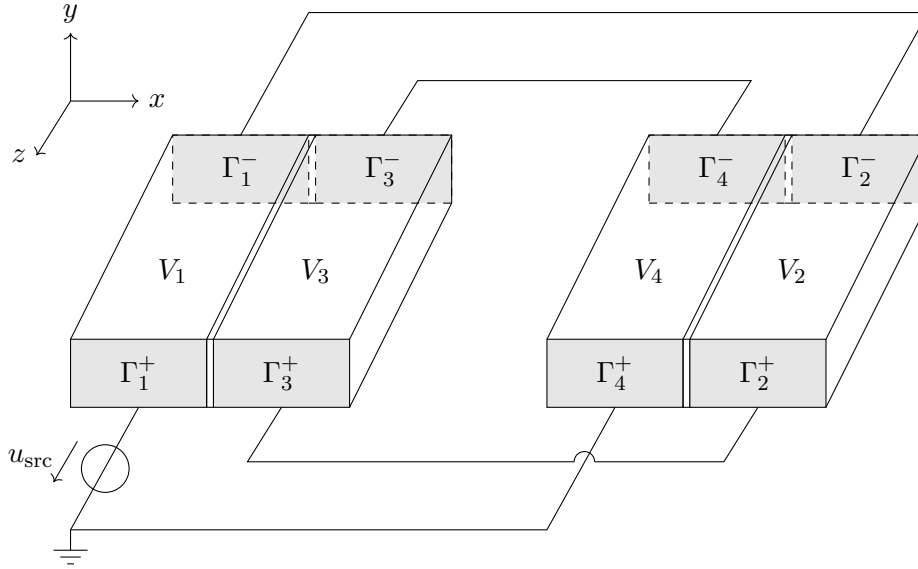


Figure 3.5.: A sketch showing the coil winding connections and numbering scheme for an exemplary coil with $\mathcal{W} = 4$ half-turns.

Γ_1^+ is connected to a voltage source u_{src} while $\Gamma_{\mathcal{W}}^+$ is grounded as shown in Fig. 3.5.

Connecting Half-Turns by Floating Boundaries

For the thermal model, the temperature distribution across the half-turn cross-sections can be assumed as constant due to the high thermal conductivity of copper and NbTi or Nb₃Sn as metallic materials and the small cross-section area of a half-turn. Therefore, BCs of the form

$$\vartheta|_{\Gamma_w^-} = \vartheta|_{\Gamma_{w+1}^-}, \quad w = 2n + 1, \quad n = 0, \dots, \frac{\mathcal{W}}{2} - 1, \quad (3.40a)$$

$$\vartheta|_{\Gamma_w^+} = \vartheta|_{\Gamma_{w+1}^+}, \quad w = 2n, \quad n = 1, \dots, \frac{\mathcal{W}}{2} - 1 \quad (3.40b)$$

can be applied for the temperatures on the half-turn end surfaces. These conditions are floating BCs [DBH03]: The temperature values on these surfaces are constant but not known beforehand. They are only determined by solving the BVP. In this way, the connected half-turns share the same temperature at their respective end surfaces. Note that Γ_1^+ and $\Gamma_{\mathcal{W}}^+$ are not included in (3.40), as these are the half-turn surfaces connected to the external circuit. On these boundaries, isothermal BCs (3.33b) are assumed.

4. Numerical Ingredients for the Q3D Method

"Double, double, toil and trouble;
Fire burn and cauldron bubble!"

William Shakespeare, *Macbeth*

The Q3D method is a hybrid numerical approach, which combines a 2D FEM in the xy -plane and a 1D SEM in the z -direction to achieve an efficient numerical technique for the quench simulation of long superconducting coils. In order to build and apply this method, this chapter collects and presents all ingredients needed to boil down the Q3D method in the subsequent Chapter 5.

4.1. Weak Formulation of the Magneto-Thermal Model

The thermal and magnetic models are transferred into their weak forms. In a next step, the discrete forms are obtained, see Sec. 4.2. In the following, the dependence on the spatial and temporal coordinates \vec{r} and t will be left out for the sake of readability.

Weak Formulation of the Thermal Model

The heat conduction equation (3.33a) is multiplied with a test function $\vartheta' \in \mathcal{U}'$ of a not yet specified function space \mathcal{U}' , and the PDE is integrated over the domain V , yielding

$$-\int_V \nabla \cdot (\lambda \nabla \vartheta) \vartheta' dV + \int_V C_V \partial_t \vartheta \vartheta' dV = \int_V q_V \vartheta' dV \quad \forall \vartheta' \in \mathcal{U}'. \quad (4.1)$$

Using integration by parts and Gauss' theorem [Bos98], (4.1) becomes

$$\int_V \lambda \nabla \vartheta \cdot \nabla \vartheta' dV - \int_{\partial V} \lambda \partial_n \vartheta \vartheta' dS + \int_V C_V \partial_t \vartheta \vartheta' dV = \int_V q_V \vartheta' dV \quad \forall \vartheta' \in \mathcal{U}'. \quad (4.2)$$

To finally obtain the weak formulation, one needs to specify the function space \mathcal{U} , in which the solution ϑ is searched, as well as the function space \mathcal{U}' of the test functions ϑ' . The function spaces \mathcal{U} and \mathcal{U}' should be chosen in a way such that the integrals in (4.2) are well-defined and that the boundary integral term vanishes [BS08]. To this end, they are chosen as

$$\mathcal{U} = \mathcal{U}' = H_0^1(V) = \{u \in H^1(V) : u = 0 \text{ on } \Gamma_{\text{iso}}\} \quad (4.3)$$

with the Hilbert space

$$H^1(V) = \{u : \nabla u \in L_2(V)\} \quad (4.4)$$

and the function space of square-integrable functions,

$$L_2(V) = \left\{ u : \int_V |u|^2 dV < \infty \right\}. \quad (4.5)$$

In the end, the weak formulation for the thermal model reads:

$$\left\{ \begin{array}{l} \text{Find } \vartheta \in H_0^1(V) \text{ s.t.} \\ \int_V \lambda \nabla \vartheta \cdot \nabla \vartheta' dV + \int_V C_V \partial_t \vartheta \vartheta' dV = \int_V q_V \vartheta' dV \quad \forall \vartheta' \in H_0^1(V). \end{array} \right. \quad (4.6)$$

Note that this weak formulation is only valid for homogeneous Dirichlet BCs due to $\vartheta \in H_0^1(V)$. Section 5.3 will show how to consider a scenario with inhomogeneous Dirichlet boundaries in the Q3D setting.

Weak Formulation for the Magnetic Model

The MQS potential formulation (3.29a) is multiplied with a vectorial test function $\vec{A}' \in \mathcal{V}$ and the PDE is integrated over the domain V . Integration by parts, vector-algebraic manipulation and applying Stokes' theorem [Bos98] lead to

$$\int_V \nu \nabla \times \vec{A} \cdot \nabla \times \vec{A}' dV + \int_{\partial V} (\nu \nabla \times \vec{A}) \times \vec{A}' \cdot d\vec{S} = \int_V \vec{J} \cdot \vec{A}' dV \quad \forall \vec{A}' \in \mathcal{V}. \quad (4.7)$$

Due to the De Rham sequence [Rus10], one chooses

$$\mathcal{V} = \mathcal{V}' = H_0(\text{curl}; V) = \{ \vec{v} \in H(\text{curl}; V) : \vec{v} \times \vec{n} = 0 \text{ on } \Gamma_{\text{Dir}} \} \quad (4.8)$$

with

$$H(\text{curl}; V) = \{ \vec{v} : \nabla \times \vec{v} \in L_2(V) \} \quad (4.9)$$

as the function space of curl-conforming functions in order to ensure that the integrals in (4.7) are well-defined. Considering (3.17), the current density in the right-hand side of (4.7) consists of two parts, $\vec{J} = \vec{J}_e + \vec{J}_m$. Thus, the right-hand side of (4.7) is decomposed into two parts reading

$$\int_V \vec{J}_m \cdot \vec{A}' dV = \int_V \nu \tau \nabla \times \partial_t \vec{A} \cdot \nabla \times \vec{A}' dV, \quad (4.10)$$

$$\int_V \vec{J}_e \cdot \vec{A}' dV = - \int_V \sigma \partial_t \vec{A} \cdot \vec{A}' dV + u_w \int_V \sigma \vec{\xi}_w \cdot \vec{A}' dV \quad (4.11)$$

using (3.20), (3.21) and (3.22).

The gauge condition (3.29e) is taken into account by introducing Lagrange multipliers $\zeta \in H_0^1(V)$ and adding the negative gradient $-\nabla \zeta$ as additional term to (4.7)[CDN18]. By gathering all equations, one finally obtains the weak formulation for the magnetic problem:

$$\left\{ \begin{array}{l}
\text{Find } \vec{A} \in H_0(\text{curl}; V), \zeta \in H_0^1(V), u_w \in \mathbb{R}, \text{ with } w = 1, \dots, \mathcal{W} \text{ s.t.} \\
\text{(I): } \int_V \nu \nabla \times \vec{A} \cdot \nabla \times \vec{A}' \, dV + \int_V \nu \tau \nabla \times \partial_t \vec{A} \cdot \nabla \times \vec{A}' \, dV + \int_V \sigma \partial_t \vec{A} \cdot \vec{A}' \, dV \\
\quad - \int_V \nabla \zeta \cdot \vec{A}' \, dV - \sum_{w=1}^{\mathcal{W}} u_w \int_V \sigma \vec{\xi}_w \cdot \vec{A}' \, dV = 0 \quad \forall \vec{A}' \in H_0(\text{curl}; V), \\
\text{(II): } - \int_V \vec{A} \cdot \nabla \zeta' \, dV = 0 \quad \forall \zeta' \in H_0^1(V), \\
\text{(III): } - \int_V \sigma \partial_t \vec{A} \cdot \vec{\xi}_v \, dV + u_w \int_V \sigma \vec{\xi}_w \cdot \vec{\xi}_v \, dV = i_v, \quad v = 1, \dots, \mathcal{W}.
\end{array} \right. \quad (4.12)$$

As in the case of the thermal problem, this weak formulation is only valid for problems with homogeneous Dirichlet BCs due to the choice of $\vec{A} \in H_0(\text{curl}; V)$. Inhomogeneous Dirichlet boundaries are covered in Sec. 5.3 for the Q3D setting.

4.2. Discretization of the Magneto-Thermal Model

Discretization of the Domain

The domain V is discretized into a computational domain V_h , and the continuous weak formulation is translated into a discrete weak formulation. Herein, the subscript h denotes a method-dependent discretization parameter. With $h \rightarrow 0$, the solution of the discrete problem should converge against the solution of the continuous problem [Bra12]. The nature of this spatial discretization and, thus, of the resulting mesh depends on the employed numerical method and the dimensionality of the considered domain:

- In the 2D FEM, a triangulation of the 2D cross-section $\Omega \subset V$ leads to triangles T and the 2D Cartesian computational domain Ω_h , see Sec. 4.3. For first-order FEM, the discretization parameter h relates to the mesh length, meaning that convergence is achieved by refining the triangular mesh [Bra12].
- In the 1D SEM, the interval I is subdivided into line elements I_k , see Sec. 4.4. Here, the discrete solution converges with the refinement of the mesh and also with increasing order of the employed basis functions [STW11].
- In the Q3D hybrid method, the 3D domain is discretized using prism elements P as a combination of 2D triangles T in the cross-section Ω_h and 1D lines I_k in the third dimension, see Chapter 5. Here, a convergence is achieved by either refining the FE or SE mesh, or by increasing the order of the basis functions.

Discretization of Function Spaces

The discrete weak formulation is obtained by approximating the original function space \mathcal{U} by finite-dimensional closed function subspace $\mathcal{U}_h \subset \mathcal{U}$. The concrete definition of \mathcal{U}_h depends on the choice of the numerical method:

- In the first-order FEM with nodal shape functions, $\mathcal{U}_h = \mathcal{S}_0^1(\Omega_h) \cap H_0^1(\Omega_h)$ with $\mathcal{S}_0^1(\Omega_h)$ being the function space of continuous splines of first order (hat functions) with compact support on the domain Ω_h , see Sec. 4.3.
- In the FEM with first-order edge shape functions, $\mathcal{U}_h = \mathcal{S}_0^1(\Omega_h) \cap H_0(\text{curl}; \Omega_h)$, see Sec. 4.3.
- In the SEM, $\mathcal{U}_h = \mathcal{P}_0^N(I) \cap H_0^1(I)$ with $\mathcal{P}_0^N(I)$ being the function space of continuous orthogonal polynomials with a maximal order of N with compact support on the interval I , see Sec. 4.4.
- In the Q3D hybrid method, $\mathcal{U}_h = \mathcal{U}_h^{2\text{DFE}}(\Omega_h) \times \mathcal{U}_h^{1\text{DSE}}(I)$, i.e. a tensorial product of the 2D FE and 1D SE function spaces is used, see Chapter 5.

Discretization of the Solution

The temperature and MVP are approximated as

$$\vartheta(\vec{r}, t) \approx \sum_{j=1}^{\mathcal{J}} \vartheta_j(t) v_j(\vec{r}), \quad (4.13)$$

$$\vec{A}(\vec{r}, t) \approx \sum_{e=1}^{\mathcal{E}} \hat{a}_e(t) \vec{v}_e(\vec{r}) \quad (4.14)$$

with \mathcal{J} scalar shape functions $v_j(\vec{r}) \in \mathcal{U}_h(V_h)$ and \mathcal{E} vectorial shape functions $\vec{v}_e(\vec{r}) \in \mathcal{U}_h(\text{curl}; V)$, where \mathcal{J} and \mathcal{E} are the numbers of degrees of freedom (DoF) for the temperature and the MVP, respectively. Here, ϑ_j are the temperature coefficients, and \hat{a}_e are the MVP coefficients. The bow indicates that \hat{a}_e represent the line-integrated MVP¹ in Vs as opposed to the MVP, which is in Vs/m.

Following the Ritz-Galerkin approach, the same test functions $v_i(\vec{r}), i = 1, \dots, \mathcal{J}$ and $\vec{v}_e(\vec{r}), e = 1, \dots, \mathcal{E}$ are used. Eventually, one obtains for the thermal problem (4.6) the spatially discretized formulation

$$\left\{ \begin{array}{l} \text{Find } u_j, j = 1, \dots, \mathcal{J} \text{ s.t.} \\ \sum_{j=1}^{\mathcal{J}} \vartheta_j \int_{V_h} \lambda \nabla v_j \cdot \nabla v_i \, dV + \sum_{j=1}^{\mathcal{J}} \partial_t \vartheta_j \int_{V_h} C_V v_j v_i \, dV = \int_{V_h} q_V v_i \, dV \quad \forall v_i \in \mathcal{U}_h. \end{array} \right. \quad (4.15)$$

¹This notation is taken from the finite integration technique [CW01].

Analogously, the magnetic problem (4.12) is translated into

$$\left\{ \begin{array}{l} \text{Find } \hat{a}_e \text{ with } e = 1, \dots, \mathcal{E}; u_w \text{ with } w = 1, \dots, \mathcal{W}; \zeta_j \text{ with } j = 1, \dots, \mathcal{J} \text{ s.t.} \\ \text{(I): } \sum_{e=1}^{\mathcal{E}} \hat{a}_e \int_{V_h} \nu \nabla \times \vec{v}_e \cdot \nabla \times \vec{v}_d \, dV + \sum_{e=1}^{\mathcal{E}} \partial_t \hat{a}_e \int_{V_h} \nu \tau \nabla \times \vec{v}_e \cdot \nabla \times \vec{v}_d \, dV \\ \quad + \sum_{e=1}^{\mathcal{E}} \partial_t \hat{a}_e \int_{V_h} \sigma \vec{v}_e \cdot \vec{v}_d \, dV - \sum_{j=1}^{\mathcal{J}} \zeta_j \int_{V_h} \nabla v_j \cdot \vec{v}_d \, dV \\ \quad - \sum_{w=1}^{\mathcal{W}} u_w \int_{V_h} \vec{\xi}_w \cdot \vec{v}_d \, dV = 0 \quad \forall \vec{v}_d \in \mathcal{V}_h, \\ \text{(II): } - \sum_{e=1}^{\mathcal{E}} \hat{a}_e \int_{V_h} \vec{v}_e \cdot \nabla v_i \, dV = 0 \quad \forall v_i \in \mathcal{U}_h, \\ \text{(III): } - \sum_{e=1}^{\mathcal{E}} \partial_t \hat{a}_e \int_{V_h} \sigma \vec{v}_e \cdot \vec{\xi}_v \, dV + \sum_{w=1}^{\mathcal{W}} u_w \int_{V_h} \sigma \vec{\xi}_w \cdot \vec{\xi}_v \, dV = i_v, \quad v = 1, \dots, \mathcal{W}. \end{array} \right. \quad (4.16)$$

Here, the Lagrange multipliers ζ are discretized with nodal shape functions $v_j(\vec{r}) \in \mathcal{U}_h(V_h)$.

Translation into a System of Equations

Next, the terms in the discrete formulations (4.15) and (4.16) are written in a system of equations, such that they can be expressed as matrices and vectors. In the following notation, the subscript of a discrete quantity indicates the material parameter for a matrix and a function for a vector, respectively. For the thermal problem (4.15), the entries of the matrices and vectors arise as

$$(\mathbf{K}_\lambda^n)_{ij} = \int_{V_h} \lambda \nabla v_j \cdot \nabla v_i \, dV \quad \text{thermal conductance matrix,} \quad (4.17)$$

$$(\mathbf{M}_{C_V}^n)_{ij} = \int_{V_h} C_V v_j v_i \, dV \quad \text{thermal capacitance matrix,} \quad (4.18)$$

$$(\mathbf{q}_V)_i = \int_{V_h} q_V v_i \, dV \quad \text{thermal load vector.} \quad (4.19)$$

The matrices (4.17) and (4.18) are also commonly referred to as stiffness matrix and mass matrix, respectively. Eventually, this leads to the thermal semi-discrete system of equations

$$\mathbf{K}_\lambda^n \boldsymbol{\vartheta} + \mathbf{M}_{C_V}^n \frac{d\boldsymbol{\vartheta}}{dt} = \mathbf{q}_V, \quad (4.20)$$

where the vector $\boldsymbol{\vartheta}$ collects the temperature coefficients ϑ_j . For the magnetic problem (4.16), the matrices read

$$(\mathbf{K}_c^e)_{de} = \int_{V_h} c \nabla \times \vec{v}_e \cdot \nabla \times \vec{v}_d dV \quad \text{magnetic reluctance matrix,} \quad (4.21)$$

$$(\mathbf{M}_\sigma^e)_{de} = \int_{V_h} \sigma \vec{v}_e \cdot \vec{v}_d dV \quad \text{electrical conductance matrix,} \quad (4.22)$$

$$(\mathbf{C}_1)_{ie} = \int_{V_h} \vec{v}_e \cdot \nabla v_i dV \quad \text{node-edge coupling matrix,} \quad (4.23)$$

$$(\mathbf{X}_\sigma)_{dw} = \int_{V_h} \sigma \vec{\xi}_w \cdot \vec{v}_d dV \quad \text{winding matrix,} \quad (4.24)$$

$$(\mathbf{G}_\sigma)_{vw} = \int_{V_h} \sigma \vec{\xi}_w \cdot \vec{\xi}_v dV \quad \text{direct current conductance matrix.} \quad (4.25)$$

with $c \in \{\nu, \nu\tau\}$. Finally, this leads to the magnetic semi-discrete system of equations

$$\begin{bmatrix} \mathbf{K}_\nu^e + \mathbf{K}_{\nu\tau}^e \frac{d}{dt} + \mathbf{M}_\sigma^e \frac{d}{dt} & -\mathbf{X}_\sigma & \mathbf{C}_1^\top \\ -\mathbf{X}_\sigma^\top \frac{d}{dt} & \mathbf{G}_\sigma & \mathbf{0} \\ \mathbf{C}_1 & \mathbf{0} & \mathbf{0} \end{bmatrix} \begin{bmatrix} \hat{\mathbf{a}} \\ \mathbf{u} \\ \boldsymbol{\zeta} \end{bmatrix} = \begin{bmatrix} \mathbf{0} \\ \mathbf{i} \\ \mathbf{0} \end{bmatrix}. \quad (4.26)$$

Here, $\hat{\mathbf{a}}$ collects the MVP coefficients \hat{a}_e , \mathbf{u} the voltage drops u_w per half-turn, $\boldsymbol{\zeta}$ the Lagrange multipliers ζ_j and \mathbf{i} the half-turn currents i_v .

Temporal Discretization

After the spatial discretization, the temporal derivative $\frac{d}{dt}$ still needs to be discretized in order to obtain fully discrete systems of equations. To this end, the continuous time range $t = [0, t_{\text{end}}]$ is discretized into time instances $t_i, i = 1, \dots, N_{\text{time}}$ and the i -th time step is defined as $\Delta t_i = t_{i+1} - t_i$. In this work, a backward implicit Euler scheme [Qua17] is applied to (4.20) and (4.26), where the solution vectors represent the solution in the next time step t_{i+1} ,

$$\boldsymbol{\vartheta}^{(i+1)} := \boldsymbol{\vartheta}(t = t_{i+1}) \quad \text{and} \quad \hat{\mathbf{a}}^{(i+1)} := \hat{\mathbf{a}}(t = t_{i+1}), \quad (4.27)$$

and the time derivative of a discrete quantity \mathbf{x} at t_{i+1} is approximated as

$$\frac{d\mathbf{x}(t_{i+1})}{dt} \approx \frac{\mathbf{x}^{(i+1)} - \mathbf{x}^{(i)}}{\Delta t_i}. \quad (4.28)$$

With this, the thermal system of equations finally reads

$$\mathbf{K}_\lambda^n(\boldsymbol{\vartheta}^{(i+1)}) \boldsymbol{\vartheta}^{(i+1)} + \frac{1}{\Delta t_i} \mathbf{M}_{C_V}^n(\boldsymbol{\vartheta}^{(i+1)}) \boldsymbol{\vartheta}^{(i+1)} = \mathbf{q}_V(\boldsymbol{\vartheta}^{(i+1)}) + \frac{1}{\Delta t_i} \mathbf{M}_{C_V}^n(\boldsymbol{\vartheta}^{(i)}) \boldsymbol{\vartheta}^{(i)}, \quad (4.29)$$

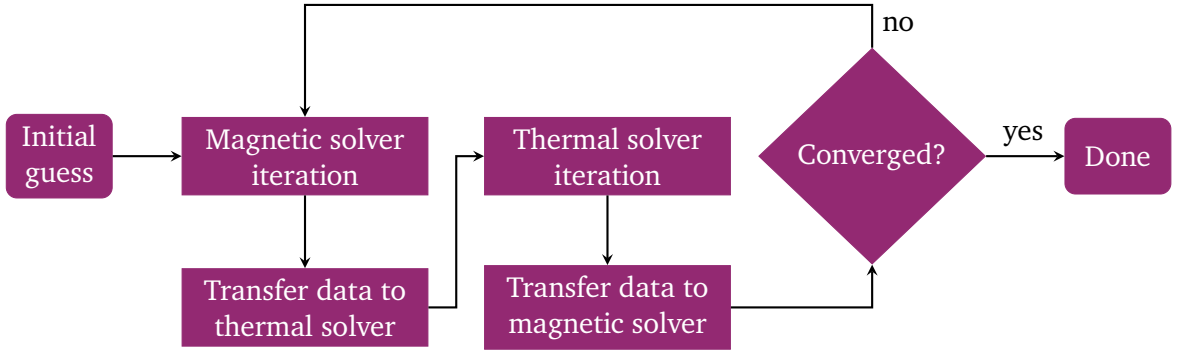


Figure 4.1.: Nonlinear iteration scheme for the magneto-thermal coupled problem utilizing the alternating nonlinear method [SJ17]. Herein, the magnetic and thermal solver are applied successively. Then, prescribed convergence criteria are checked such as (4.31) and whether a maximum iteration number has been reached.

and the magnetic system of equations reads

$$\begin{bmatrix} \mathbf{K}_\nu^e + \frac{1}{\Delta t_i} (\mathbf{K}_{\nu\tau}^e(\boldsymbol{\vartheta}^{(i+1)}) + \mathbf{M}_\sigma^e(\boldsymbol{\vartheta}^{(i+1)})) & -\mathbf{X}_\sigma(\boldsymbol{\vartheta}^{(i+1)}) & \mathbf{C}_1^T \\ -\frac{1}{\Delta t_i} \mathbf{X}_\sigma^T(\boldsymbol{\vartheta}^{(i+1)}) & \mathbf{G}_\sigma(\boldsymbol{\vartheta}^{(i+1)}) & \mathbf{0} \\ \mathbf{C}_1 & \mathbf{0} & \mathbf{0} \end{bmatrix} \begin{bmatrix} \hat{\mathbf{a}}^{(i+1)} \\ \mathbf{u}^{(i+1)} \\ \zeta^{(i+1)} \end{bmatrix} = \begin{bmatrix} \frac{1}{\Delta t_i} (\mathbf{K}_{\nu\tau}^e(\boldsymbol{\vartheta}^{(i)}) + \mathbf{M}_\sigma^e(\boldsymbol{\vartheta}^{(i)})) \hat{\mathbf{a}}^{(i)} \\ \mathbf{i} - \frac{1}{\Delta t_i} \mathbf{X}_\sigma^T(\boldsymbol{\vartheta}^{(i)}) \hat{\mathbf{a}}^{(i)} \\ \mathbf{0} \end{bmatrix}. \quad (4.30)$$

Note that there exist more sophisticated time discretization schemes, see e.g. [ND96; CWW02; Cor+17]. However, as this work emphasizes the spatial discretization of quench simulation, a more elaborated temporal discretization is not pursued.

Nonlinear Iteration Scheme

The multi-physical quench simulation requires to solve two strongly coupled nonlinear system of equations, which represent the co-simulated thermal and magnetic problems. Different approaches exist to handle such coupled nonlinear systems. Here, the alternating nonlinear method is employed, which works best for avoiding over-solving, thus increasing the overall computational efficiency [SJ17]. In this approach, the magnetic and thermal solver are solved successively in one nonlinear iteration ($k + 1$), and the residuals of both solvers are checked for the convergence criteria

$$\Delta^{(k+1)} = \frac{1}{2} \left(\frac{\|\boldsymbol{\vartheta}^{(k+1)} - \boldsymbol{\vartheta}^{(k)}\|_2}{\|\boldsymbol{\vartheta}^{(k+1)}\|_2} + \frac{\|\hat{\mathbf{a}}^{(k+1)} - \hat{\mathbf{a}}^{(k)}\|_2}{\|\hat{\mathbf{a}}^{(k+1)}\|_2} \right) < \epsilon_{\text{tol}}. \quad (4.31)$$

with a prescribed tolerance ϵ_{tol} . Here, $\Delta^{(k+1)}$ represents the averaged relative difference of the temperature and MVP solution compared to the previous iteration k . The scheme of the alternating nonlinear method is shown in Fig. 4.1.

Algorithm 1 Fixed point iteration scheme.

Require: Initial iterate $\boldsymbol{\vartheta}^{(0)}$ as solution of the previous time step, iteration counter $k = 0$, maximal iteration number k_{\max} , initial difference $\Delta^{(0)} = \infty$, convergence tolerance ϵ_{tol} .

while $(\Delta^{(k)} > \epsilon_{\text{tol}})$ and $(k \leq k_{\max})$ **do**

Assemble system matrix $\mathbf{A}(\boldsymbol{\vartheta}^{(k)})$ and right-hand side $\mathbf{b}(\boldsymbol{\vartheta}^{(0)})$.

Solve $\mathbf{A}(\boldsymbol{\vartheta}^{(k)})\boldsymbol{\vartheta}^{(k+1)} = \mathbf{b}(\boldsymbol{\vartheta}^{(0)})$ for $\boldsymbol{\vartheta}^{(k+1)}$.

Compute $\Delta^{(k+1)} = \frac{\|\boldsymbol{\vartheta}^{(k+1)} - \boldsymbol{\vartheta}^{(k)}\|_2}{\|\boldsymbol{\vartheta}^{(k+1)}\|_2}$.

Set $k \leftarrow k + 1$.

end while

As nonlinear iteration scheme, this work employs a fixed point iteration, also known as method of successive substitution [Hau09]. The idea is to linearize the nonlinear system of equations in the working point $\boldsymbol{\vartheta}^{(k)}$, and to successively solve the system in each iteration $(k + 1)$ for the working point $\boldsymbol{\vartheta}^{(k+1)}$. The scheme ends when either the solution achieves a satisfying convergence criterion or a prescribed number of maximal iterations is reached [Hau09]. Algorithm 1 shows the procedure for a general nonlinear system of equations $\mathbf{A}(\boldsymbol{\vartheta})\boldsymbol{\vartheta} = \mathbf{b}$. In the context of the alternating nonlinear method, this procedure is performed in each iteration for both the magnetic and thermal system of equations.

4.3. First Ingredient: 2D Finite Element Method

In the Q3D method, the 2D FEM is employed to discretize the transversal cross-section of the superconducting coil. To this end, the 2D xy -cross-section Ω is partitioned into a mesh

$$\mathcal{T}_h = \{T_t, t = 1, \dots, N_{\text{FE}}\} \quad (4.32)$$

consisting of a total of N_{FE} triangular non-overlapping FEs T_t , N_n non-hanging nodes, and N_e edges. This yields the computational domain [Bra12]

$$\Omega_h = \bigcup_{T \in \mathcal{T}_h} T. \quad (4.33)$$

Nodal Shape Functions

The linear 2D nodal shape function $N_j^{(T)} : \mathbb{R}^2 \mapsto [0, 1]$ for node j on the element $T \in \mathcal{T}_h$ is given as

$$N_j^{(T)}(x, y) = a_j^{(T)}x + b_j^{(T)}y + c_j^{(T)} \in H^1(\Omega_h), \quad (4.34)$$

where $a_j^{(T)}, b_j^{(T)}, c_j^{(T)} \in \mathbb{R}$ are coefficients depending on the location of the element T , such that the nodal property

$$N_j^{(T)}(\vec{r}) = \begin{cases} 1 & \text{on node } i = j, \\ 0 & \text{on node } i \neq j, \end{cases} \quad (4.35)$$

is fulfilled. From node j , $N_j^{(T)}$ linearly decays to zero on all other nodes $i \neq j$ belonging to T and is zero on all other elements $T' \neq T$ as shown by the color scheme in Fig. 4.2a. Hence, the global

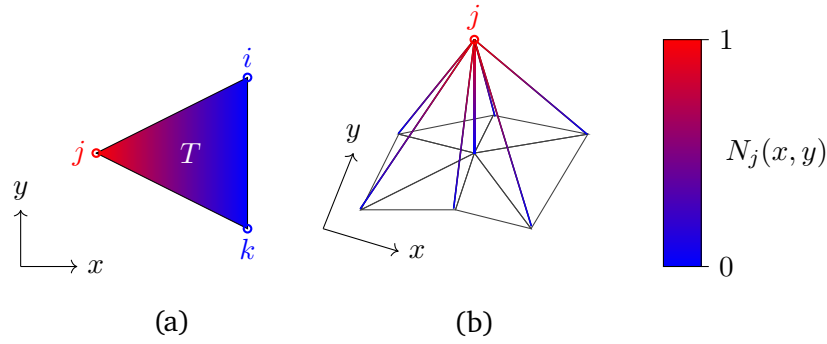


Figure 4.2.: Nodal property of linear 2D nodal shape functions: The function N_j equals one on its own node j , and linearly decays to zero for all other nodes $i \neq j$, see (a). In a 3D perspective, where the third axis represents the value of N_j , the 2D nodal shape function resembles a hat, see (b).

nodal function

$$N_j(x, y) = \sum_{T \in \mathcal{T}_h} N_j^{(T)}(x, y) \quad (4.36)$$

is a hat function with local support on all elements T featuring node j [ZTT05]. This means, that $N_j = 1$ on the node j , and that N_j decays linearly to zero to all other nodes i , which belong to elements T containing node j . In a 3D perspective, where the third dimension reflects the function's value, N_j resembles a hat as shown in Fig. 4.2b. With that properties, N_j is continuous in every spatial direction, which makes it appropriate for approximating physical fields exhibiting this type of continuity such as the temperature,

$$\vartheta(x, y; t) \approx \sum_{j=1}^J \vartheta_j(t) N_j(x, y). \quad (4.37)$$

Edge Shape Functions

For the correct representation of the MVP, edge shape functions are employed, which are $H(\text{curl})$ -conforming [Bos98] as required by the weak formulation (4.12). In general, an edge shape function is associated with an edge $e = (i, j)$ from a node i to a node j of the mesh, and is expressed in terms of the nodal shape functions as

$$\vec{w}_e(\vec{r}) = N_i(\vec{r})\nabla N_j(\vec{r}) - N_j(\vec{r})\nabla N_i(\vec{r}) \in H^1(\text{curl}; \Omega_h). \quad (4.38)$$

In a 2D Cartesian xy -plane, two types of edge functions are distinguished.

A transversal edge function $\vec{w}_e^{(t)}(x, y) : \mathbb{R}^2 \mapsto [0, 1] \times [0, 1] \times [0]$, $e = 1, \dots, N_e$, is associated to an edge $e = (i, j)$ in the mesh as shown in Fig. 4.3 as purple arrow. It follows the general expression (4.38)

$$\vec{w}_e^{(t)}(x, y) = N_i(x, y)\nabla N_j(x, y) - N_j(x, y)\nabla N_i(x, y). \quad (4.39)$$

Note that $\nabla = (\partial_x, \partial_y, \partial_z)^\top$ is the 3D gradient. However, as the 2D nodal shape functions do not depend on z , the third component of $\vec{w}_e^{(t)}$ is always zero.

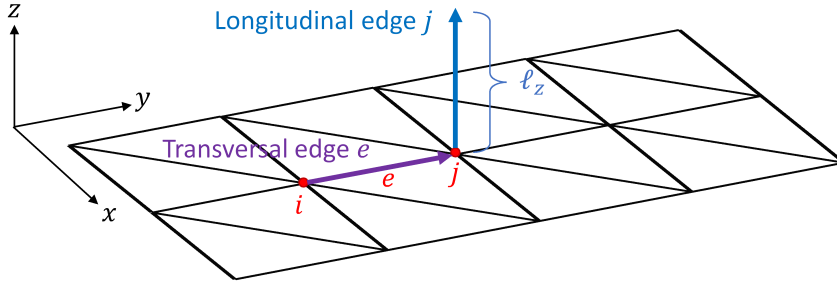


Figure 4.3.: Two types of edge functions in a 2D Cartesian mesh arise: Transversal (or tangential) edges (purple) are associated with the mesh edges e connecting two mesh nodes i and j (red). Meanwhile, longitudinal (or normal) edges (blue) perpendicularly emerge from the mesh nodes j into z -direction.

A longitudinal edge function $\vec{w}_j^{(\ell)}(x, y) : \mathbb{R}^2 \mapsto [0] \times [0] \times [0, 1]$, $j = 1, \dots, N_n$, is associated to an edge standing perpendicularly on a node j and pointing into positive z -direction, as shown in Fig. 4.3 as blue arrow. It is expressed in terms of nodal functions as

$$\vec{w}_j^{(\ell)}(x, y) = \frac{N_j(x, y)}{\ell_z} \vec{e}_z, \quad (4.40)$$

where \vec{e}_z is the unit vector in z -direction, and ℓ_z is the depth of the geometry, i.e. the length of the longitudinal edge.

As a consequence of this distinction, the MVP is approximated by a decomposition into a transversal component lying in the xy -plane and a longitudinal component pointing in z -direction,

$$\vec{A}(x, y; t) \approx \sum_{e=1}^{\mathcal{E}} \hat{a}_e^{(t)}(t) \vec{w}_e^{(t)}(x, y) + \sum_{j=1}^{\mathcal{J}} \hat{a}_j^{(\ell)}(t) \vec{w}_j^{(\ell)}(x, y) \quad (4.41)$$

where $\hat{a}_e^{(t)}$ and $\hat{a}_j^{(\ell)}$ are the transversal and longitudinal MVP coefficients, respectively.

Matrix Assembly

For the thermal system of equations (4.20), the 2D FE matrices and vectors (4.17), (4.18) and (4.19) read

$$\left(\mathbf{K}_\lambda^{\text{FE},n} \right)_{ij} = \int_{\Omega_h} \lambda(x, y) \nabla N_j(x, y) \cdot \nabla N_i(x, y) \, dx dy, \quad (4.42)$$

$$\left(\mathbf{M}_{C_V}^{\text{FE},n} \right)_{ij} = \int_{\Omega_h} C_V(x, y) N_j(x, y) N_i(x, y) \, dx dy, \quad (4.43)$$

$$\left(\mathbf{q}_V^{\text{FE}} \right)_i = \int_{\Omega_h} q_V(x, y) N_i(x, y) \, dx dy. \quad (4.44)$$

For the magnetic systems of equation (4.26), in the case of the transversal edge shape functions, the matrices (4.21)–(4.24) read

$$(\mathbf{K}_c^{\text{FE,t}})_{de} = \int_{\Omega_h} c(x, y) \nabla \times \vec{w}_e^{(t)}(x, y) \cdot \nabla \times \vec{w}_d^{(t)}(x, y) \, dx dy, \quad (4.45)$$

$$(\mathbf{M}_\sigma^{\text{FE,t}})_{de} = \int_{\Omega_h} \sigma(x, y) \vec{w}_e^{(t)}(x, y) \cdot \vec{w}_d^{(t)}(x, y) \, dx dy, \quad (4.46)$$

$$(\mathbf{C}_1^{\text{FE,t}})_{ie} = \int_{\Omega_h} \vec{w}_e^{(t)}(x, y) \cdot \nabla N_i(x, y) \, dx dy, \quad (4.47)$$

$$(\mathbf{X}_\sigma^{\text{FE,t}})_{dw} = 0. \quad (4.48)$$

Here, the transversal winding matrix (4.48) is zero, since the scalar product between the transversal edge shape function (lying in the xy -plane) and the voltage distribution function $\vec{\xi}_w$ (pointing in z -direction) is zero. The material parameter c is substituted either with ν or $\nu\tau$. In the case of longitudinal edge shape functions, the matrices read

$$(\mathbf{K}_c^{\text{FE},\ell})_{ij} = \int_{\Omega_h} c(x, y) \nabla N_j(x, y) \cdot \nabla N_i(x, y) \ell_z^{-2} \, dx dy, \quad (4.49)$$

$$(\mathbf{M}_\sigma^{\text{FE},\ell})_{ij} = \int_{\Omega_h} \sigma(x, y) N_j(x, y) N_i(x, y) \ell_z^{-2} \, dx dy, \quad (4.50)$$

$$(\mathbf{C}_1^{\text{FE},\ell})_{i'j} = 0, \quad (4.51)$$

$$(\mathbf{X}_\sigma^{\text{FE},\ell})_{iw} = \int_{\Omega_h} \sigma(x, y) T_w(x, y) N_i(x, y) \ell_z^{-2} \, dx dy. \quad (4.52)$$

Here, the node-edge coupling matrix $\mathbf{C}_1^{\text{FE},\ell}$ is a zero matrix, because the gradient term in (4.23) lies in the xy -plane and the longitudinal edge shape function points in z -direction. In contrast to the transversal case, the longitudinal winding matrix is not zero, since the longitudinal edge shape functions point in the same direction as the voltage distribution functions $\vec{\xi}_w$.

For the calculation of the matrices and vectors, the reference element approach is used [Bra12]. In this process, the integrals over Ω_h are expressed as sums of integrals over T in the image coordinate system. Then, they are transformed into integrals over the reference element \hat{T} in the reference coordinate system utilizing appropriate mapping theorems. The detailed calculations are left to Appendix A.1.

4.4. Second Ingredient: 1D Spectral Element Method

Consider the general 1D BVP

$$-\alpha(z)\partial_z^2 u(z) + \beta(z)\partial_z u(z) + \gamma(z)u(z) = f(z) \quad \text{in } I = [0, \ell_z], \quad (4.53a)$$

$$u(0) = 0, \quad (4.53b)$$

$$u(\ell_z) = 0, \quad (4.53c)$$

with an unknown function $u(z)$, parameters $\alpha(z), \beta(z), \gamma(z) \geq 0$ and a known right-hand side $f(z)$. Following the procedure in Sec. 4.1, the weak formulation reads

$$\left\{ \begin{array}{l} \text{Find } u(z) \in \mathcal{P} \text{ s.t.} \\ \int_I \alpha(z)\partial_z u(z)\partial_z v(z) dz + \int_I \beta(z)\partial_z u(z)v(z) dz + \int_I \gamma(z)u(z)v(z) dz \\ = \int_I f(z)v(z) dz \quad \forall v(z) \in \mathcal{P}' \end{array} \right. \quad (4.54)$$

with test functions $v(z)$, the solution function space \mathcal{P} and the test function space \mathcal{P}' . To solve this BVP with the SEM, the interval I is partitioned in N_{SE} subintervals $I_k = [z_k, z_{k+1}] \subset I$ called spectral elements (SE). The solution is expanded on an element I_k in terms of polynomials $p_q^k(z) \in \mathcal{P}_0^N$ of order q as [STW11]

$$u(z) \approx \sum_{q=1}^Q \tilde{u}_q^k p_q^k(z) \quad \forall k \quad (4.55)$$

with Q as the total number of considered polynomial orders and the function space

$$\mathcal{P}_0^N = \left\{ p_q^k(z) \in H_0^1(I_k) : p_q^k(z) \text{ is a polynomial of order } q \leq N \right\} \quad (4.56)$$

of element-wise continuous polynomials $p_q^k(z)$ with a maximal order N . While the coefficients in the linear FEM discretization are nodal, i.e., they represent directly the physical values at the DoFs, the coefficients \tilde{u}_q^k are in general modal [STW11], i.e., they do not represent physical values (e.g. the temperature), but the weight of the q -th polynomial mode $p_q^k(z)$ in element k .

With this definition, the polynomials are not necessarily continuous along the interval I . However, a correct representation of the temperature and the MVP needs at least C^0 -continuity along z . Therefore, either the continuity has to be imposed or appropriate polynomials $p_q^k(z)$ have to be chosen such that this continuity is intrinsically given.

The SEM differs from the FEM also in the choice of the inner product. As the SEM relies on orthogonality properties of the employed polynomials, a polynomial-dependent weighting function $w(z)$ is required within the inner product to fulfill the orthogonality relation [STW11].

This yields the discrete weak formulation

$$\left\{ \begin{array}{l} \text{Find } \tilde{u}_q^k, q = 1, \dots, Q, k = 1, \dots, N_{\text{SE}} \text{ s.t.} \\ \sum_q \tilde{u}_q^k \left[\int_I \alpha(z) \partial_z p_q^k(z) \partial_z (p_p^k(z) w(z)) dz + \int_I \beta(z) \partial_z p_q^k(z) p_p^k(z) w(z) dz \right. \\ \left. + \int_I \gamma(z) p_q^k(z) p_p^k(z) w(z) dz \right] = \int_I f(z) p_p^k(z) w(z) dz \quad \forall p_p^k(z) w(z) \in \mathcal{P}_0^N. \end{array} \right. \quad (4.57)$$

This leads to the discrete system of equations

$$(\mathbf{K}_\alpha^{\text{SE}} + \mathbf{D}_\beta^{\text{SE}} + \mathbf{M}_\gamma^{\text{SE}}) \tilde{\mathbf{u}} = \tilde{\mathbf{f}} \quad (4.58)$$

with

$$(\mathbf{K}_\alpha^{\text{SE}})_{pq}^{(k)} = \int_I \alpha(z) \partial_z p_q^k(z) \partial_z p_p^k(z) w(z) dz \quad \text{spectral stiffness matrix,} \quad (4.59)$$

$$(\mathbf{D}_\beta^{\text{SE}})_{pq}^{(k)} = \int_I \beta(z) \partial_z p_q^k(z) p_p^k(z) w(z) dz \quad \text{spectral damping matrix,} \quad (4.60)$$

$$(\mathbf{M}_\gamma^{\text{SE}})_{pq}^{(k)} = \int_I \gamma(z) p_q^k(z) p_p^k(z) w(z) dz \quad \text{spectral mass matrix,} \quad (4.61)$$

$$(\tilde{\mathbf{f}})_p^{(k)} = \int_I f(z) p_p^k(z) w(z) dz \quad \text{spectral load vector,} \quad (4.62)$$

and a vector $\tilde{\mathbf{u}}$ collecting the solution coefficients [STW11].

The choice of the polynomials $p_q^k(z)$ determines the structure of the matrices and the properties of the approximation for $u(z)$. Ideally, the chosen polynomial basis fulfills the following requirements:

1. To achieve a high computational efficiency, the polynomial basis produces
 - a) sparse matrices (4.59), (4.60) and (4.61)
 - b) with closed form expressions.
2. To correctly represent the physics and avoid imposing additional constraints, the polynomial basis intrinsically fulfills C^0 -continuity across the SE interfaces.
3. The polynomial basis enables an easy incorporation of boundary conditions without the need to manipulate multiple polynomial modes \tilde{u}_q^k .
4. The polynomial basis has a weighting function $w(z) \equiv 1$ leading to easier calculations.

Table 4.1 compares the Lagrange, Legendre, Chebyshev, Lobatto and modified Lobatto polynomial bases regarding those requirements [STW11], [FD15]. Note that although the Lagrange polynomial basis fulfills almost all requirements and is a popular choice for SEMs as it leads to a diagonal mass matrix [KT99], it heavily violates the sparsity requirement as it produces a fully populated stiffness matrix $\mathbf{K}_\alpha^{\text{SE}}$. This would fatally reduce the computational efficiency of the Q3D method, thus disqualifying the Lagrange polynomials for utilization in the Q3D discretization.

Table 4.1.: Comparison between different polynomial bases w.r.t the requirements described in Section 4.4. A green checkmark indicates complete fulfillment, a yellow checkmark partial fulfillment, and a red cross non-fulfillment.

Requirement	Lagrange	Legendre	Chebyshev	Lobatto	Mod. Lobatto
(1a) Sparse matrices	✗	✓	✓	✓	✓
(1b) Closed form	✓	✓	✓	✓	✓
(2) C^0 -continuity	✓	✗	✗	✗	✓
(3) Easy BC incorporation	✓	✗	✗	✗	✓
(4) $w(z) \equiv 1$	✓	✓	✗	✗	✓

Eventually, only the modified Lobatto polynomials meet all requirements simultaneously. Hence, they are introduced in detail in the following.

Modified Lobatto Polynomials

The Lobatto polynomial of q -th order is defined as [Poz14]

$$\text{LO}_q(\hat{z}) = L'_{q+1}(\hat{z}), \quad (4.63)$$

with $\hat{z} \in \hat{I} = [-1, 1]$ where L'_{q+1} is the derivative of the Legendre polynomial of $(q + 1)$ -th order. Lobatto polynomials are orthogonal on the interval $\hat{I} = [-1, 1]$ [FD15],

$$\int_{\hat{I}} \text{LO}_p(\hat{z})\text{LO}_q(\hat{z})w(\hat{z})d\hat{z} = \frac{2(p+1)(p+2)}{2p+3}\delta_{pq}, \quad (4.64)$$

with a weight function

$$w(\hat{z}) = 1 - \hat{z}^2 \quad (4.65)$$

and the Kronecker delta defined as

$$\delta_{pq} = \begin{cases} 1, & p = q, \\ 0, & p \neq q. \end{cases} \quad (4.66)$$

The modified Lobatto polynomials on the reference interval $\hat{I} = [-1, 1]$ are defined in terms of Lobatto polynomials (4.63) as [FD15]

$$\hat{\phi}_q(\hat{z}) = \begin{cases} \frac{1-\hat{z}}{2}, & q = 1, \\ \frac{1-\hat{z}^2}{4}\text{LO}_{q-2}(\hat{z}), & q = 2, \dots, N, \\ \frac{1+\hat{z}}{2}, & q = N + 1, \end{cases} \quad (4.67)$$

where N is the maximal polynomial order. Using the derivate relation, which links the Lobatto polynomials LO_{q-1} of order $(q - 1)$ to the Legendre polynomials L_q of q -th order [FD15],

$$\partial_{\hat{z}}((\hat{z}^2 - 1)\text{LO}_{q-1}(\hat{z})) = q(q+1)L_q(\hat{z}), \quad (4.68)$$

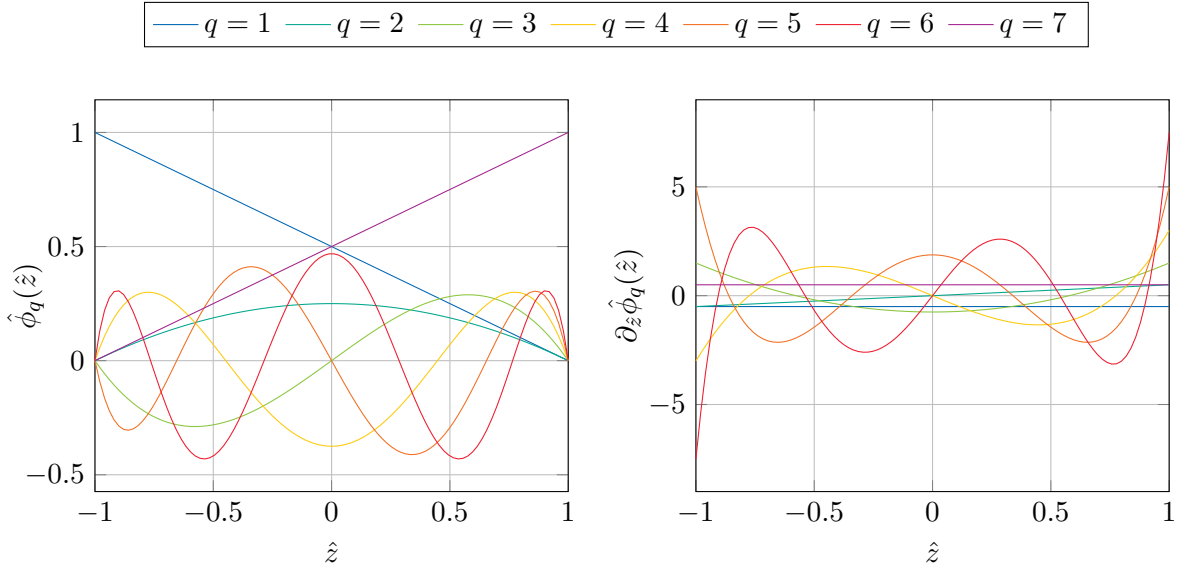


Figure 4.4.: Modified Lobatto polynomials (4.67) (left) and their derivatives (4.69) (right) for $N = 6$ on the reference interval.

the derivatives of (4.67) are obtained [FD15],

$$\partial_z \hat{\phi}_q(\hat{z}) = \begin{cases} -\frac{1}{2}, & q = 1, \\ -\frac{q(q-1)}{4} L_{q-1}(\hat{z}), & q = 2, \dots, N, \\ +\frac{1}{2}, & q = N + 1. \end{cases} \quad (4.69)$$

Figure 4.4 shows the modified Lobatto polynomials (4.67) and their derivative (4.69) for $N = 6$ on the reference interval. Here, two types of modes q can be distinguished:

- The boundary modes $q = 1$ and $q = N + 1$ are described by hat functions and are therefore nodal, i.e. the corresponding coefficients \tilde{u}_1^k and \tilde{u}_{N+1}^k represent the actual physical values at z_k and z_{k+1} , respectively.
- The inner modes $q = 2, \dots, N$ are expressed in terms of Lobatto polynomials, and are therefore modal. The orthogonality property (4.64) of the Lobatto polynomials leads to low interactions between themselves and, thus, sparse inner matrices.

Through the nodal property of the boundary modes, C^0 -continuity between two neighboring elements I_k and I_{k+1} is automatically imposed by setting

$$\tilde{u}_{N+1}^k = \tilde{u}_1^{k+1}. \quad (4.70)$$

Due to the compact support of $\phi_q^{(k)}$ on the k -th SE, the q -th global SE modified Lobatto shape function can be defined as the sum of the local shape functions,

$$\phi_q(z) = \sum_{k=1}^{N_{SE}} \phi_q^{(k)}(z). \quad (4.71)$$

A function $f(z)$ can be expanded in terms of modified Lobatto polynomials of maximal polynomial order N as

$$f(z) \approx \sum_{m=1}^{N+1} \tilde{f}_m \phi_m(z). \quad (4.72)$$

The spectral coefficients \tilde{f}_m are collected in a vector $\tilde{\mathbf{f}}$, which is calculated by a forward transform,

$$\tilde{\mathbf{f}} = \mathbf{V}^{-1} \mathbf{f}, \quad (4.73)$$

where

$$(\mathbf{V})_{ij} = \hat{\phi}_j(z_i^{(\text{LGL})}) \quad (4.74)$$

is the Vandermonde matrix [Poz14] of the modified Lobatto polynomials, $z_i^{(\text{LGL})}$ are the Legendre-Gauss-Lobatto (LGL) nodes, which are obtained by the Newton method [STW11] using an approximation by [Let78] as initial guess, and

$$(\mathbf{f})_i = f(z_i^{(\text{LGL})}) \quad (4.75)$$

collects the function evaluations of $f(z)$ at the LGL nodes. To recover the function $f(z)$ from given spectral coefficients $\tilde{\mathbf{f}}$, the Vandermonde matrix is utilized for a backward transform,

$$\mathbf{f} = \mathbf{V} \tilde{\mathbf{f}}, \quad (4.76)$$

delivering the evaluations of $f(z)$ at the LGL nodes. Both the forward and backward transforms (4.73) and (4.76) have to be performed for each SE individually.

Linear Spectral Matrices

Using the modified Lobatto polynomials, the element-wise spectral stiffness matrix

$$(\mathbf{K}_\alpha^{\text{SE}})^{(k)}_{pq} = \int_{I_k} \alpha^{(k)} \partial_z \phi_q^{(k)}(z) \partial_z \phi_p^{(k)}(z) dz \quad (4.77)$$

is an inner diagonal matrix with four additional outer entries, resulting into maximal $(N + 3)$ non-zero entries per element in total. The element-wise spectral damping matrix

$$(\mathbf{D}_\beta^{\text{SE}})^{(k)}_{pq} = \int_{I_k} \beta^{(k)} \partial_z \phi_q^{(k)}(z) \phi_p^{(k)}(z) dz \quad (4.78)$$

is an inner two-banded matrix with diagonals below and above the main diagonal and with eight additional entries. Thus, this matrix has a total of maximal $(2N + 4)$ non-zero entries. The element-wise spectral mass matrix

$$(\mathbf{M}_\gamma^{\text{SE}})^{(k)}_{pq} = \int_{I_k} \gamma^{(k)} \phi_q^{(k)}(z) \phi_p^{(k)}(z) dz \quad (4.79)$$

is an inner tridiagonal matrix with twelve additional outer entries, such that this matrix has a total of maximal $(3N + 7)$ non-zero entries. All in all, this confirms that the usage of modified Lobatto

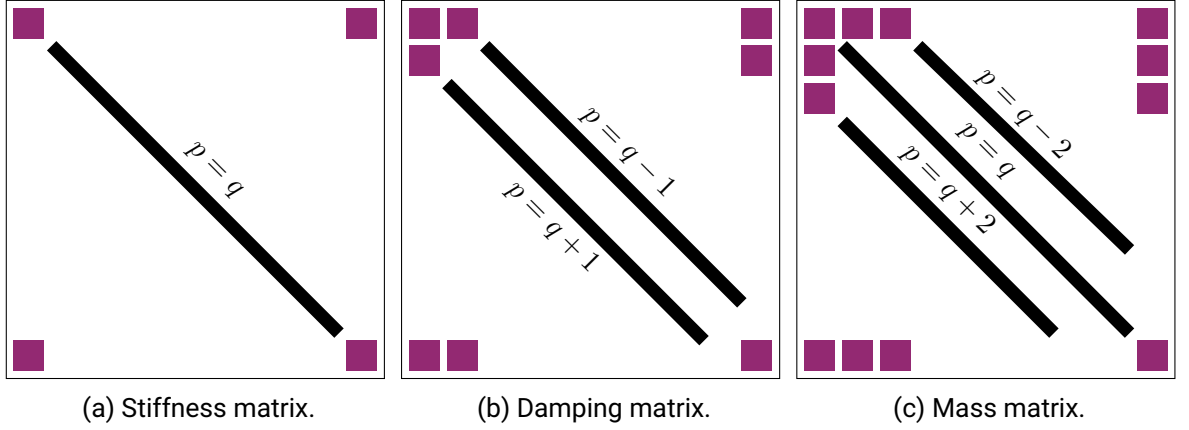


Figure 4.5.: Sparse structure of element-wise spectral matrices with modified Lobatto polynomial basis and element-wise constant material parameters. The purple squares indicate outer entries produced by boundary modes or interactions with boundary modes, while the black lines represent the inner diagonals generated by the inner modes.

polynomials as SE basis functions leads to highly sparse matrices. The described sparsity patterns of (4.77)–(4.79) are shown in Fig. 4.5, where the outer entries generated by the boundary modes are colored in purple, while the inner bands produced by the inner modes are visualized by black lines. The closed forms of (4.77)–(4.79) are given in Appendix A.2.

Nonlinear Spectral Matrices

In the case of a nonlinear material relation, e.g. a temperature-dependent thermal conductivity $\lambda = \lambda(\vartheta)$, the material function is forward transformed in terms of polynomials $\psi_m^{(k)}$ yielding corresponding spectral coefficients $\tilde{\lambda}_m^{(k)}$,

$$\lambda(z) \approx \sum_{m=0}^N \tilde{\lambda}_m^{(k)} \psi_m^{(k)}(z) \quad \forall k. \quad (4.80)$$

Thus, the nonlinear element-wise spectral stiffness, damping and mass matrices are calculated by a polynomial triple product integral,

$$(\mathbf{K}_\alpha^{\text{SE}})^{(k)}_{pq} = \sum_{m=0}^N \tilde{\alpha}_m^{(k)} \int_{I_k} \psi_m^{(k)}(z) \partial_z \phi_q^{(k)}(z) \partial_z \phi_p^{(k)}(z) dz, \quad (4.81)$$

$$(\mathbf{D}_\beta^{\text{SE}})^{(k)}_{pq} = \sum_{m=0}^N \tilde{\beta}_m^{(k)} \int_{I_k} \psi_m^{(k)}(z) \partial_z \phi_q^{(k)}(z) \phi_p^{(k)}(z) dz, \quad (4.82)$$

$$(\mathbf{M}_\gamma^{\text{SE}})^{(k)}_{pq} = \sum_{m=0}^N \tilde{\gamma}_m^{(k)} \int_{I_k} \psi_m^{(k)}(z) \phi_q^{(k)}(z) \phi_p^{(k)}(z) dz. \quad (4.83)$$

In general, it is very difficult if not impossible to find a closed form for such polynomial triple product integrals [GN07]. Numerical integration or semi-analytical computation tools have to be utilized.

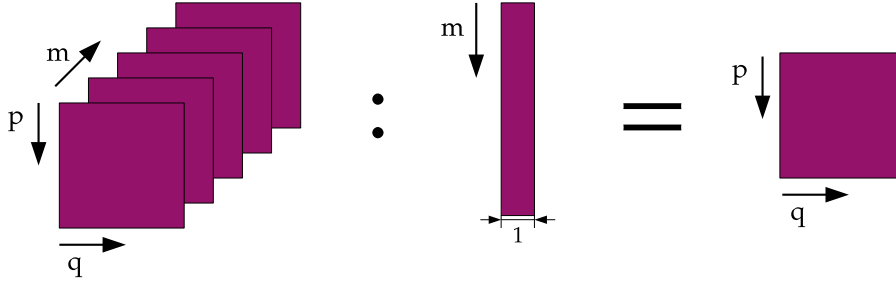


Figure 4.6.: Concept of the tensor contraction used to calculate the nonlinear spectral matrices: The tensor contraction of a third order tensor with entries (p, q, m) with a vector with entries m on the left-hand side yields a matrix with entries (p, q) on the right-hand side.

Performing a numerical integration in each nonlinear iteration, however, is computationally very demanding. Therefore, an approach originating in the efficient implementation of higher-order FEM is employed [KL07]: For a fixed order N , the third order reference tensors

$$(\mathcal{K}^{\text{SE}})_{mpq} = \int_{\hat{I}} \psi_m(\hat{z}) \partial_{\hat{z}} \hat{\phi}_q(\hat{z}) \partial_{\hat{z}} \hat{\phi}_p(\hat{z}) d\hat{z}, \quad (4.84)$$

$$(\mathcal{D}^{\text{SE}})_{mpq} = \int_{\hat{I}} \psi_m(\hat{z}) \partial_{\hat{z}} \hat{\phi}_q(\hat{z}) \hat{\phi}_p(\hat{z}) d\hat{z}, \quad (4.85)$$

$$(\mathcal{M}^{\text{SE}})_{mpq} = \int_{\hat{I}} \psi_m(\hat{z}) \hat{\phi}_q(\hat{z}) \hat{\phi}_p(\hat{z}) d\hat{z}, \quad (4.86)$$

are computed using semi-analytical integration. This computation is performed only once, after which the reference tensors are stored in a database. Note that (4.84)–(4.86) do not contain any geometry or material information.

Next, the material function λ is evaluated along z for the current working point u , and the spectral material coefficients $\tilde{\lambda}_m^{(k)}$ are calculated in terms of the polynomials $\psi_m^{(k)}$ for each SE $k = 1, \dots, N_{\text{SE}}$. This yields a spectral material coefficient vector $\tilde{\lambda}^{(k)} \in \mathbb{R}^N$ for each SE k . Then, the element-wise nonlinear spectral matrices are obtained by a tensor contraction [KL07],

$$(\mathbf{K}_{\alpha}^{\text{SE}})^{(k)} = \mathcal{K}^{\text{SE}} : \tilde{\alpha}^{(k)} b_k^{-1}, \quad (4.87)$$

$$(\mathbf{D}_{\beta}^{\text{SE}})^{(k)} = \mathcal{D}^{\text{SE}} : \tilde{\beta}^{(k)}, \quad (4.88)$$

$$(\mathbf{M}_{\gamma}^{\text{SE}})^{(k)} = \mathcal{M}^{\text{SE}} : \tilde{\gamma}^{(k)} b_k, \quad (4.89)$$

where the geometrical information is included through mapping coefficients b_k , see Appendix A.2. Basically, the tensor contraction operator $:$ performs the sum operation in (4.81)–(4.83) in an efficient way, as shown in Fig. 4.6.

Finally, one last question remains: Which polynomials $\psi_m^{(k)}$ are optimal for this tensor contraction approach? As the polynomial triple product integrals are calculated on beforehand, the focus for answering this question should be placed on the efficient computation of the spectral material coefficients $\tilde{\lambda}_m^{(k)}$. Therefore, Chebyshev polynomials T_m are the ideal choice because the corre-

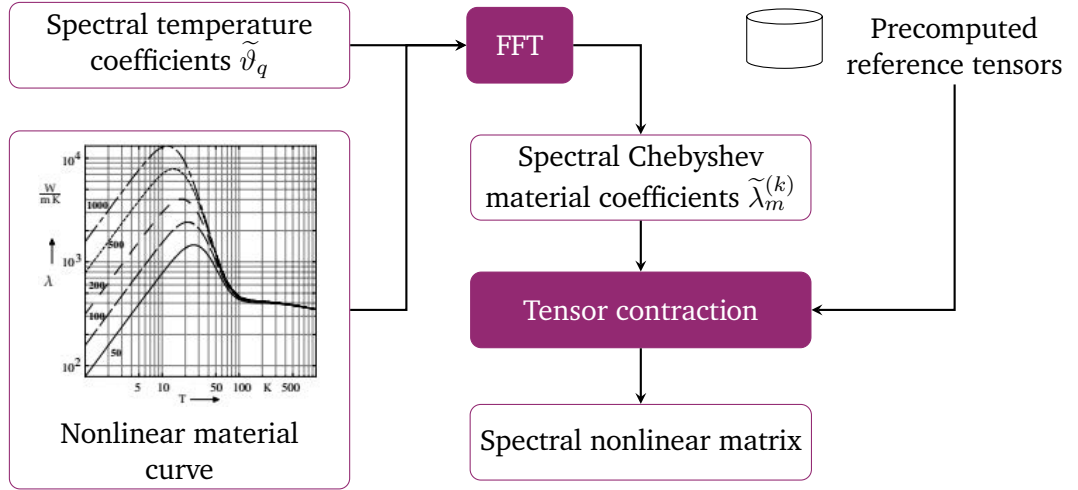


Figure 4.7.: Efficient scheme to assemble the nonlinear SE matrices: The nonlinear material curve is evaluated at the current working point using the spectral temperature coefficients. By employing a FFT, the spectral Chebyshev material coefficients are obtained. In a tensor contraction operation with precomputed reference tensors, the spectral nonlinear matrix is finally computed. Material curve taken from [Rus10].

sponding spectral coefficients can be computed efficiently using a Fast Fourier Transform (FFT) or a Discrete Cosine Transform (DCT) [Mak80; STW11]. To this end, four steps are performed:

1. The nonlinear material curve is evaluated at the current working point $\tilde{\vartheta}^{(k+1)}$.
2. Using FFT or DCT, the spectral Chebyshev material coefficients are calculated.
3. Precomputed reference tensors are tensor-contracted with the material coefficient vector to compute the element-wise nonlinear spectral matrices.
4. The element-wise nonlinear spectral matrices are assembled to a global SE matrix.

This procedure is visualized in the scheme seen in Fig. 4.7.

4.5. Seasoning: Field-Circuit Coupling

For the quench simulation, a field-circuit coupling approach [SDW13] is applied to include coil end effects by using end winding models, see Sec. 3.5. With this, an external circuit is also taken into account, to which the superconducting coil is connected. In this work, a very simple external circuit is considered, where the coil is connected to a voltage source u_{src} at Γ_1^+ , and to ground at Γ_w^+ , see Fig. 3.5. Furthermore, the end windings are linked to each other by ideal electrical connections, as shown in Fig. 3.5. The resulting electrical circuit is seen in Fig. 4.8. Here, the half-turns are modeled as solid conductors, meaning that the voltage drop along the w -th half-turn is applied as a potential difference between the end winding interfaces Γ_w^\pm [SDW13],

$$u_w(t) = \phi_{w+1}(t) - \phi_w(t). \quad (4.90)$$

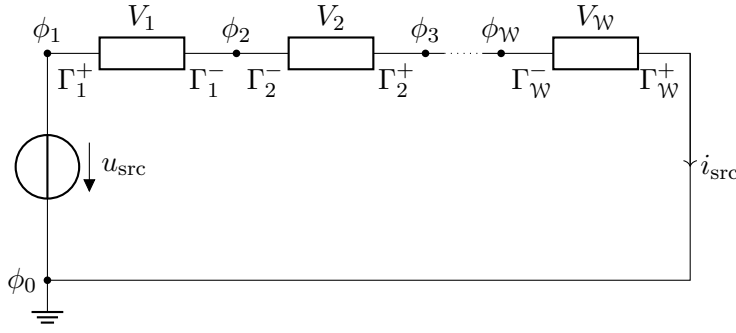


Figure 4.8.: Schematic of a simple superconducting coil circuit. The half-turns V_w are modeled as solid conductors and connected in series at their surfaces Γ_w^\pm to a voltage source, the ground and each other, respectively.

For all voltage drops $u_w, w = 1, \dots, W$, this relation is expressed in a discrete form as

$$\mathbf{u}_{\text{sol}}(t) = \mathbf{A}_{\text{sol}}^\top \boldsymbol{\phi}(t), \quad (4.91)$$

where the vectors \mathbf{u}_{sol} and $\boldsymbol{\phi}$ collect the voltage drops u_w and circuit node potentials ϕ_w , respectively. \mathbf{A}_{sol} is an incidence matrix with respect to the solid conductors V_w [SDW13]. By following Kirchhoff's law and rewriting for the nodal potentials [SDW13], the circuit equations

$$\mathbf{A}_V \mathbf{i}_V(t) - \mathbf{A}_{\text{sol}} \mathbf{X}_\sigma^\top \hat{\mathbf{a}}(t) + \mathbf{A}_{\text{sol}} \mathbf{G}_\sigma \mathbf{A}_{\text{sol}}^\top \boldsymbol{\phi}(t) = \mathbf{0} \quad (4.92a)$$

$$\mathbf{A}_V^\top \boldsymbol{\phi}(t) = u_{\text{src}}(t) \quad (4.92b)$$

are obtained, where \mathbf{A}_V is an incidence matrix selecting the voltage source in the circuit, and \mathbf{i}_V is the vector of voltage source currents. This approach is known as a modified nodal analysis (MNA) [SDW13]. Combining the circuit equations (4.92) with the MQS field equations (4.26) by using (4.91) yields the semi-discrete field-circuit coupled system of equations

$$\begin{bmatrix} \mathbf{M}_\sigma^e + \mathbf{K}_{\nu\tau}^e & \mathbf{0} & \mathbf{0} & \mathbf{0} \\ -\mathbf{X}_\sigma^\top & \mathbf{0} & \mathbf{0} & \mathbf{0} \\ \mathbf{0} & \mathbf{0} & \mathbf{0} & \mathbf{0} \\ \mathbf{0} & \mathbf{0} & \mathbf{0} & \mathbf{0} \end{bmatrix} \frac{d}{dt} \begin{bmatrix} \hat{\mathbf{a}} \\ \boldsymbol{\phi} \\ \mathbf{i}_V \\ \zeta \end{bmatrix} + \begin{bmatrix} \mathbf{K}_\nu^e & -\mathbf{X}_\sigma \mathbf{A}_{\text{sol}}^\top & \mathbf{0} & \mathbf{C}_1^\top \\ \mathbf{0} & \mathbf{A}_{\text{sol}} \mathbf{G}_\sigma \mathbf{A}_{\text{sol}}^\top & \mathbf{A}_V & \mathbf{0} \\ \mathbf{0} & -\mathbf{A}_V^\top & \mathbf{0} & \mathbf{0} \\ \mathbf{C}_1 & \mathbf{0} & \mathbf{0} & \mathbf{0} \end{bmatrix} \begin{bmatrix} \hat{\mathbf{a}} \\ \boldsymbol{\phi} \\ \mathbf{i}_V \\ \zeta \end{bmatrix} = \begin{bmatrix} \mathbf{0} \\ \mathbf{0} \\ -u_{\text{src}} \\ \mathbf{0} \end{bmatrix}. \quad (4.93)$$

Of course, this procedure can be expanded for multiple voltage sources, other linear lumped elements such as inductors and capacitors as well as nonlinear lumped elements [SDW13; Cor20].

5. Quasi-3D Method for Quench Simulation

"Either this is madness or it is Hell."
"It is neither," calmly replied the voice of
the Sphere, "it is Knowledge; it is Three
Dimensions: open your eye once again
and try to look steadily."

Edwin Abbott Abbott, *Flatland*

This chapter brings the numerical components of the previous chapter together to derive the Q3D method for the quench simulation of a superconducting magnet coil. Furthermore, the implementation of the Q3D method with focus on the structure of the implemented framework is presented.

5.1. Quasi-3D Discretization of the Magneto-Thermal Model

Index Notation

In the Q3D setting, a physical quantity is approximated with hybrid FE-SE shape functions, which are products of 2D FE and 1D SE shape functions. The 2D FE nodal and edge shape functions N_j and $\vec{w}_e^{(t)}$ are associated to FE DoFs such as the j -th node and the e -th edge, respectively, while the 1D SE shape functions ϕ_q are related to the q -th polynomial mode. This leads to a combined index jq corresponding to the q -th mode in the j -th node, and eq corresponding to the q -th mode in the e -th edge, respectively.

In practice, the entries are sorted per 2D FE DoF i , polynomial mode q and also SE k in a way that depends on the evaluation order of the FE and SE matrix products, leading to a global Q3D index $n(i, k, q)$. In the following, however, the discrete Q3D quantity entries are denoted with the combined index notation for the sake of comprehensibility and to underline the hybrid character of the Q3D discretization. The global Q3D index and the influence of the product evaluation order are discussed at the end of this section.

Quasi-3D Thermal Model

In the translational Q3D setting, the temperature is discretized with hybrid shape functions consisting of products between 2D FE nodal functions (4.34) and modified Lobatto polynomials (4.67),

$$\vartheta(\vec{r}, t) \approx \sum_{j=1}^{N_n} \sum_{q=1}^{N+1} \vartheta_{jq}(t) N_j(x, y) \phi_q(z). \quad (5.1)$$

Herein, N_n is the total number of nodes in the 2D FE mesh, and N is the maximal polynomial order of the modified Lobatto polynomials. This discretization is applied to the thermal weak

formulation (4.6). The test function is composed as

$$\vartheta^l(\vec{r}, t) \approx N_i(x, y) \phi_p(z). \quad (5.2)$$

Both the ansatz and test functions are thus from $\mathcal{U}_h = H_0^1(\Omega_h) \times \mathcal{P}_0^N(I)$, which is the product of the corresponding 2D FE nodal and 1D SE function spaces. The gradient of (5.1) is computed to

$$\begin{aligned} \nabla \vartheta(\vec{r}, t) &\approx \sum_{jq} \vartheta_{jq}(t) \nabla (N_j(x, y) \phi_q(z)) \\ &= \sum_{jq} \vartheta_{jq}(t) \begin{bmatrix} \nabla_{xy} N_j(x, y) \phi_q(z) \\ N_j(x, y) \partial_z \phi_q(z) \end{bmatrix}, \end{aligned} \quad (5.3)$$

with $\nabla_{xy} = [\partial_x, \partial_y]^\top$ as the 2D Nabla operator in the xy -plane and \sum_{jq} as abbreviation for the double sum $\sum_{j=1}^{N_n} \sum_{q=1}^N$. Naturally by definition of the Q3D shape function, the derivatives in x and y affect only the FE part, while the derivative in z affects only the SE part. Thus, the weak heat conduction equation becomes

$$\begin{aligned} \sum_{jq} \vartheta_{jq} \int_{V_h} \lambda \begin{bmatrix} \nabla_{xy} N_j \phi_q \\ N_j \partial_z \phi_q \end{bmatrix} \cdot \begin{bmatrix} \nabla_{xy} N_i \phi_p \\ N_i \partial_z \phi_p \end{bmatrix} dV + \sum_{jq} \frac{d\vartheta_{jq}}{dt} \int_{V_h} C_V N_j \phi_q N_i \phi_p dV \\ = (\mathbf{K}_\lambda^{\text{Q3D}})_{ijpq} = (\mathbf{M}_{C_V}^{\text{Q3D}})_{ijpq} \\ = \int_{V_h} q_V N_i \phi_p dV, \\ = (\mathbf{q}_V^{\text{Q3D}})_{ip} \end{aligned} \quad (5.4)$$

where the temporal and spatial dependencies are left out for the sake of readability. Next, the volume integral over the computational domain V_h is decomposed into a surface integral over the 2D cross-section Ω_h and a line integral over the 1D interval I . Furthermore, it is assumed that the material parameter can be split into a transversal part $\lambda^{(t)}$ and a longitudinal part $\lambda^{(\ell)}$ as

$$\lambda(x, y, z) = \lambda^{(t)}(x, y) \lambda^{(\ell)}(z). \quad (5.5)$$

This assumption is necessary to pull apart the volume integrals into transversal and longitudinal integrals, such that the stiffness term in (5.4) reads

$$\begin{aligned} (\mathbf{K}_\lambda^{\text{Q3D}})_{ijpq} &= \underbrace{\int_I \lambda^{(\ell)} \phi_q \phi_p dz}_{=(\mathbf{M}_\lambda^{\text{SE}})_{pq}} \underbrace{\int_{\Omega_h} \lambda^{(t)} \nabla_{xy} N_j \cdot \nabla_{xy} N_i dxdy}_{=(\mathbf{K}_\lambda^{\text{FE,n}})_{ij}} \\ &+ \underbrace{\int_I \lambda^{(\ell)} \partial_z \phi_q \partial_z \phi_p dz}_{=(\mathbf{K}_\lambda^{\text{SE}})_{pq}} \underbrace{\int_{\Omega_h} \lambda^{(t)} N_j N_i dxdy}_{=(\mathbf{M}_\lambda^{\text{FE,n}})_{ij}} \end{aligned} \quad (5.6)$$

The integrals are identified with the 2D FE nodal stiffness and mass matrix (4.42) and (4.43), and the 1D SE stiffness and mass matrix (4.77) and (4.79), respectively. By using the Kronecker tensor product notation [Loa00], the Q3D nodal stiffness matrix is obtained by

$$\mathbf{K}_\lambda^{\text{Q3D},n} = \mathbf{M}_\lambda^{\text{SE}} \otimes \mathbf{K}_\lambda^{\text{FE},n} + \mathbf{K}_\lambda^{\text{SE}} \otimes \mathbf{M}_\lambda^{\text{FE},n}. \quad (5.7)$$

In the same way, the mass term in (5.4) is expressed by

$$\left(\mathbf{M}_{C_V}^{\text{Q3D}} \right)_{ijpq} = \underbrace{\int_I C_V^{(\ell)} \phi_q \phi_p dz}_{= (\mathbf{M}_{C_V}^{\text{SE}})_{pq}} \underbrace{\int_{\Omega_h} C_V^{(t)} N_j N_i dx dy}_{= (\mathbf{M}_{C_V}^{\text{FE},n})_{ij}}, \quad (5.8)$$

and is computed in a Kronecker tensor product of the 1D SE mass matrix (4.79) and the 2D FE nodal mass matrix (4.43) by

$$\mathbf{M}_{C_V}^{\text{Q3D},n} = \mathbf{M}_{C_V}^{\text{SE}} \otimes \mathbf{M}_{C_V}^{\text{FE},n}. \quad (5.9)$$

The right-hand side term becomes

$$\left(\mathbf{q}_V^{\text{Q3D}} \right)_{ip} = \underbrace{\int_I q_V^{(\ell)} \phi_p dz}_{= \mathbf{q}_V^{\text{SE}}} \underbrace{\int_{\Omega_h} q_V^{(t)} N_i dx dy}_{= \mathbf{q}_V^{\text{FE},n}}, \quad (5.10)$$

such that the Q3D nodal load vector is obtained by

$$\mathbf{q}_V^{\text{Q3D},n} = \mathbf{q}_V^{\text{SE}} \otimes \mathbf{q}_V^{\text{FE},n}. \quad (5.11)$$

Finally, the semi-discrete thermal Q3D system of equations reads

$$\mathbf{K}_\lambda^{\text{Q3D},n} \boldsymbol{\vartheta} + \mathbf{M}_{C_V}^{\text{Q3D},n} \frac{d\boldsymbol{\vartheta}}{dt} = \mathbf{q}_V^{\text{Q3D},n}, \quad (5.12)$$

where the vector $\boldsymbol{\vartheta}$ collects the Q3D temperature coefficients ϑ_{jq} . Regarding the Q3D prism element shown in Fig. 5.1, these coefficients are associated to the prism's nodes. The dimension of the system is $N^{\text{Q3D},n} \times N^{\text{Q3D},n}$ with

$$N^{\text{Q3D},n} = N_n (NN_{\text{SE}} + 1), \quad (5.13)$$

which consists of the dimension of the nodal FE system N_n and the dimension of the SE system, $(NN_{\text{SE}} + 1)$. This number also coincides with the total number of temperature DoF. To obtain a full discrete system of equation, the temporal derivative in (5.12) has to be discretized as discussed in Sec. 4.2.

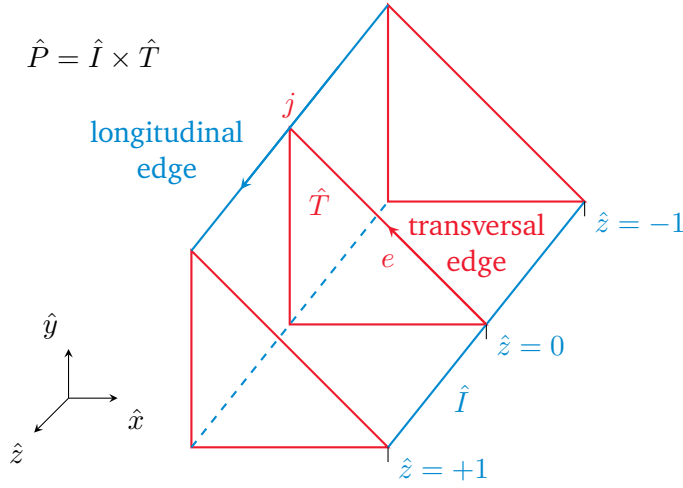


Figure 5.1.: Composition of the reference Q3D prism element $\hat{P} = \hat{I} \times \hat{T} = \{(0, 0), (0, 1), (1, 0)\}$ (red) and a reference 1D interval $\hat{I} = [-1, 1]$ (blue). The transversal edges e are associated to the triangle's edges; the longitudinal edges j are allocated along the prism's length. A longitudinal and transversal edge are exemplary shown as a blue and red arrow, respectively. Figure adapted from [DD21].

Quasi-3D Magnetic Model

The MVP is decomposed into a transversal component $\vec{A}^{(t)}$ lying in the xy -plane, and a longitudinal component $\vec{A}^{(\ell)}$ pointing in z -direction,

$$\vec{A}(\vec{r}, t) = \begin{bmatrix} \vec{A}^{(t)}(\vec{r}, t) \\ \vec{A}^{(\ell)}(\vec{r}, t) \end{bmatrix}. \quad (5.14)$$

$\vec{A}^{(t)}$ and $\vec{A}^{(\ell)}$ are separately discretized with hybrid shape functions consisting of the 2D FE transversal edge function (4.39) and the 2D FE longitudinal edge function (4.40), respectively, multiplied with modified Lobatto polynomials (4.67),

$$\vec{A}(\vec{r}, t) \approx \underbrace{\sum_{e=1}^{N_e} \sum_{q=1}^{N+1} \hat{a}_{eq}^{(t)}(t) \vec{w}_e^{(t)}(x, y) \phi_q(z)}_{\approx \vec{A}^{(t)}(\vec{r}, t)} + \underbrace{\sum_{j=1}^{N_n} \sum_{w=1}^{N+1} \hat{a}_{jw}^{(\ell)}(t) \vec{w}_j^{(\ell)}(x, y) \phi_w(z)}_{\approx \vec{A}^{(\ell)}(\vec{r}, t)} \quad (5.15)$$

Here, N_e denotes the total number of edges in the 2D FE mesh. In the Q3D context, $\vec{A}^{(t)}$ is then associated to a transversal edge, which belongs to a FE, while $\vec{A}^{(\ell)}$ is related to a longitudinal edge, which is associated to a node of the FE mesh and is oriented along the spectral mesh, see Fig. 5.1. In the context of the Q3D prism element P , $\vec{A}^{(t)}$ is allocated on its triangular cross-section, while $\vec{A}^{(\ell)}$ is allocated along the prism's length.

This discretization is applied to the magnetic weak formulation (4.12). The test function is composed as

$$\vec{A}'(\vec{r}, t) = \vec{w}_d^{(t)}(x, y) \phi_p(z) + \vec{w}_i^{(\ell)}(x, y) \phi_v(z). \quad (5.16)$$

Thus, both the ansatz and test functions belong to $\mathcal{V}_h = H_0(\text{curl}; \Omega_h) \times \mathcal{P}_0^N(I)$, which is the

product of the corresponding 2D FE edge and 1D SE function spaces. The curl of (5.15) reads

$$\begin{aligned}\nabla \times \vec{A}(\vec{r}, t) &\approx \sum_{ejqw} \nabla \times \begin{bmatrix} \widehat{a}_{eq}^{(t)}(t) w_{e,x}^{(t)}(x, y) \phi_q(z) \\ \widehat{a}_{eq}^{(t)}(t) w_{e,y}^{(t)}(x, y) \phi_q(z) \\ \widehat{a}_{jw}^{(\ell)}(t) N_j(x, y) \phi_w(z) \end{bmatrix} \\ &= \sum_{ejqw} \begin{bmatrix} \widehat{a}_{jw}^{(\ell)}(t) \partial_y N_j(x, y) \phi_w(z) - \widehat{a}_{eq}^{(t)}(t) w_{e,x}^{(t)}(x, y) \partial_z \phi_q(z) \\ \widehat{a}_{eq}^{(t)}(t) w_{e,x}^{(t)}(x, y) \partial_z \phi_q(z) - \widehat{a}_{jw}^{(\ell)}(t) \partial_x N_j(x, y) \phi_w(z) \\ \widehat{a}_{eq}^{(t)}(t) \left(\partial_x w_{e,y}^{(t)}(x, y) - \partial_y w_{e,x}^{(t)}(x, y) \right) \phi_q(z) \end{bmatrix}\end{aligned}\quad (5.17)$$

with the abbreviation \sum_{ejqw} for the quadruple sum $\sum_{e=1}^{N_e} \sum_{j=1}^{N_n} \sum_{q=1}^{N+1} \sum_{w=1}^{N+1}$ and by writing the longitudinal edge shape functions out as $\vec{w}_i^{(\ell)} = N_i \vec{e}_z$. In the following, the individual terms of the MQS formulation in the Q3D setting are investigated and put into a compact Kronecker tensor product form. For the sake of brevity, the spatial and temporal dependencies are left out. The Q3D curlcurl term of the weak MQS formulation reads

$$(\mathbf{K}_\nu^{\text{Q3D,e}})_{deijpqvw} = \int_{V_h} \nu \begin{bmatrix} \partial_y N_j \phi_w - w_{e,x}^{(t)} \partial_z \phi_q \\ w_{e,x}^{(t)} \partial_z \phi_q - \partial_x N_j \phi_w \\ \left(\partial_x w_{e,y}^{(t)} - \partial_y w_{e,x}^{(t)} \right) \phi_q \end{bmatrix} \cdot \begin{bmatrix} \partial_y N_i \phi_v - w_{d,x}^{(t)} \partial_z \phi_p \\ w_{d,x}^{(t)} \partial_z \phi_p - \partial_x N_i \phi_v \\ \left(\partial_x w_{d,y}^{(t)} - \partial_y w_{d,x}^{(t)} \right) \phi_p \end{bmatrix} dV. \quad (5.18)$$

Several terms arise from the scalar product in this integrand, which are compiled to

$$(\mathbf{K}_\nu^{\text{Q3D,e}})_{deijpqvw} = \underbrace{\int_I \nu^{(\ell)} \phi_q \phi_p dz}_{=(\mathbf{M}_\nu^{\text{SE}})_{pq}} \underbrace{\int_{\Omega_h} \nu^{(t)} \nabla_{xy} \times \vec{w}_e^{(t)} \cdot \nabla_{xy} \times \vec{w}_d^{(t)} dx dy}_{=(\mathbf{K}_\nu^{\text{FE,t}})_{de}} \quad (5.19a)$$

$$+ \underbrace{\int_I \nu^{(\ell)} \partial_z \phi_q \partial_z \phi_p dz}_{=(\mathbf{K}_\nu^{\text{SE}})_{pq}} \underbrace{\int_{\Omega_h} \nu^{(t)} \vec{w}_e^{(t)} \cdot \vec{w}_d^{(t)} dx dy}_{=(\mathbf{M}_\nu^{\text{FE,t}})_{de}} \quad (5.19b)$$

$$+ \underbrace{\int_I \nu^{(\ell)} \phi_w \phi_v dz}_{=(\mathbf{M}_\nu^{\text{SE}})_{vw}} \underbrace{\int_{\Omega_h} \nu^{(t)} \nabla_{xy} N_j \cdot \nabla_{xy} N_i dx dy}_{=(\mathbf{K}_\nu^{\text{FE,\ell}})_{ij}} \quad (5.19c)$$

$$- \underbrace{\int_I \nu^{(\ell)} \partial_z \phi_q \phi_v dz}_{=(\mathbf{D}_\nu^{\text{SE}})_{vq}} \underbrace{\int_{\Omega_h} \nu^{(t)} \vec{w}_e^{(t)} \cdot \nabla_{xy} N_i dx dy}_{=(\mathbf{C}_\nu^{\text{FE,t}})_{ie}} \quad (5.19d)$$

$$- \underbrace{\int_I \nu^{(\ell)} \phi_w \partial_z \phi_p dz}_{=(\mathbf{D}_\nu^{\text{SE}})_{pw}^\top} \underbrace{\int_{\Omega_h} \nu^{(t)} \nabla_{xy} N_j \cdot \vec{w}_d^{(t)} dx dy}_{=(\mathbf{C}_\nu^{\text{FE,t}})_{dj}^\top}. \quad (5.19e)$$

Again, the integrals in longitudinal direction are identified with 1D SE matrices, while the integrals

over the transversal cross-section are identified with 2D FE matrices. The integral products lead to Kronecker tensor products. With this, (5.19a) and (5.19b) form the Q3D transversal stiffness matrix,

$$\mathbf{K}_\nu^{\text{Q3D,t}} = \mathbf{M}_\nu^{\text{SE}} \otimes \mathbf{K}_\nu^{\text{FE,t}} + \mathbf{K}_\nu^{\text{SE}} \otimes \mathbf{M}_\nu^{\text{FE,t}}, \quad (5.20)$$

(5.19c) represents the Q3D longitudinal curlcurl matrix,

$$\mathbf{K}_\nu^{\text{Q3D,\ell}} = \mathbf{M}_\nu^{\text{SE}} \otimes \mathbf{K}_\nu^{\text{FE,\ell}}, \quad (5.21)$$

and (5.19d) and (5.19e) yield matrices coupling the transversal and longitudinal parts with each other,

$$\mathbf{C}_\nu^{\text{Q3D,t}\ell} = -\mathbf{D}_\nu^{\text{SE}} \otimes \mathbf{C}_\nu^{\text{FE,t}}, \quad (5.22)$$

$$\mathbf{C}_\nu^{\text{Q3D,\ell t}} = \left(\mathbf{C}_\nu^{\text{Q3D,t}\ell} \right)^\top. \quad (5.23)$$

In the end, the Q3D curlcurl matrix reads

$$\mathbf{K}_\nu^{\text{Q3D,e}} = \begin{bmatrix} \mathbf{K}_\nu^{\text{Q3D,t}} & \mathbf{C}_\nu^{\text{Q3D,t}\ell} \\ \left(\mathbf{C}_\nu^{\text{Q3D,t}\ell} \right)^\top & \mathbf{K}_\nu^{\text{Q3D,\ell}} \end{bmatrix}. \quad (5.24)$$

The Q3D edge-mass matrix reads

$$\left(\mathbf{M}_\sigma^{\text{Q3D,e}} \right)_{deijppqvw} = \int_{V_h} \sigma \begin{bmatrix} w_{e,x}^{(t)} \phi_q \\ w_{e,y}^{(t)} \phi_q \\ N_j \phi_w \end{bmatrix} \cdot \begin{bmatrix} w_{d,x}^{(t)} \phi_p \\ w_{d,y}^{(t)} \phi_p \\ N_i \phi_v \end{bmatrix} dV. \quad (5.25)$$

By expanding the scalar product, two terms arise, which are compactly expressed by

$$\left(\mathbf{M}_\sigma^{\text{Q3D,e}} \right)_{deijppqvw} = \underbrace{\int_I \sigma^{(\ell)} \phi_q \phi_p dz}_{=(\mathbf{M}_\sigma^{\text{SE}})_{pq}} \underbrace{\int_{\Omega_h} \sigma^{(t)} \vec{w}_e^{(t)} \cdot \vec{w}_d^{(t)} dx dy}_{=(\mathbf{M}_\sigma^{\text{FE,t}})_{de}} \quad (5.26a)$$

$$+ \underbrace{\int_I \sigma^{(\ell)} \phi_w \phi_v dz}_{=(\mathbf{M}_\sigma^{\text{SE}})_{vw}} \underbrace{\int_{\Omega_h} \sigma^{(t)} N_j N_i dx dy}_{=(\mathbf{M}_\sigma^{\text{FE,\ell}})_{ij}}. \quad (5.26b)$$

Again, the integrals can be identified with 1D SE and 2D FE matrices, respectively. In this way, (5.26a) yields the Q3D transversal edge-mass matrix

$$\mathbf{M}_\sigma^{\text{Q3D,t}} = \mathbf{M}_\sigma^{\text{SE}} \otimes \mathbf{M}_\sigma^{\text{FE,t}}, \quad (5.27)$$

and (5.26b) the Q3D longitudinal edge-mass matrix

$$\mathbf{M}_\sigma^{\text{Q3D,\ell}} = \mathbf{M}_\sigma^{\text{SE}} \otimes \mathbf{M}_\sigma^{\text{FE,\ell}}. \quad (5.28)$$

Together, they form the Q3D edge-mass matrix

$$\mathbf{M}_\sigma^{\text{Q3D,e}} = \begin{bmatrix} \mathbf{M}_\sigma^{\text{Q3D,t}} & \mathbf{0} \\ \mathbf{0} & \mathbf{M}_\sigma^{\text{Q3D,\ell}} \end{bmatrix}. \quad (5.29)$$

The sparsity pattern of the Q3D edge mass matrix is shown in Fig. 5.4b for an exemplary Q3D discretization, where the diagonal block matrix structure containing the transversal and longitudinal edge mass matrices is clearly distinguishable. From the Coulomb gauge condition, the terms

$$\left(\mathbf{C}_1^{\text{Q3D}}\right)_{deijpqvw} = \int_{V_h} \begin{bmatrix} w_{d,x}^{(t)} \phi_p \\ w_{d,y}^{(t)} \phi_p \\ N_i \phi_v \end{bmatrix} \cdot \nabla (N_j \phi_q) \, dV, \quad (5.30a)$$

$$\left(\tilde{\mathbf{C}}_1^{\text{Q3D}}\right)_{deijpqvw} = \int_{V_h} \nabla (N_i \phi_p) \cdot \begin{bmatrix} w_{e,x}^{(t)} \phi_q \\ w_{e,y}^{(t)} \phi_q \\ N_j \phi_w \end{bmatrix} \, dV \quad (5.30b)$$

arise. The term (5.30a) is decomposed into

$$\left(\mathbf{C}_1^{\text{Q3D}}\right)_{deijpqvw} = \underbrace{\int_I \phi_p \phi_q \, dz}_{=(\mathbf{M}_1^{\text{SE}})_{pq}} \underbrace{\int_{\Omega_h} \vec{w}_d^{(t)} \cdot \nabla_{xy} N_j \, dx dy}_{=(\mathbf{C}_1^{\text{FE,t}})_{dj}^\top} \quad (5.31a)$$

$$+ \underbrace{\int_I \partial_z \phi_q \phi_p \, dz}_{=(\mathbf{D}_1^{\text{SE}})_{pq}} \underbrace{\int_{\Omega_h} N_j N_i \, dx dy}_{=(\mathbf{M}_1^{\text{FE,n}})_{ij}} \quad (5.31b)$$

and (5.30b) is expressed in the same way but with flipped indices. Finally, (5.30a) and (5.30b) are written as

$$\mathbf{C}_1^{\text{Q3D}} = \left[\mathbf{M}_1^{\text{SE}} \otimes (\mathbf{C}_1^{\text{FE,t}})^\top \quad \mathbf{D}_1^{\text{SE}} \otimes \mathbf{M}_1^{\text{FE,n}} \right], \quad (5.32)$$

$$\tilde{\mathbf{C}}_1^{\text{Q3D}} = (\mathbf{C}_1^{\text{Q3D}})^\top. \quad (5.33)$$

From the mixed voltage distribution terms, the matrices

$$\left(\mathbf{X}_\sigma^{\text{Q3D}}\right)_{diptv} = \int_{V_h} \sigma \frac{T_t}{\ell_t} \vec{e}_z \cdot \begin{bmatrix} w_{d,x}^{(t)} \phi_p \\ w_{d,y}^{(t)} \phi_p \\ N_i \phi_v \end{bmatrix} \, dV, \quad (5.34a)$$

$$\left(\tilde{\mathbf{X}}_\sigma^{\text{Q3D}}\right)_{ejqsw} = \int_{V_h} \sigma \begin{bmatrix} w_{e,x}^{(t)} \phi_q \\ w_{e,y}^{(t)} \phi_q \\ N_j \phi_w \end{bmatrix} \cdot \frac{T_s}{\ell_s} \vec{e}_z \, dV \quad (5.34b)$$

arise. Obviously, both terms have only a longitudinal component, since the voltage distribution

function $\vec{\xi}$ purely points in z -direction. The term (5.34a) is written out as

$$(\mathbf{X}_\sigma^{\text{Q3D}})_{itv} = \underbrace{\int_I \sigma^{(\ell)} \phi_v dz}_{=(\mathbf{f}_\sigma^{\text{SE}})_v} \underbrace{\int_{\Omega_h} \sigma^{(t)} \ell_t^{-1} T_t N_i dx dy}_{=(\mathbf{X}_\sigma^{\text{FE}})_{it}}. \quad (5.35)$$

Again, (5.34b) is expressed in the same way but with flipped indices. Then, (5.34a) and (5.34b) are expressed as

$$\mathbf{X}_\sigma^{\text{Q3D}} = \mathbf{f}_\sigma^{\text{SE}} \otimes \mathbf{X}_\sigma^{\text{FE}}, \quad (5.36)$$

$$\tilde{\mathbf{X}}_\sigma^{\text{Q3D}} = (\mathbf{X}_\sigma^{\text{Q3D}})^\top, \quad (5.37)$$

where

$$(\mathbf{f}_\sigma^{\text{SE}})_p = \int_I \sigma^{(\ell)} \phi_p dz \quad (5.38)$$

is the spectral load vector with the electrical conductivity as right-hand side function. In the end, the semi-discrete magnetic Q3D system of equations is obtained,

$$\begin{bmatrix} \mathbf{K}_\nu^{\text{Q3D,e}} + \left(\mathbf{K}_{\nu\tau}^{\text{Q3D,e}} + \mathbf{M}_\sigma^{\text{Q3D,e}} \right) \frac{d}{dt} & -\mathbf{X}_\sigma^{\text{Q3D}} & -\left(\mathbf{C}_1^{\text{Q3D}} \right)^\top \\ -\left(\mathbf{X}_\sigma^{\text{Q3D}} \right)^\top \frac{d}{dt} & \mathbf{G}_\sigma & \mathbf{0} \\ -\mathbf{C}_1^{\text{Q3D}} & \mathbf{0} & \mathbf{0} \end{bmatrix} \begin{bmatrix} \hat{\mathbf{a}} \\ \mathbf{u} \\ \zeta \end{bmatrix} = \begin{bmatrix} \mathbf{0} \\ \mathbf{i} \\ \mathbf{0} \end{bmatrix}, \quad (5.39)$$

where $\hat{\mathbf{a}}$ unites the Q3D coefficients of the transversal and longitudinal component of the MVP,

$$\hat{\mathbf{a}} = \begin{bmatrix} \hat{\mathbf{a}}^{(t)} \\ \hat{\mathbf{a}}^{(\ell)} \end{bmatrix}, \quad (5.40)$$

which has a total of

$$N^{\text{Q3D,MVP}} = (N_e + N_n)(NN_{\text{SE}} + 1) \quad (5.41)$$

entries. The Lagrange multiplier coefficient vector ζ has $N^{\text{Q3D,n}}$ entries, and the voltage drop vector \mathbf{u} has \mathcal{W} entries. Overall, the total number of DoF of the gauged system (5.39) results to

$$N^{\text{Q3D,e}} = (N_e + 2N_n)(NN_{\text{SE}} + 1) + \mathcal{W}. \quad (5.42)$$

Finally, one has to discretize the temporal derivative in (5.39) to obtain a fully discrete system of equations that can be solved numerically as described in Sec. 4.2. Furthermore, one can expand (5.39) for a field-circuit coupling as discussed in Sec. 4.5.

Given a FE DoF (node or edge) index $i \in 1, \dots, N_{\text{FE,DoF}}$, a SE index $k \in 1, \dots, N_{\text{SE}}$ and a mode $q \in 1, \dots, N + 1$, the corresponding global Q3D index is obtained by the formula

$$n(i, k, q) = i + [(q - 1) + N(k - 1)] N_{\text{FE,DoF}}, \quad (5.43)$$

where $N_{\text{FE,DoF}}$ stands for the total number of FE DoFs, i.e. N_n in the nodal case and N_e in the edge case.

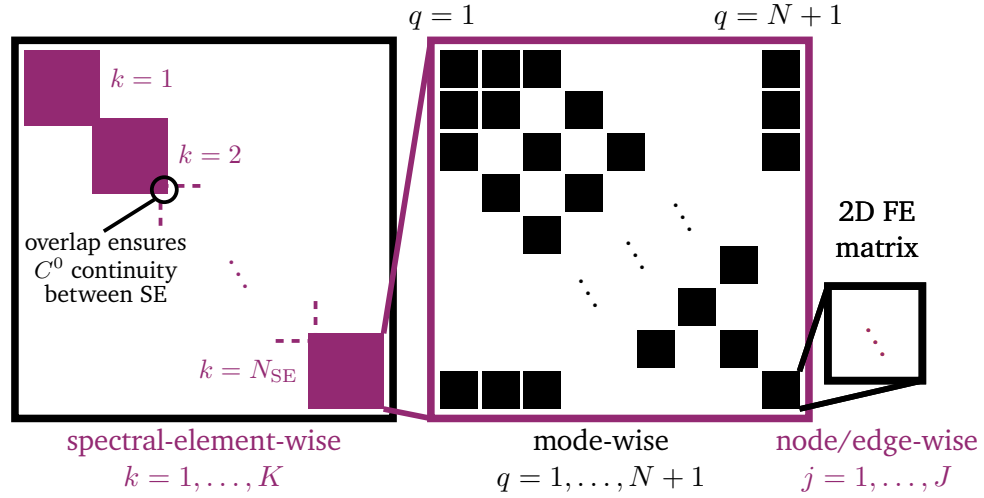


Figure 5.2.: Kronecker tensor product structure of the Q3D matrices: On the top level, there are block matrices for each SE which consist of a mode-wise block matrix pattern. These lowest level block matrices are the 2D FE matrices with node-wise and edge-wise entries for the nodal and edge matrices, respectively. Figure adapted from [DCD20].

5.2. Idiosyncrasies of the Quasi-3D Method

The Q3D hybrid basis functions are composed of the products of FE and SE basis functions. As a result, the Q3D discrete quantities are constructed by performing Kronecker tensor products of 2D FE and 1D SE quantities. This leads to special properties for the Q3D systems of equations and the Q3D method in general, which are discussed in the following.

Quasi-3D Matrix Structures

The Kronecker tensor product of SE and FE matrices creates a special pattern for the Q3D matrix as shown in Fig. 5.2: On the top level, a diagonal overlapping block matrix structure is visible. Each of these blocks is a spectral method matrix with a mode-wise block matrix pattern. These, in turn, are the 2D FE matrices, whose entries are either node- or edge-wise depending on the chosen shape functions.

Figure 5.3 shows the sparsity pattern for both the Q3D nodal stiffness matrix (divgrad matrix) $\mathbf{K}_\lambda^{\text{Q3D},n}$ and the Q3D nodal mass matrix $\mathbf{M}_{C_V}^{\text{Q3D},n}$ for an exemplary Q3D discretization with $N_n = 29$, $N_e = 68$, $N_{\text{SE}} = 2$ and $N = 6$. Since they both involve the spectral Lobatto mass matrix (4.79) with its tridiagonal structure, both Q3D nodal matrices share the same sparsity pattern. Here, one can clearly distinguish the two block matrices corresponding to the two SEs. Therein, the $N + 1 = 7$ modal block matrix structure is visible. In turn, each modal block matrix exhibits the structure of a nodal FE matrix.

Figure 5.4 shows the sparsity pattern for the ungauged Q3D edge stiffness matrix (curlcurl matrix) $\mathbf{K}_\nu^{\text{Q3D},e}$ and the ungauged Q3D edge mass matrix $\mathbf{M}_\sigma^{\text{Q3D},e}$ for the same Q3D configuration. On top of the SE block level, the Q3D edge matrices are partitioned in a transversal part (top left block) and a longitudinal part (bottom right block). In Fig. 5.4a, the additional transversal-longitudinal coupling terms $\mathbf{C}_\nu^{\text{Q3D},t\ell}$ and $\mathbf{C}_\nu^{\text{Q3D},\ell t}$ of the Q3D curlcurl matrix are visible as secondary rectangular matrix blocks.

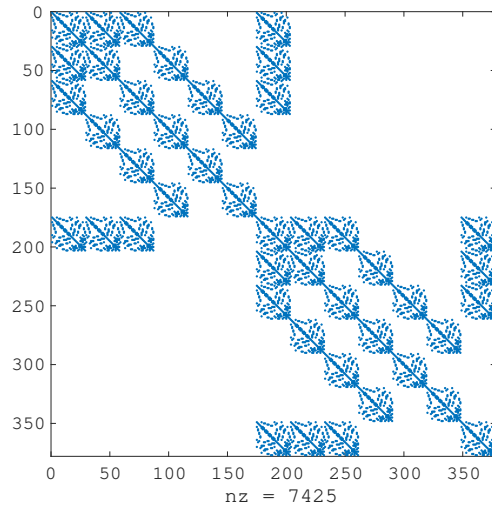
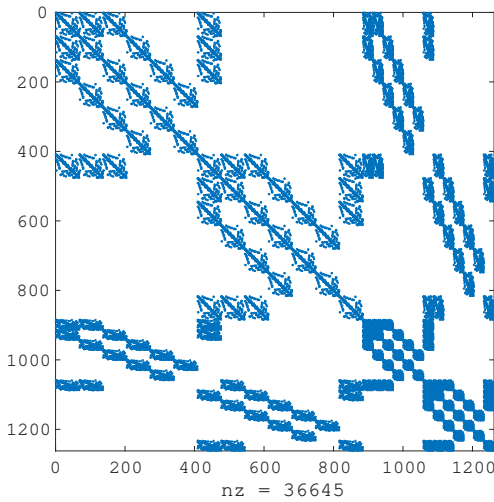
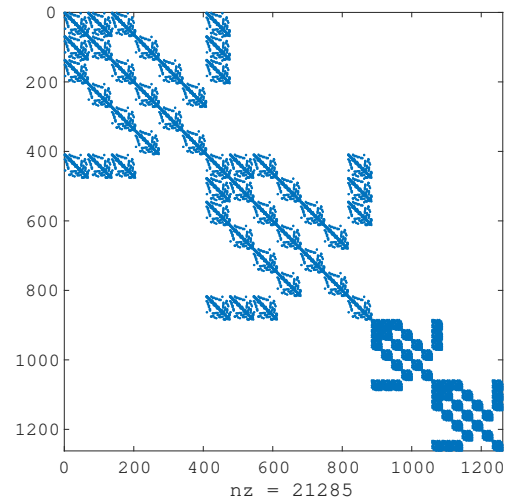


Figure 5.3.: Sparsity pattern for the Q3D nodal stiffness matrix (divgrad matrix) $\mathbf{K}_\lambda^{\text{Q3D},n}$ and Q3D nodal mass matrix $\mathbf{M}_{C_V}^{\text{Q3D},n}$ for an exemplary Q3D discretization with $N_n = 29$, $N_e = 68$, $N_{\text{SE}} = 2$ and $N = 6$, resulting into 7425 non-zero (nz) entries. The two block matrices corresponding to the two SEs are clearly distinguishable, as well as the $N + 1 = 7$ modal block matrix structure within.



(a) Q3D edge stiffness matrix $\mathbf{K}_\nu^{\text{Q3D},e}$.



(b) Q3D edge mass matrix matrix $\mathbf{M}_\sigma^{\text{Q3D},e}$.

Figure 5.4.: Sparsity pattern for the Q3D edge stiffness matrix (curlcurl matrix) (5.24) and Q3D edge mass matrix (5.29) for an exemplary Q3D discretization with $N_n = 29$, $N_e = 68$, $N_{\text{SE}} = 2$ and $N = 6$.

Impact of the Kronecker Tensor Product Order

It is possible to define the Kronecker tensor product in a reversed way, i.e. FE matrices \otimes SE matrices instead of SE matrices \otimes FE matrices. Then, on the top level of the Q3D matrix, a 2D FE structure would be visible with node- or edge-wise SE block matrices. Accordingly, the order of the Q3D coefficients in the solution vector changes and with that the global index formula (5.43). Numerical experiments show that the reversed product order does not lead to a different condition number or computational effort to solve the Q3D system. However, because sparse direct solvers pass through the matrix in certain directions, the Kronecker tensor product order may affect rounding-off errors in such solvers.

The order could have more significance for dedicated algebraic techniques, in which the Kronecker tensor products are not explicitly carried out. For example, in Runge-Kutta time integration [Boo+07] or in stochastic collocation [RV10] of PDEs, similar Kronecker product matrices arise. The resulting systems are then solved by multigrid solvers. In these applications, it is indeed computationally more reasonable to choose the reversed product order, i.e. with the FE matrix as first factor.

Either way, the Kronecker tensor product nature of the Q3D quantities leads to a very efficient assembly of the Q3D matrices, provided that the respective 2D FE and 1D SE assembly routines are well implemented.

Similarities and Differences to Finite Element Methods

Albeit not widely used, triangular prism elements are also known in the classical FEM [ZTT05]. For $N = 1$, the Q3D basis functions coincide with the FE ones using first-order triangular prism elements.

For $N > 1$, the translational Q3D method resembles a 3D anisotropic hp -FEM using triangular prism elements, for which first-order basis functions are utilized in the xy -plane, and higher-order basis functions are employed in z -direction. Similarly to such a hp -FEM, the Q3D method needs only a few large elements in z -direction, on which the solution is approximated with polynomial basis functions. However, the hp -FEM typically employs hierarchical basis functions based on normalized Legendre polynomial integrals [BS94]. This leads to a p -adaptive property, meaning that the discretization can be refined by just adding additional basis functions without changing the solution coefficients and the need for re-meshing. This is not true for the Q3D method, which would need a re-calculation of the LGL nodes upon increasing the polynomial order N , necessitating the re-computation of the solution coefficients. On the other hand, hierarchical functions are only approximately orthogonal [BS94], resulting into much less sparse matrices as the Q3D method with its exactly orthogonal polynomial basis functions (see Sec. 4.4).

Furthermore, in contrast to the hp -FEM, the Q3D basis functions lead to a tensor product character of the method. This property imposes some requirements on the model, e.g. the materials cannot be defined prism-element-wise, but as a product of a xy -dependent quantity and a z -dependent quantity as done for e.g. the thermal conductivity (5.5), and local refinements of the computational domain are not possible. Breaking these requirements leads to a partial or full loss of the tensor product character. However, this tensor product character can be exploited to speed up the assembly and solution of the Q3D systems of equations.

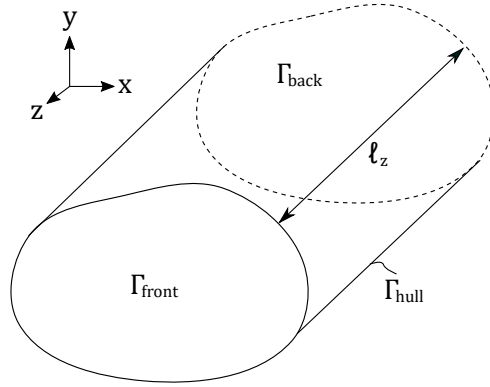


Figure 5.5.: Different types of boundaries in the Q3D model: Γ_{hull} relates to the boundary of the 2D FE computational domain, while Γ_{front} and Γ_{back} are related to the end points of the 1D SE interval.

5.3. Quasi-3D Boundary Conditions

As a combination of a 1D SEM and a 2D FEM, the Q3D method distinguishes three main types of general boundaries (see Fig. 5.5):

1. The boundary of the 2D FE mesh, i.e. the transversal cross-section, which represents the hull Γ_{hull} of the 3D geometry.
2. The back surface of the 3D geometry, Γ_{back} , which relates to one end point of the 1D SE interval, i.e. $z = 0$ in the image interval and $\hat{z} = -1$ in the reference interval.
3. The front surface of the 3D geometry, Γ_{front} , which relates to the other end point of the 1D SE interval, i.e. $z = \ell_z$ in the image interval and $\hat{z} = +1$ in the reference interval.

BCs on Γ_{back} and Γ_{front} involve only the boundary modes $q = 1$ and $q = N + 1$ of the Q3D discretization, while BCs on Γ_{hull} have to take also the inner modes $q = 2, \dots, N$ into account. In case of the edge shape functions, only the MVP components, which are tangential with respect to the respective boundary, are relevant for the BC treatment. Thus, on Γ_{back} and Γ_{front} , only the transversal MVP component is affected by BCs, while on Γ_{hull} , both the longitudinal and transversal MVP components play a role.

In the following, the relevant BCs for quench simulation are introduced and their incorporation into the Q3D model and the Q3D systems of equations is discussed.

Dirichlet BCs

A Dirichlet BC means that the solution u on a certain boundary Γ_{Dir} is known beforehand,

$$u(\vec{r}, t) = u_{\text{Dir}}(\vec{r}, t) \quad \text{at } \Gamma_{\text{Dir}}. \quad (5.44)$$

In the context of the thermal model, this represents an isothermal BC, i.e. a fixed temperature at Γ_{Dir} . For the magnetic model, a homogeneous Dirichlet BC, i.e. $u_{\text{Dir}}(\vec{r}, t) = 0$, represents an electric BC, i.e. the vanishing of the normal component of the magnetic field flux, $\vec{n} \cdot \vec{B} = 0$, which corresponds to $\vec{n} \times \vec{A} = 0$. An inhomogeneous Dirichlet BC is used to set the magnetic field flux on the boundary to a specified external magnetic field flux value, $\vec{B} = \vec{B}_{\text{ext}}$ at Γ_{Dir} ,

see Chapter 3. In terms of the MVP, the tangential component of \vec{A} is set, such that the desired \vec{B}_{ext} is obtained following $\vec{B} = \nabla \times \vec{A}$. As the discrete problem works with line-integrated MVP coefficients $\hat{a}_{eq}^{(t)}, \hat{a}_{jw}^{(\ell)} \in \mathbb{R}$, the scalar condition (5.44) can be also considered for Dirichlet BCs applying to the MVP. Then, u refers to the MVP coefficients, whose related component is tangential to the boundary Γ_{Dir} , i.e. $\hat{a}_{eq}^{(t)}$ for Γ_{back} and Γ_{front} , and $\hat{a}_{jw}^{(\ell)}$ for Γ_{hull} .

The precise incorporation of the Dirichlet BC depends on the boundary type and the nature of u_{Dir} . In the case of $\Gamma_{\text{Dir}} = \Gamma_{\text{back}}$ or $\Gamma_{\text{Dir}} = \Gamma_{\text{front}}$, only the first or last boundary modes of the corresponding nodes and edges play a role, respectively. Let $\mathcal{J}_{\text{back}}$ and $\mathcal{J}_{\text{front}}$ denote the index set of mesh DoFs (nodes or edges) contained in Γ_{back} and Γ_{front} , respectively, and $u_{jq}^{(k)}$ be the solution coefficient on the j -th mesh DoF for the q -th mode in the k -th SE. Then, the continuous conditions

$$u(\vec{r}, t) = u_{\text{back}}(\vec{r}, t) \quad \text{at } \Gamma_{\text{back}}, \quad (5.45a)$$

$$u(\vec{r}, t) = u_{\text{front}}(\vec{r}, t) \quad \text{at } \Gamma_{\text{front}} \quad (5.45b)$$

translate into the discrete conditions

$$u_{i,1}^{(1)}(t) = u_{i,\text{back}}(t), \quad i \in \mathcal{J}_{\text{back}}, \quad (5.46a)$$

$$u_{i,N+1}^{(N_{\text{SE}})}(t) = u_{i,\text{front}}(t), \quad i \in \mathcal{J}_{\text{front}}, \quad (5.46b)$$

with $u_{i,\text{back}}$ and $u_{i,\text{front}}$ being the Dirichlet data for the i -th mesh DoF at the back and front boundary, respectively. In practice, only the corresponding boundary modes have to be manipulated to incorporate Dirichlet BCs at Γ_{back} and Γ_{front} , which is due to the nodal property of the modified Lobatto polynomials at the boundaries of the interval I , as already discussed in Sec. 4.4.

In the case of $\Gamma_{\text{Dir}} = \Gamma_{\text{hull}}$, all modes and SEs of the corresponding nodes and edges are affected by the Dirichlet BC, since the BC takes effect in the whole longitudinal dimension. Therefore, it does not suffice to only manipulate boundary modes, especially if the Dirichlet data u_{hull} varies in z -direction. Then, the inner modes are generally non-zero, because they define the non-constant nature of the solution and, thus, they are needed to represent a u_{hull} with $\partial_z u_{\text{hull}} \neq 0$. If, however, $u_{\text{hull}} \equiv \text{constant}$, then the inner modes have to be set to zero to represent the function's constancy, while the boundary modes are simply set to u_{hull} .

Let $\mathcal{J}_{\text{hull}}$ denote the index set of mesh DoFs (nodes or edges) contained in Γ_{hull} . Then, the continuous condition

$$u(\vec{r}, t) = u_{\text{hull}}(\vec{r}, t) \quad \text{at } \Gamma_{\text{hull}} \quad (5.47)$$

translates into the discrete condition

$$u_{iq}^{(k)}(t) = \tilde{u}_{iq,\text{hull}}^{(k)}(t), \quad i \in \mathcal{J}_{\text{hull}}, \quad (5.48)$$

where $\tilde{u}_{iq,\text{hull}}^{(k)}$ are the coefficients of the modified Lobatto polynomial expansion of u_{hull} for the i -th mesh DoF, q -th mode and k -th SE. They are obtained by a forward transform (4.73) for each $i \in \mathcal{J}_{\text{hull}}$, and will display the aforementioned modal behavior.

Neumann BCs

Homogeneous Neumann BCs (3.29h) and (3.33c) are used in the magnetic and thermal model to represent magnetic and adiabatic BCs, respectively. They are natural BCs, meaning that they do not have to be imposed explicitly into the discrete systems of equations, as the homogeneous

Neumann boundary integral terms in the weak formulations (4.6) and (4.12) become zero by definition.

Robin BCs

A Robin BC (3.31c) emulates the effects of thermal convection at the boundary Γ_{con} . On this boundary, a heat exchange with the surrounding helium with temperature ϑ_{fluid} and heat transfer coefficient α takes place (see Sec. 3.3). The Robin BC is incorporated into the weak thermal formulation through the boundary integral term in (4.2), yielding

$$-\int_{\Gamma_{\text{con}}} \lambda \partial_n \vartheta \vartheta' \, dS = \int_{\Gamma_{\text{con}}} \alpha (\vartheta - \vartheta_{\text{fluid}}) \vartheta' \, dS. \quad (5.49)$$

The right-hand side can be split in two boundary integral terms,

$$R = \int_{\Gamma_{\text{con}}} \alpha \vartheta \vartheta' \, dS, \quad (5.50)$$

$$r = \int_{\Gamma_{\text{con}}} \alpha \vartheta_{\text{fluid}} \vartheta' \, dS. \quad (5.51)$$

After discretization with the Q3D approximation (5.1) and (5.2), a left-hand side matrix and a right-hand side vector arise,

$$(\mathbf{R}_\alpha^{\text{Q3D}})_{ijpq} = \underbrace{\int_I \alpha^{(\ell)} \phi_q \phi_p \, dz}_{=(\mathbf{M}_\alpha^{\text{SE}})_{pq}} \underbrace{\int_{\Gamma_{\text{con}}} \alpha^{(t)} N_j N_i \, ds(x, y)}_{=(\mathbf{R}_\alpha^{\text{FE}})_{ij}}, \quad (5.52)$$

$$(\mathbf{r}_\alpha^{\text{Q3D}})_{ip} = \underbrace{\int_I \alpha^{(\ell)} \phi_p \, dz}_{=(\mathbf{f}_\alpha^{\text{SE}})_p} \underbrace{\int_{\Gamma_{\text{con}}} \alpha^{(t)} \vartheta_{\text{fluid}} N_i \, ds(x, y)}_{=(\mathbf{r}_\alpha^{\text{FE}})_i}. \quad (5.53)$$

Note that the FE integral parts are line integrals. As for all the other discrete Q3D quantities, the Robin matrix (5.52) and the Robin vector (5.53) can be expressed as Kronecker tensor products of 1D SE and 2D FE matrices and vectors,

$$\mathbf{R}_\alpha^{\text{Q3D}} = \mathbf{M}_\alpha^{\text{SE}} \otimes \mathbf{R}_\alpha^{\text{FE}}, \quad (5.54)$$

$$\mathbf{r}_\alpha^{\text{Q3D}} = \mathbf{f}_\alpha^{\text{SE}} \otimes \mathbf{r}_\alpha^{\text{FE}}. \quad (5.55)$$

Finally, the Robin BCs are incorporated into the thermal model by inserting $\mathbf{R}_\alpha^{\text{Q3D}}$ and $\mathbf{r}_\alpha^{\text{Q3D}}$ into the Q3D thermal system of equations (5.12).

Floating BCs

The floating BCs (3.40) are used to thermally connect the half-turn ends with each other, see Sec. 3.5. To this end, macro elements \mathcal{M}_m with multi-index $m = (v, w)$ are introduced for each

pair of connected floating boundaries $\Gamma_m = \Gamma_v \cup \Gamma_w$, such that

$$\mathcal{M}_m = \bigcup_{T \in \Gamma_m} T. \quad (5.56)$$

Each macro element is associated with an unknown ϑ_m and a macro basis function [DBH03]

$$M_m(\vec{r}) = \sum_{i \in \mathcal{J}_m} N_i(x, y) \phi_{(m)}(z), \quad (5.57)$$

where the index sets \mathcal{J}_m collect the nodal indices contained in Γ_m . Furthermore,

$$\phi_{(m)}(z) = \begin{cases} \phi_1^{(1)}(z), & \Gamma_m \subset \Gamma_{\text{back}}, \\ \phi_{N+1}^{(N_{\text{SE}})}(z), & \Gamma_m \subset \Gamma_{\text{front}}, \end{cases} \quad (5.58)$$

is one of the outermost boundary modes of the spectral modified Lobatto discretization, depending whether the floating boundaries are located at the back or front of the model. Note that inner modes are not involved in the floating BCs. Then, the temperature is decomposed into a non-floating "free" component denoted by the superscript *, and a floating component denoted by superscript f, where several DoFs are collapsed by macro elements,

$$\begin{aligned} \vartheta(\vec{r}, t) \approx & \underbrace{\sum_{j \in \mathcal{J}^*} \sum_{q=1}^{N+1} \vartheta_{jq}^*(t) N_j(x, y) \phi_q^{(k)}(z)}_{\text{fully free part}} + \underbrace{\sum_{j' \in \mathcal{J}_m} \sum_{q'=2}^N \vartheta_{j'q'}^*(t) N_{j'}(x, y) \phi_{q'}^{(k)}(z)}_{\text{part of free inner modes}} \\ & + \underbrace{\sum_{m=1}^{N_f} \vartheta_m^f(t) M_m(\vec{r})}_{\text{floating part}} \end{aligned} \quad (5.59)$$

with N_f as number of floating boundary pairs and

$$\mathcal{J}^* = \{1, \dots, N_n\} \setminus \bigcup_{m=1}^{N_f} \mathcal{J}_m \quad (5.60)$$

being the index set of all free nodes, i.e. nodes that are not contained in any floating boundary. In the Q3D context, the free Q3D indices $\mathcal{J}_*^{\text{Q3D}}$ include not only all modes on all SE of the nodal indices \mathcal{J}^* , which are not involved in the floating boundaries anyway, but also the inner modes on all SE of the nodal indices \mathcal{J}_m of the floating boundaries, as the floating boundaries are only located at Γ_{back} ($z = 0$) and Γ_{front} ($z = \ell_z$), yielding

$$\mathcal{J}_*^{\text{Q3D}} = \mathcal{J}^* \times \{1, \dots, N+1\} \cup \bigcup_{m=1}^{N_f} \mathcal{J}_m \times \{2, \dots, N\}. \quad (5.61)$$

The m -th Q3D floating index set reads

$$\mathcal{J}_m^{\text{Q3D}} = \begin{cases} \mathcal{J}_m \times \{1\}, & \text{if } \Gamma_m \subset \Gamma_{\text{back}}, \\ \mathcal{J}_m \times \{N+1\}, & \text{if } \Gamma_m \subset \Gamma_{\text{front}}. \end{cases} \quad (5.62)$$

With this and with having the unconstrained system of equations $\mathbf{A}\boldsymbol{\vartheta} = \mathbf{q}$ at hand, the decomposition (5.59) leads to the constrained system of equations

$$\begin{bmatrix} \mathbf{A}_{**} & \mathbf{A}_{*f} \\ \mathbf{A}_{f*} & \mathbf{A}_{ff} \end{bmatrix} \begin{bmatrix} \boldsymbol{\vartheta}_* \\ \boldsymbol{\vartheta}_f \end{bmatrix} = \begin{bmatrix} \mathbf{q}_* \\ \mathbf{q}_f \end{bmatrix} \quad (5.63)$$

as known from standard methods [DBH03]. Here, for each imposed floating BC, the corresponding indices are summed up leading to a partial collapse of the original matrix and vector parts,

$$\mathbf{A}_{**} = (A_{ij})_{i,j \in \mathcal{J}_*^{\text{Q3D}}} \quad \text{as extraction of the free matrix part,} \quad (5.64a)$$

$$\mathbf{A}_{*f} = \left(\sum_{n \in \mathcal{J}_f^{\text{Q3D}}} A_{in} \right)_{\substack{i \in \mathcal{J}_*^{\text{Q3D}} \\ 1 \leq f \leq N_f}} \quad \text{as column-wise sum per floating BC,} \quad (5.64b)$$

$$\mathbf{A}_{f*} = \left(\sum_{m \in \mathcal{J}_f^{\text{Q3D}}} A_{mj} \right)_{\substack{1 \leq f \leq N_f \\ j \in \mathcal{J}_*^{\text{Q3D}}}} \quad \text{as row-wise sum per floating BC,} \quad (5.64c)$$

$$\mathbf{A}_{ff} = \left(\sum_{m \in \mathcal{J}_f^{\text{Q3D}}} \sum_{n \in \mathcal{J}_f^{\text{Q3D}}} A_{mn} \right)_{1 \leq f \leq N_f} \quad \text{as double sum per floating BC,} \quad (5.64d)$$

and analogously for the load vector,

$$\mathbf{q}_* = (q_i)_{i \in \mathcal{J}_*^{\text{Q3D}}} \quad \text{as extraction of the free vector part,} \quad (5.65a)$$

$$\mathbf{q}_f = \left(\sum_{m \in \mathcal{J}_f^{\text{Q3D}}} q_m \right)_{1 \leq f \leq N_f} \quad \text{as sum per floating BC.} \quad (5.65b)$$

Herein, $\mathbf{A}_{**} \in \mathbb{R}^{|\mathcal{J}_*^{\text{Q3D}}| \times |\mathcal{J}_*^{\text{Q3D}}|}$, $\mathbf{A}_{*f} \in \mathbb{R}^{|\mathcal{J}_*^{\text{Q3D}}| \times N_f}$, $\mathbf{A}_{f*} \in \mathbb{R}^{N_f \times |\mathcal{J}_*^{\text{Q3D}}|}$ and $\mathbf{A}_{ff} \in \mathbb{R}^{N_f \times N_f}$. The vectors $\boldsymbol{\vartheta}_* \in \mathbb{R}^{|\mathcal{J}_*^{\text{Q3D}}|}$ and $\boldsymbol{\vartheta}_f \in \mathbb{R}^{N_f}$ collect the solution coefficients of the free DoFs and the floating DoFs, respectively. After solving (5.63), the solution can be inflated to $\boldsymbol{\vartheta}$ by appropriately setting $\vartheta_j = (\vartheta_f)_m$ for $j \in \mathcal{J}_m^{\text{Q3D}} \forall m = 1, \dots, N_f$ and $\vartheta_j = (\vartheta_*)_i$ for $j \in \mathcal{J}_*^{\text{Q3D}} \forall i = 1, \dots, |\mathcal{J}_*^{\text{Q3D}}|$.

5.4. Implementation and Program Structure

For a proof of concept, the proposed Q3D method is implemented in an in-house object-oriented framework in MATLAB [MAT20]. The code is structured in the following modules:

- The **2D FEM** module involves the triangular 2D FE mesh class and the 2D FE assembly routines. The mesh object is constructed with the assistance of the open-source software Gmsh [GR09]. The 2D FE mesh object contains information about the mesh coordinates and topology, which is utilized by the 2D FE assembly routines.
- The **1D SEM** module consists of the SE shape function class. This includes functions for evaluating and constructing orthogonal polynomials as well as backward and forward trans-

forming the spectral coefficients. The SE shape function constructs a 1D SE discretization based on modified Lobatto polynomials from a given partition in z -direction and a prescribed maximal polynomial order N . On this discretization, the 1D SE assembly routines construct the 1D SE matrices and vectors. Furthermore, this module includes the database of precomputed reference tensors for the efficient assembly of the nonlinear SE matrices (see Sec. 4.4). The subsequent tensor contractions are performed utilizing the MATLAB Tensor Toolbox [BK07; BK+17].

- The **Q3D** module contains the Q3D assembly routines, which employ the respective discretizations and assembly routines of the 2D FEM and 1D SEM packages to construct the Q3D entities according to Sec. 5.1. Furthermore, this module provides functions for Q3D calculations, such as for constraining the Q3D system of equations as explained in Sec. 5.3, computing Q3D global indices following (5.43), and backward and forward transforming the Q3D solution.
- The **end winding** module consists of three sub-modules:
 - The **MNA** sub-module contains all routines for handling electrical circuits based on the MNA.
 - The **Q3D MNA coupling** sub-module combines Q3D and MNA entities to perform a field-circuit coupling. This is required for the magnetic coil end effects (see Sec. 4.5). To this end, a Q3D MNA coupler object is constructed, which delivers the coupled system of equations (4.93) and provides functionalities for updating and indexing it.
 - The **Q3D floating coupling** sub-module uses the Q3D floating BCs to take the thermal coil end effects into account (see Sec. 5.3). To this end, a Q3D floating coupler object is constructed, which constrains a given system of equations based on the provided winding scheme information.
- Additional code capabilities are collected in a **toolbox** module, e.g. post-processing and visualization functionalities as well as functions for coupling the MATLAB program with Python [VD09] in order to utilize more powerful solvers for systems of equations such as MUMPS [ADL00].
- The **material** module contains nonlinear material characteristics for the thermal conductivity and electric resistivity of copper, NbTi/Nb₃Sn and polyimide taken from [Rus10]. They are employed by the Q3D matrix assembly routines to construct nonlinear matrices.

These modules form the Q3D simulation code, which is utilized to execute a quench simulation study. Such a Q3D quench simulation study typically consists of seven building blocks:

1. **Model setup:** The superconducting coil model is set up. This includes the definition of physical parameters and concepts such as materials, boundary conditions, excitations and the coil winding scheme, as well as the definition of numerical aspects such as nonlinear iteration criteria and the time discretization.
2. **2D FE discretization:** The cross-section of the superconducting coil model is discretized using the open-source mesher Gmsh [GR09] and the 2D FEM module.
3. **1D SE discretization:** The longitudinal dimension of the superconducting coil model is discretized using the 1D SEM module.

-
4. **Q3D discretization:** The Q3D module combines the 2D FE and 1D SE discretizations are combined into a Q3D discretization.
 5. **End winding modeling:** Based on the winding scheme of the superconducting coil, the end winding module takes the coil end effects in the thermal and magnetic model into account.
 6. **Solving the magneto-thermal problem:** In this step, the magneto-thermal systems of equations are stated, constrained and solved. This leads to a outer transient loop consisting of as many iterations as the number of time steps, and an inner nonlinear iteration loop with a variable number of steps depending on the convergence criteria. In this nonlinear loop, the magneto-thermal problem is solved following the alternating nonlinear method [SJ17] as described in Sec. 4.2.
 7. **Post-processing & visualization:** The obtained solution is post-processed, and the quantities of interest are reported and visualized such as voltages, maximal temperatures, thermal and magnetic energies, temperature curves along the half-turns, temperature and magnetic flux density distributions in 3D space and over time, etc. Ideally, this leads to new insights for the considered quench scenario.

Figure 5.6 shows a scheme of this procedure. The arrows indicate the data flow between the building blocks.

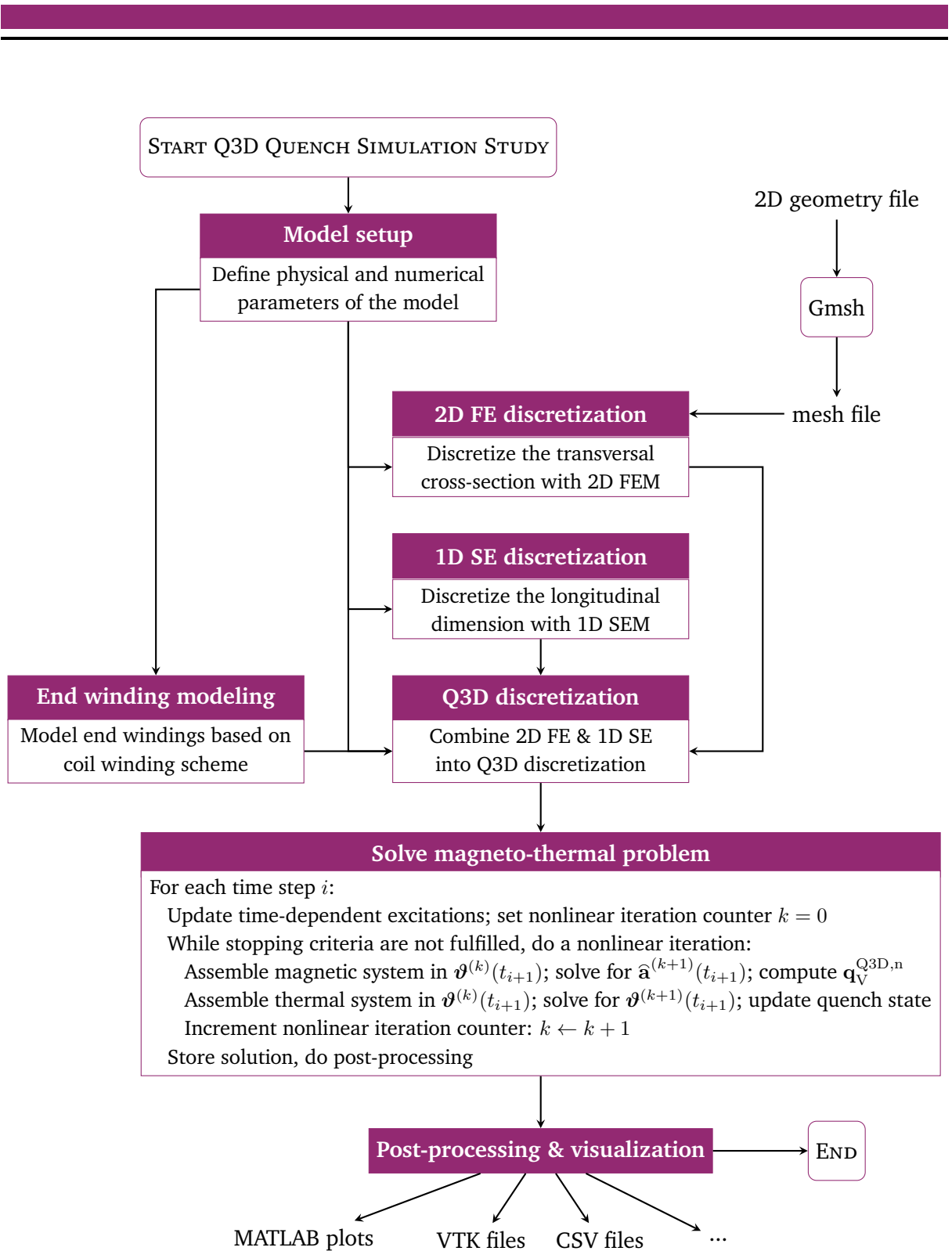


Figure 5.6.: Scheme of a Q3D quench simulation study. First, the physical and numerical parameters of the model are set up. These data are provided to the other steps of the study. Based on a user-given geometry, the open-source mesher Gmsh generates a 2D triangular mesh, which is utilized for the 2D FE discretization. The Q3D discretization step combines the 2D FE and 1D SE components. The Q3D systems of equations are then solved in a transient nonlinear iterative procedure. At the end, the results are post-processed and visualized.

6. Quasi-3D Quench Simulation Studies

Amy: "I've never seen results like this before."
Sheldon: "Yeah, we need to stop for magnets on the way home; this is going right on the fridge."

The Big Bang Theory

This chapter presents several Q3D quench simulation studies to verify the Q3D simulation approach and to compare it against conventional 3D FE simulation approaches in terms of computational efficiency and accuracy. After presenting the results of a convergence study, the Q3D method is used to simulate four different superconducting models.

6.1. Convergence Study

In order to numerically verify the Q3D method, convergence studies are carried out. To this end, the magnetostatic PDE

$$\nabla \times \nabla \times \vec{A}(\vec{r}) = \vec{J}(\vec{r}) \quad (6.1)$$

with $\nu \equiv 1$ in a cubic 3D domain $\Omega = [-1, 1]^3$ is considered, for which a manufactured solution

$$\vec{A}(\vec{r}) = \sin(\pi z)\vec{e}_x + \sin(\pi x)\sin(\pi y)\vec{e}_z \quad (6.2)$$

is constructed. From (6.2), it follows the magnetic flux density

$$\vec{B}(\vec{r}) = \nabla \times \vec{A}(\vec{r}) = \pi \sin(\pi x) \cos(\pi y)\vec{e}_x + \pi (\cos(\pi z) - \cos(\pi x) \sin(\pi y))\vec{e}_y, \quad (6.3)$$

the source current density

$$\vec{J}(\vec{r}) = \nabla \times \nabla \times \vec{A} = \pi^2 \sin(\pi z)\vec{e}_x + 2\pi^2 \sin(\pi x)\sin(\pi y)\vec{e}_z \quad (6.4)$$

the magnetic energy

$$W_{\text{mag}} = 4\pi^2 \quad (6.5)$$

and appropriate BCs. The problem is repeatedly solved using different combinations of characteristic mesh lengths h and maximal polynomial orders p . The computed magnetic energy $W_{\text{mag,num}}(h, p)$ is compared with the analytical magnetic energy (6.5). The relative error

$$\epsilon_{\text{rel}}(h, p) = \frac{|W_{\text{mag}} - W_{\text{mag,num}}(h, p)|}{W_{\text{mag}}} \quad (6.6)$$

is calculated and plotted over h in Fig. 6.1 and p in Fig. 6.2.

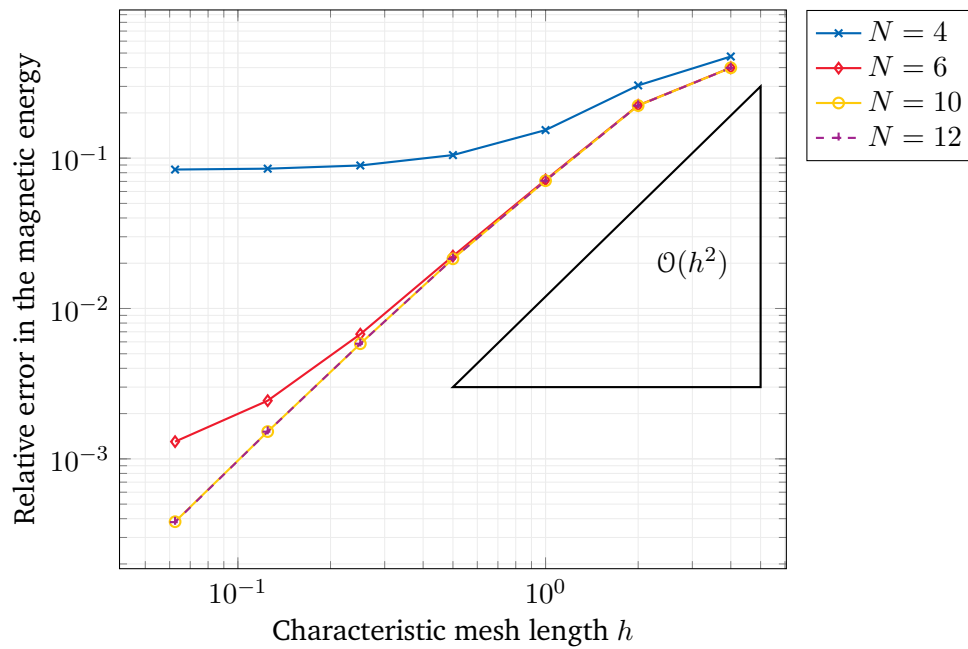


Figure 6.1.: Convergence behavior of the Q3D method depending on the characteristic mesh length h for fixed maximal polynomial orders N .

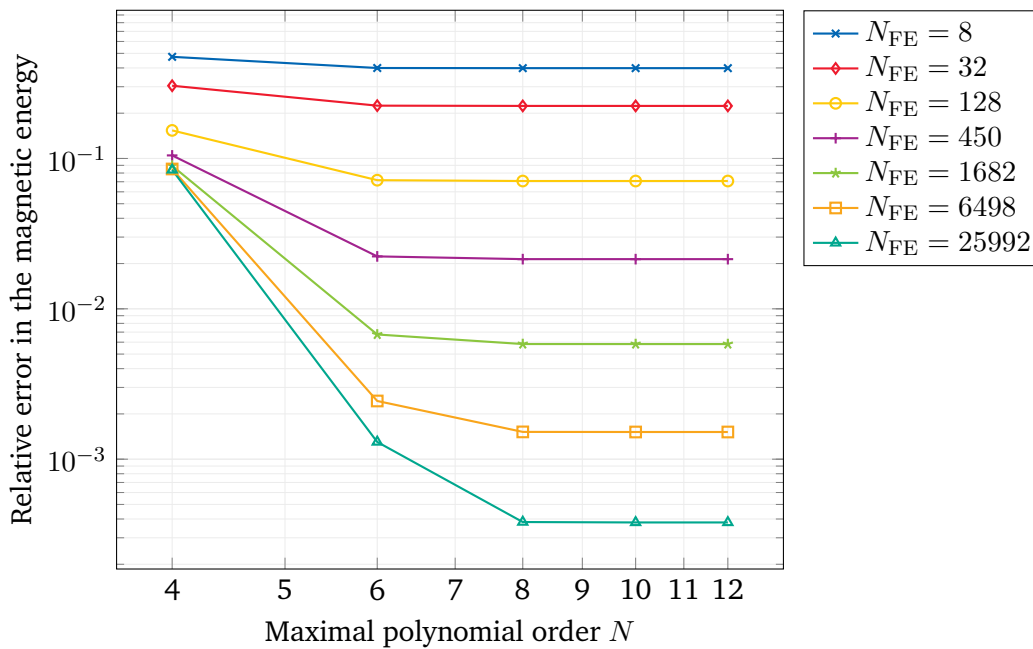


Figure 6.2.: Convergence behavior of the Q3D method depending on the maximal polynomial order N for fixed transversal meshes with N_{FE} number of FEs.

Figure 6.1 shows a quadratic convergence of the magnetic energy, which is the expected behavior for the chosen FE discretization [BS08]. For low N , the convergence stagnates for fine meshes, because the errors made in the spectral discretization outweigh the improvements achieved in the mesh refinement in the cross-section. In this case, only a p -refinement can lead to better results.

In Fig. 6.2, an exponential convergence behavior is observed as expected for spectral methods [STW11]. The coarser the mesh, the earlier the convergence begins to stagnate. Again, the reason is that the errors made in the cross-sectional FE discretization outweigh the improvements achieved in the p -refinement. The effect seems more pronounced than in Fig. 6.1, since the SEM converges much faster than the FEM. In conclusion, one can derive the following rules of thumb for the Q3D setting:

1. It does not make sense to choose a very high N as the accuracy of the solution is more influenced by the FE discretization. Experience shows that $N = 6, \dots, 8$ is an appropriate choice most of the times.
2. To improve results, one should rather refine the FE mesh instead of increasing the polynomial order of the SEM.

The results of the convergence study verify the correctness of the magnetic Q3D method. The thermal Q3D method was successfully verified in the same manner.

6.2. Thermal Simulation of Rutherford Cables

This simulation study represents a first test of the nodal Q3D method, which is subsequently compared to a conventional 3D FE simulation. The findings of this simulation study have been published in [DCD20].

Model and Scenario

A thermal problem consisting of a stack of three Rutherford cables is considered as shown in Fig. 2.4c. The cable cross-sections are homogenized following the homogenization approach presented in Sec. 3.1, while the glass fibre insulation layers are explicitly modeled. A heat excitation caused by a quench located in the left cable at $z_q = \frac{1}{3}\ell_z$ is mimicked by a prescribed constant Gaussian heat loss density

$$q_V(\vec{r}) = \hat{q} \exp\left(-\frac{(z - z_q)^2}{\sigma_q^2}\right) \chi_q(x, y), \quad (6.7)$$

where \hat{q} is the excitation's amplitude, σ_q is the standard deviation of the Gaussian function, and χ_q is a characteristic function

$$\chi_q(x, y) = \begin{cases} 1, & (x, y) \in V_q, \\ 0, & (x, y) \notin V_q, \end{cases} \quad (6.8)$$

which is only non-zero in the quenching cable volume V_q . Linear material properties are assumed, and homogeneous Neumann BCs are applied at the hull of the geometry, i.e. the cable stack is perfectly insulated.

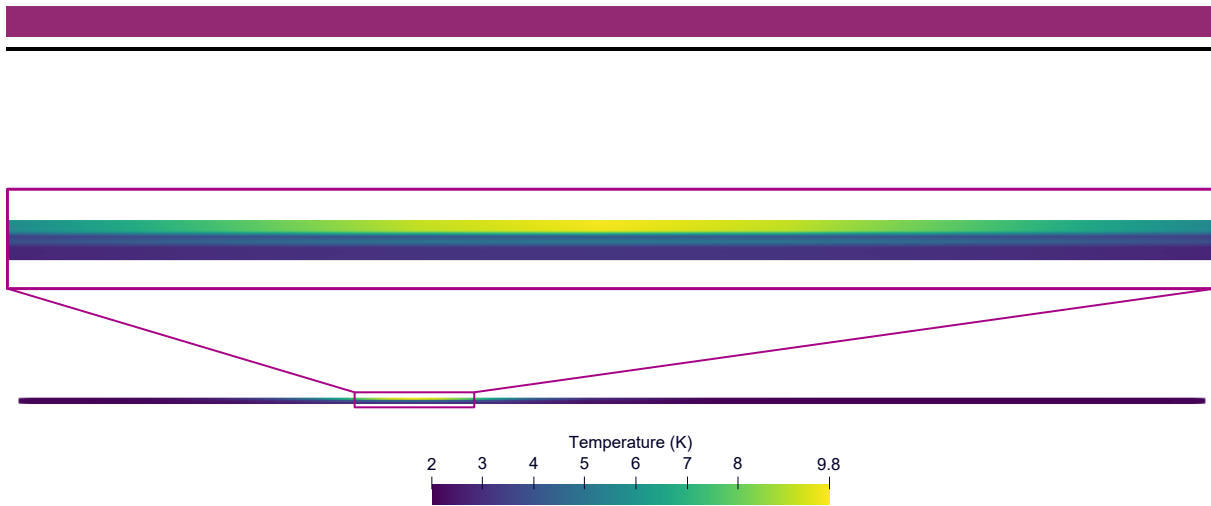


Figure 6.3.: Temperature distribution in the whole Rutherford cable model presented in Sec. 6.2 after 10 ms in the xz -plane (bottom), and a magnified view of the hot-spot region (top). The individual Rutherford cables are clearly distinguishable through the steep temperature drops at the insulation layers.

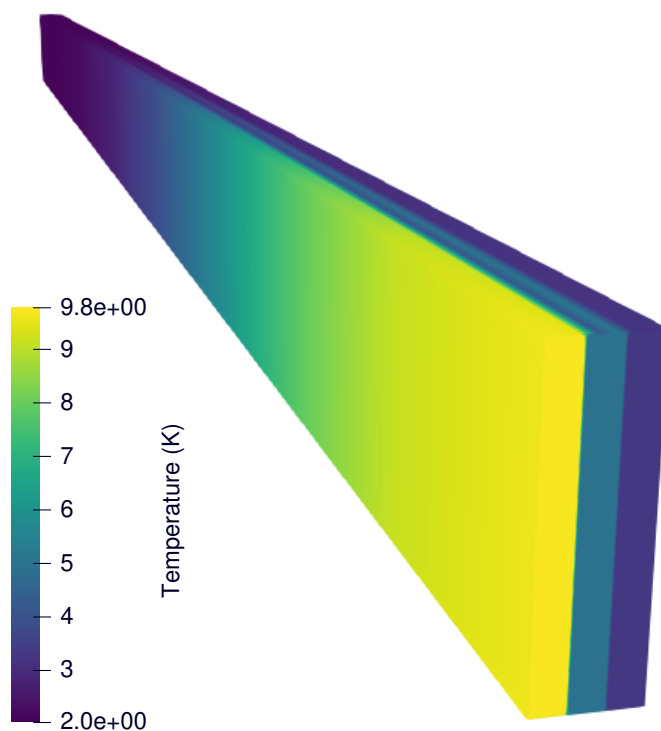


Figure 6.4.: Temperature distribution in the Rutherford cable stack model presented in Sec. 6.2 after 10 ms. The geometry is clipped at the hot-spot level $z = z_q$. Notice how the temperature sharply drops between the Rutherford cables due to the insulation layers, but smoothly diffuses into longitudinal direction, making the individual Rutherford cables clearly distinguishable [DCD20].

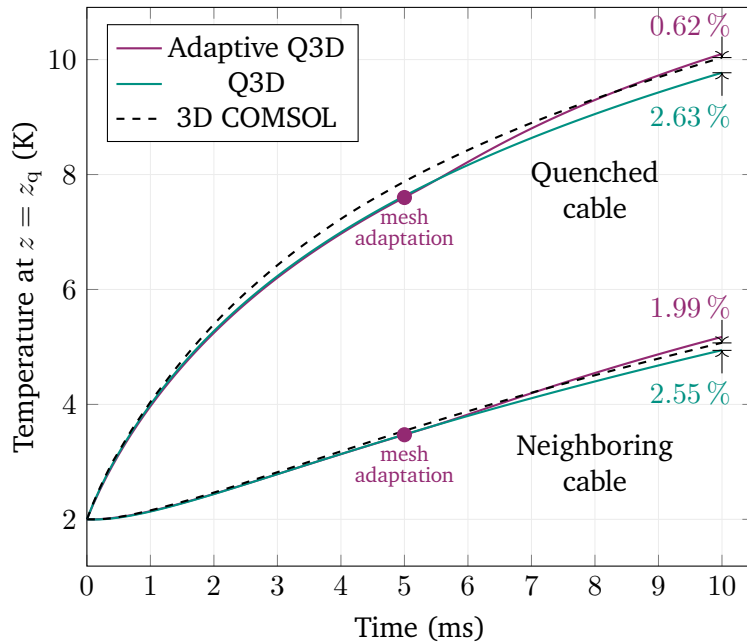


Figure 6.5.: Temperature curves over time at $z = z_q$ for the quenched cable and its neighboring cable. The green curve shows the Q3D solution without making a spectral mesh adaptation, while the purple curve shows the Q3D solution after adapting the spectral mesh after half-time of the simulation (indicated by a purple dot). The COMSOL reference solution is depicted as black dashed line. Figure adapted from [DCD20].

Simulation Results and Verification

Figure 6.4 shows the temperature distribution in the xy -plane at $z = z_q$ and at the end of the simulation time $t_{\text{end}} = 10$ ms. Due to the very good insulating property of the glass fibre, the heat exchange is much faster in longitudinal than in transversal direction. As a result, there are steep temperature drops from one cable cross-section to another. At the same time, the high thermal conductivity of the cables leads to a homogeneous temperature distribution in the cross-section, while the temperature smoothly varies in longitudinal direction.

Figure 6.5 shows the temperature development over time at the hot-spot point at $z = z_q$ for the quenched (left) cable and its neighboring (central) cable. The Q3D solutions (green) align very well with the reference solution (black) computed by a 3D FEM in COMSOL [COM], leading to relative differences below 3% at the end of the simulation time.

Nonetheless, it is observed that the Q3D solution moves further and further away from the reference solution over time. For this behavior, the fixed spectral discretization of the longitudinal dimension is to blame. As soon as the steep temperature fronts of the quench move to a SE interface, the orthogonal polynomials are no longer able to accurately resolve the temperature distribution (see Fig. 6.6): While the temperature curve at $t = 1$ ms (black) is resolved well by the black SE discretization, the temperature curve at $t = 4$ ms (purple) is especially problematic in the two outermost SEs, which would then require a high N to accurately resolve the curves. Hence, an adaptation of the spectral mesh is necessary, e.g. by moving the SE interfaces such that each half of the temperature "bell" is fully embedded into one SE, as shown in green in Fig. 6.6.

Indeed, by manually adapting the spectral mesh at $t = \frac{1}{2}t_{\text{end}}$, the results of the Q3D method

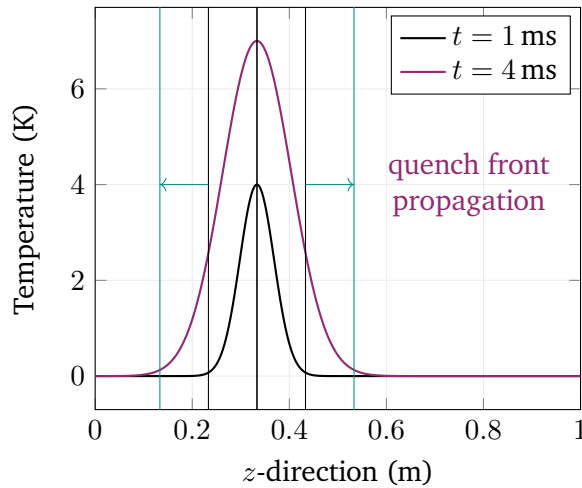


Figure 6.6.: Temperature distribution in the quenched cable in z -direction for two different points in time. The vertical lines indicate the SE interfaces and their required adaptation (green) to the moving quench fronts [DCD20].

are slightly improved as shown in purple in Fig. 6.5, leading to relative differences below 2%. The results could be further improved by implementing an adaptive Q3D mesh strategy, which automatically adapts the mesh when needed. Such strategies are already known in the area of SEMs [Mav92], and one has been successfully applied for a Q3D method using spectral wavelets in longitudinal direction [BDD21].

Performance Comparison to a 3D FE Simulation

To compare the spatial accuracy of the Q3D method with a 3D tetrahedral FE method, steady-state simulations are carried out to exclude time stepping errors. Different refinements of the Q3D and 3D FE method are compared to a fine 3D FE simulation in COMSOL. To accurately compare the two methods, the number of 2D FEs in the transversal cross-section is counted for the Q3D discretization, while for the 3D FE discretization, the average number of triangular cut surfaces in a cross-sectional slice is considered. The relative errors in the hot-spot temperature with respect to the reference simulation are shown in Fig. 6.7, where the numbers below the markers indicate the number of cross-sectional elements. Clearly, the Q3D method yields accurate results with less computational effort than the 3D simulation, e.g. for a cross-sectional resolution with 65 triangles, the 3D FEM requires a system matrix of size 21898×21898 , while the Q3D method achieves a similar error with a 98% smaller system matrix of size 2405×2405 , see the horizontal comparison in Fig. 6.7. On the other hand, if one would engage the computational resources for a system matrix of a size of approx. $10^4 \times 10^4$, one could achieve a much higher cross-sectional resolution with 915 FEs and more accurate simulation results using the Q3D method, see the vertical comparison in Fig. 6.7.

For this model, a length of $\ell_z = 1$ m has been chosen to be able to run a 3D FE simulation with reasonable computational costs. Note that real superconducting accelerator magnets can be over 10 m long. Therefore, much more pronounced gains in computational efficiency are expected from the Q3D method.

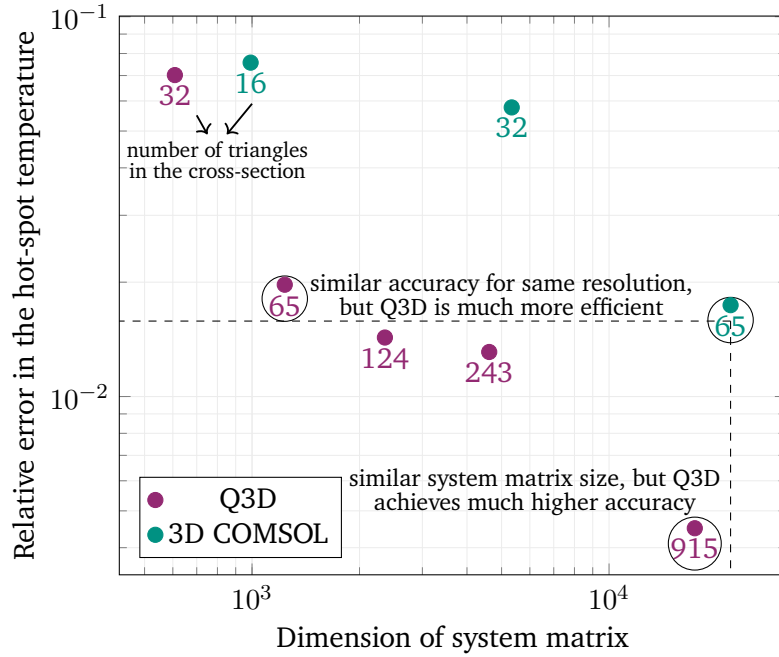


Figure 6.7.: The dimension of the Q3D (purple) and 3D FE (green) system matrices are plotted against the relative error in the hot-spot temperature w.r.t. a fine reference solution computed by COMSOL. The numbers below the marks denote the number of triangular elements resolving the transversal cross-section (Q3D) and the average number of triangular elements in a xy -slice (3D FE). The reference solution itself is resolved with 252 cross-sectional elements on average. The dashed lines mark the same level of accuracy (horizontally) and of computational efficiency (vertically), respectively. Figure adapted from [DCD20].

6.3. Magnetic Simulation of a Superconducting Cable

This simulation study checks if the Q3D method is able to portray the IFCC effects in superconducting cables, which have been discussed in Chapter 2 and mathematically described in Sec. 3.2. The findings of this simulation study are published in [DD21].

Model and Scenario

A cable segment with four round superconducting multi-filamentary wires is considered as shown in Fig. 6.8. The wires are assumed to be untwisted, such that the model can be viewed as a Q3D problem. The wire segment $\Omega_Q \cap K_Q$ is treated as quenched, i.e. normalconducting, all other wire segments as superconducting. This is modeled via the IFCC time constant as

$$\tau(\vec{r}) = \begin{cases} \tau_{SC}, & \vec{r} \in \Omega_{SC} \cap (K_{SC} \cup K_Q) \text{ or } \Omega_Q \cap K_{SC}, \\ 0, & \vec{r} \in \Omega_Q \cap K_Q \text{ or } \Omega_0 \cap (K_{SC} \cup K_Q), \end{cases} \quad (6.9)$$

with a constant $\tau_{SC} > 0$. An external harmonically time-varying magnetic flux density

$$\vec{B}_{\text{ext}}(\vec{r}, t) = -\hat{B} \sin(\omega t) \vec{e}_y \quad (6.10)$$

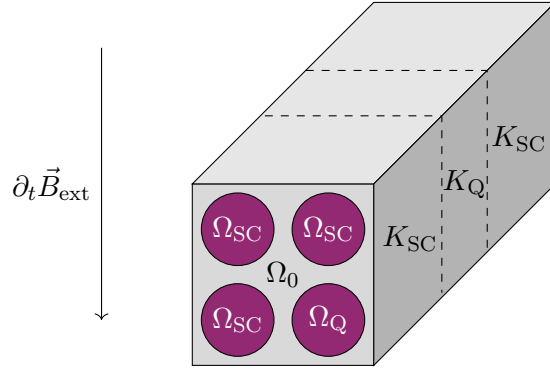


Figure 6.8.: Geometry of the superconducting cable model for the magnetic simulation study discussed in Sec. 6.3. Four multi-filamentary wires (highlighted in purple) are embedded in a non-conducting medium (gray). The wire segment $\Omega_Q \cap K_Q$ is treated as quenched (normalconducting), all other wire segments as superconducting. An external time-varying magnetic flux density \vec{B}_{ext} is applied on the model as indicated by the arrow. Figure adapted from [DD21].

is applied at the hull of the Q3D model. Here, \hat{B} is the magnetic flux density amplitude and ω is the angular frequency of the field excitation in rad/s. The model is simulated for a full excitation time period $2\pi\omega^{-1}$. As only the magnetic effects of the IFCC are of interest for this scenario, a quench development is not considered, meaning that the region $\Omega_Q \cap K_Q$ does not change in size during the simulation time.

Simulation Results and Verification

The magnetic flux density magnitude is shown in Fig. 6.9 and Fig. 6.10 at the excitation's peak time. Herein, Fig. 6.9 shows a volumetric view of the model, while for Fig. 6.10, the magnetic flux density magnitude is visualized on four slices, allowing for an inside view. As discussed in Chapter 2, superconducting regions completely expel the magnetic field due to the diamagnetic property of superconductors. Because of this, the positions of the four superconducting multi-filamentary wires are clearly visible through the zero magnetic flux density (dark blue color, i.e. $|\vec{B}| = 0$ T). For the same reason, one recognizes the quenched (normalconducting) segment part, which is penetrated by the magnetic flux density (light blue color, i.e. $|\vec{B}| > 0$ T). Therefore, these results phenomenologically validate the magnetic model introduced in Sec. 3.2.

The Q3D magnetic simulation is verified against a 3D simulation carried out in GetDP [Dul+98] by comparing the obtained magnetic energies over time. Figure 6.11a shows an excellent agreement w.r.t. the energies. The relative difference over time is shown in Fig. 6.11b, which is approximately in the order of 10^{-2} . In the time range, in which the energy approaches zero, rounding errors increase the error locally.

For the 3D simulation, the full 3D geometry was discretized with 480,164 tetrahedra resulting into 614,062 mesh edges, which is also the number of DoFs (excluding the DoFs arising from the gauging procedure). For the Q3D model, a transversal FE mesh with $N_{\text{FE}} = 2132$ triangles was chosen, leading to $N_n = 1125$ mesh nodes and $N_e = 3256$ mesh edges. The longitudinal direction was discretized with $N_{\text{SE}} = 3$ SE, while a maximal polynomial order of $N = 6$ was considered. Altogether, the total number of Q3D DoFs results into 83,239 (excluding the DoFs arising from the gauging procedure), which is only a fraction of the number of 3D DoFs. So, compared with

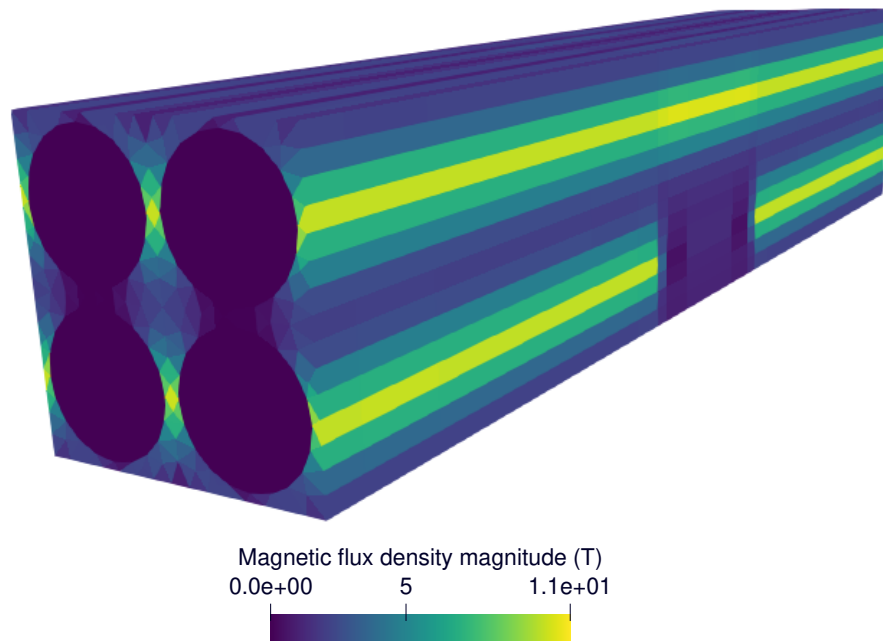


Figure 6.9.: Volumetric view of the magnetic flux density magnitude in the superconducting cable model presented in Sec. 6.3. The quenched segment part is visible due to the "disturbance" in the magnetic field flux density [DD21].

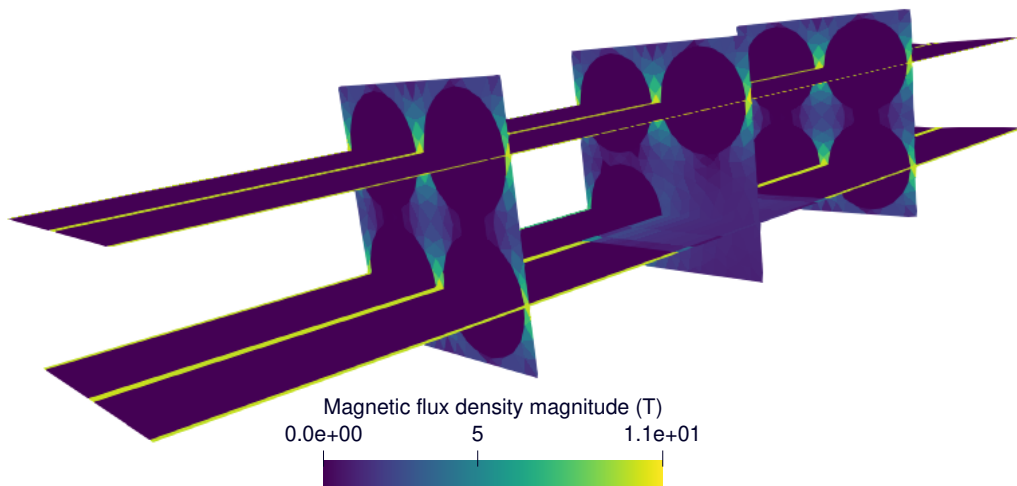


Figure 6.10.: Sliced view of the magnetic flux density magnitude in the superconducting cable model presented in Sec. 6.3. The quench segment part is penetrated by the magnetic field, while the superconducting segments completely expel the magnetic field as expected from theory [DD21].

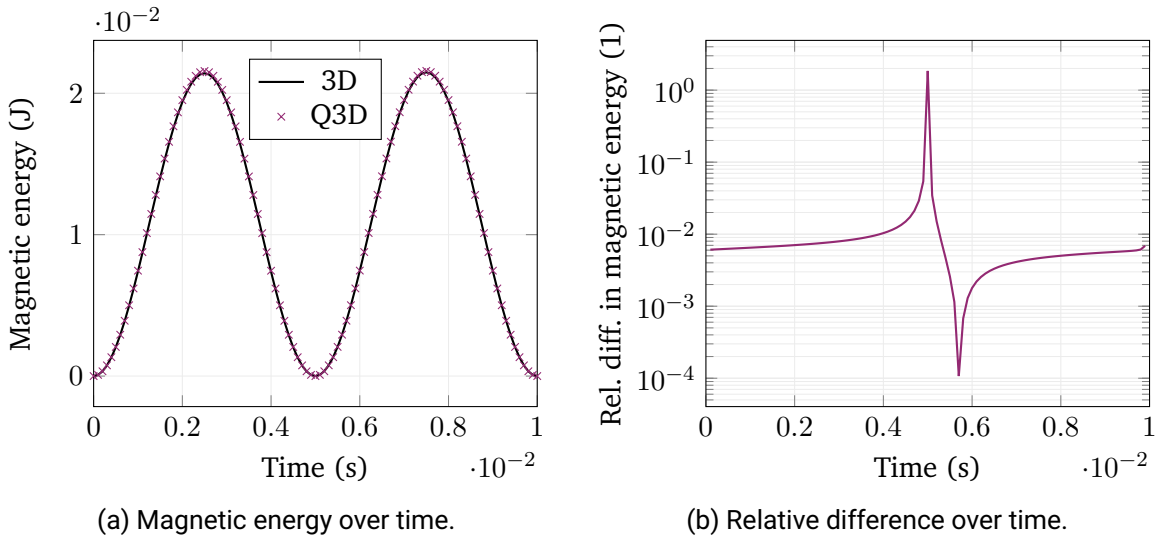


Figure 6.11.: Results for the superconducting cable model presented in Sec. 6.3. The magnetic energies obtained by the Q3D and 3D simulation are plotted over time, showing an excellent agreement (a). The relative difference between those is plotted over time, being on average in the magnitude of 10^{-2} (b). The outliers in the range [4 ms, 6 ms] are caused by rounding errors, as the energy approaches zero at 5 ms. Figures adapted from [DD21].

the full 3D FE simulation, the Q3D method demonstrated a superior computational efficiency while achieving an excellent accuracy.

6.4. Quench Simulation of a Superconducting Multi-Filamentary Wire

In the next step, a strongly coupled magneto-thermal quench simulation is conducted. A superconducting multi-filamentary wire with the quench state model introduced in Sec. 3.4 is considered. The results are verified against a 3D FE simulation, and were published in [DSD22].

Model and Scenario

A quarter of a superconducting multi-filamentary wire with rectangular form $V = [0, \ell_x] \times [0, \ell_y] \times [0, \ell_z]$ is considered, where $\ell_z \gg \ell_x, \ell_y$. An initial temperature distribution is defined, such that a central segment in longitudinal direction already quenches at the beginning of the simulation time window. The geometry is shown in Fig. 6.12. For the magnetic model, a quarter cylindrical air domain is put around the wire. Neumann BCs are set at the boundary in the xz -plane and yz -plane to represent symmetry planes. At the xy -plane and curved boundaries, homogeneous Dirichlet BCs are set to force the magnetic field to vanish. For the thermal model, it suffices to solve the thermal problem solely in the wire domain, where isothermal BCs are assumed at the wire fronts, and adiabatic BCs are set on the wire hull.

During the quench development over time, the temperature-dependent material properties are updated at the end of each time step according to the quench state model as discussed in Sec. 3.4. The nonlinear material distribution along the z -direction is resolved using the Chebyshev expansion and tensor contraction approach introduced in Sec. 4.4.

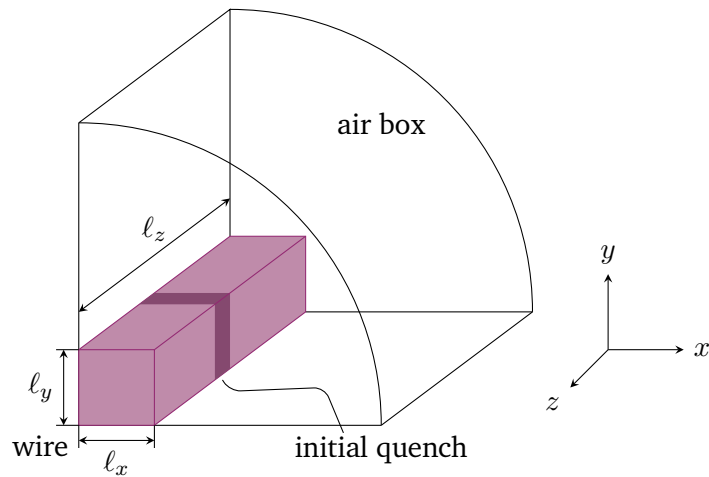


Figure 6.12.: Geometry of the quarter superconducting multi-filamentary wire model presented in Sec. 6.4. A quarter multi-filamentary wire (purple) is placed into an air box. The geometry is mirrored at the xz -plane and yz -plane to represent a full wire. An initial temperature distribution is defined, such that a segment of the wire (dark purple) is quenched at the beginning of the simulation time window. Figure adapted from [DSD22].

Simulation Results and Verification

The model is simulated using the Q3D method and compared to a conventional 3D FE simulation carried out in GetDP [Dul+98]. Attention has been paid to ensure that the numbers of FEs in the cross-section of both models are roughly the same to allow for comparability. The time range is run through a total of 25 constant time steps. The magnetic and thermal energy are computed in each time step by both solvers and compared to each other, see Fig. 6.13, showing an excellent agreement between the data.

Table 6.1 lists the number of SEs and the chosen polynomial order for the Q3D method, and compares the required number of FEs and the DoFs as well as the computation method of the 3D and Q3D solver. Due to the strong multi-scale nature of the model ($l_z \gg l_x, l_y$), it does not surprise that the 3D model demands for a high number of FEs to achieve an accurate meshing especially along the z -direction of the computational domain. On the other hand, thanks to the spectral discretization of the longitudinal dimension, the Q3D method achieves a high accuracy with much less DoFs in total. The ratios of the Q3D to 3D quantities in percent are given in the right-most column of Tab. 6.1. In the end, the Q3D discretization needs only approx. 1% as many DoFs as the conventional 3D simulation. As a consequence, on a standard workstation the transient solution of this scenario takes only five minutes employing the Q3D solver, while the 3D GetDP simulation takes one hour to run. This result underlines the computational superiority of the Q3D method against the conventional 3D FEM, which improves with increasing multi-scale ratio $\frac{l_z}{l_x + l_y}$.

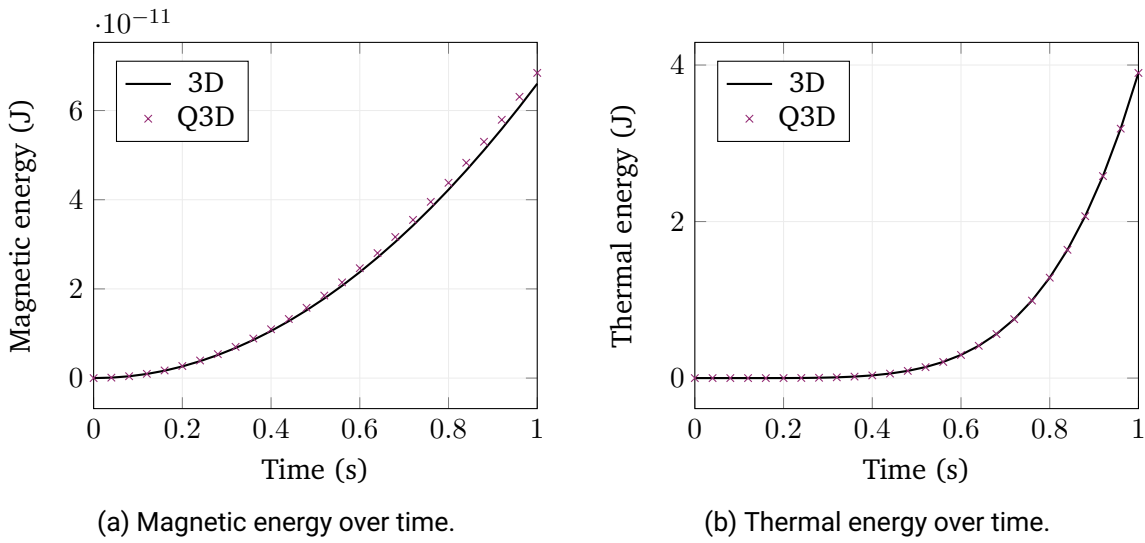


Figure 6.13.: Comparison of the magnetic and thermal energies obtained by the 3D and Q3D solver for the superconducting multi-filamentary wire model discussed in Sec. 6.4. In both cases, the Q3D solution aligns very well with the 3D reference solution. Figures taken from [DSD22].

Table 6.1.: Comparison between 3D FE and Q3D simulation for the model in Sec. 6.4.

	3D GetDP	Q3D solver	Ratio Q3D vs. 3D
#FE	1,863,431	330	0.01 %
#SE	–	5	–
Polynomial order	–	6	–
Magnetic #DoF	1,741,669	21,979	1 %
Thermal #DoF	80,735	806	1 %
Computation time	1 h	5 min	8 %

6.5. Quench Simulation of a Superconducting Coil (Lead Example)

In this final simulation study, the lead example presented in Sec. 3.1 is computed by a strongly coupled magneto-thermal Q3D simulation, which unites all introduced features of the Q3D simulation approach such as coil end effects and nonlinear material characteristics. Appendix B provides the physical data of this simulation study.

Model and Scenario

The considered superconducting coil model is shown in Fig. 3.2. Following the notation introduced in Sec. 3.5, the model is electrically connected to a constant direct voltage source u_{src} at Γ_1^+ and is grounded at Γ_{24}^+ by employing field-circuit coupling, see Sec. 4.5. Also, isothermal BCs are applied on these surfaces. The other half-turn end surfaces are electrically and thermally connected to each other as explained in Sec. 3.5. The electrical and thermal connections are modeled such that the current and the heat flux immediately enter the next half-turn upon reaching the end of a half-turn. At the hull of the coil Γ_{con} , constant Robin BCs are applied mimicking the liquid helium cooling.

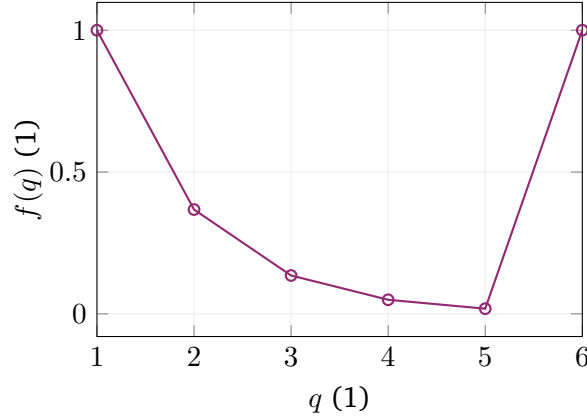


Figure 6.14.: The filter function (6.12) is plotted over the polynomial modes $q = 1, \dots, 6$ for $N = 5$. The higher the polynomial mode, the more the value of the respective spectral coefficient is diminished. The constant modes $q = 1$ and $q = N + 1$ are not modified.

At the beginning of the simulation time window $[0, 15]$ ms, the 15th half-turn is quenched at $z_q = \frac{\ell_z}{3}$. This is represented by an initial Gaussian temperature distribution

$$\vartheta(\vec{r}, t = 0) = \vartheta_0(\vec{r}) = \begin{cases} \vartheta_{\text{iso}} & \text{in } V_v, v \neq 15, \\ \frac{3}{2}\vartheta_{\text{crit}} \exp\left(-\frac{(z-z_q)^2}{\ell_q^2}\right) + \vartheta_{\text{iso}} & \text{in } V_{15}. \end{cases} \quad (6.11)$$

Here, $\ell_q = \frac{\ell_z}{100}$ in m is mathematically the Gaussian function's standard deviation, which approximately corresponds to the width of the increased temperature distribution in V_{15} . The choice of the initial hot-spot temperature $\max\{\vartheta_0\} = \frac{3}{2}\vartheta_{\text{crit}} + \vartheta_{\text{iso}}$ ensures that the model cannot recover from the local quench, but enters a state of thermal instability. This will lead to a quench development and, thus, a temperature increase in the whole coil.

Furthermore, two scenarios are considered: In the first scenario, the insulation between the cables is assumed to be very good, i.e. it is modeled with a low thermal conductivity, such that the ratio between the transversal thermal conductivity of the insulation $\lambda^{(t)}$ and the longitudinal thermal conductivity of the cable $\lambda^{(\ell)}$ is very low. In the second scenario, the insulation between the cables is less good, i.e. its thermal conductivity is higher, such that the transversal-longitudinal-ratio of the thermal conductivity is higher by an order of magnitude. This will result into different temperature developments and also quench propagation velocities.

Numerical Challenges

This model involves multiple connected half-turns and a high multi-scale ratio. This makes the choice of the optimal spectral discretization mesh non-trivial: The steep temperature gradients resemble discontinuities in longitudinal direction, which can induce numerical instability problems in the SE discretization part of the Q3D method if the spectral mesh is not chosen accordingly. However, the steep temperature fronts also move in time, making an adaptive mesh necessary as demonstrated in the Rutherford cable example in Sec. 6.2. In contrast to the Rutherford cable example, the half-turns of the considered superconducting coil model are connected to each other in longitudinal direction, which will lead to various quench front locations in the transversal

dimension. In this way, a spectral mesh, which is ideal for one half-turn, could be suboptimal for another half-turn. An adaptive mesh strategy for the Q3D method has to take these considerations into account.

Besides of an adaptive mesh strategy, there are different workarounds to deal with the presence of (quasi) discontinuities in spectral methods [PMS19]. This work utilizes a simple filter function

$$f(q) = \begin{cases} \exp(1 - q), & q < N + 1, \\ 1, & q = N + 1, \end{cases} \quad (6.12)$$

where q is the polynomial mode of the modified Lobatto polynomials. This function acts as a sort of low-pass filter, which diminishes the values of the higher-order coefficients, while not modifying the constant modes $q = 1$ and $q = N + 1$, see Fig. 6.14. Clearly, this procedure distorts the Q3D solution and counteracts the benefits of the Q3D method. For the sake of a proof of concept, however, the filtering approach leads to satisfactory results.

Simulation Results

Figure 6.15 and 6.16 show the temperature distribution at several time instances on a xz -plane slicing through the central half-turns V_{10}, \dots, V_{16} , see also the numbering scheme in Fig. 3.2, for the low and high transversal-longitudinal-ratio scenarios of the thermal conductivity, respectively. A red line marks the quench hot-spot location z_q in the longitudinal dimension.

In the low ratio scenario, due to the excellent thermal insulation properties of the glass fibre separating the half-turns from each other, the heat is primarily conducted from the hot-spot location in the 15th half-turn into longitudinal direction, see Fig. 6.15b. At the beginning, the quench development is rather slow, as one can see by comparing Fig. 6.15a and Fig. 6.15b. The more superconducting coil material is quenched, however, the more heat is generated by Ohmic losses. This accelerates the quench development, see Fig. 6.15c–6.15d.

Over time, the other half-turns $V_v, v \neq 15$ are heated up and quenched through the longitudinal heat conduction over the coil end windings, while the transversal heat conduction through the insulation layers plays a much smaller role. After 15 ms, the hot-spot temperature has increased to 85 K and multiple half-turns are quenched.

In the high ratio scenario, due to the worse thermal insulation properties of the glass fibre, the heat conduction is also conducted transversally from half-turn to half-turn, although the primary heat conduction still occurs in longitudinal direction. This leads to an ellipsoid heat development with its center at the quench hot-spot location z_q in V_{15} , see Fig. 6.16.

At the same time, the heat development is much faster than in the low ratio case. The hot-spot temperature of 85 K is already reached after 1.5 ms, so after a tenth of the time of the low ratio scenario.

The obtained simulation results are physically and qualitatively plausible. They show that the Q3D simulation approach is able to portray the quench development in a superconducting coil model by solving a transient and strongly coupled magneto-thermal problem and taking multiple half-turns, nonlinear material characteristics and coil end effects into account.

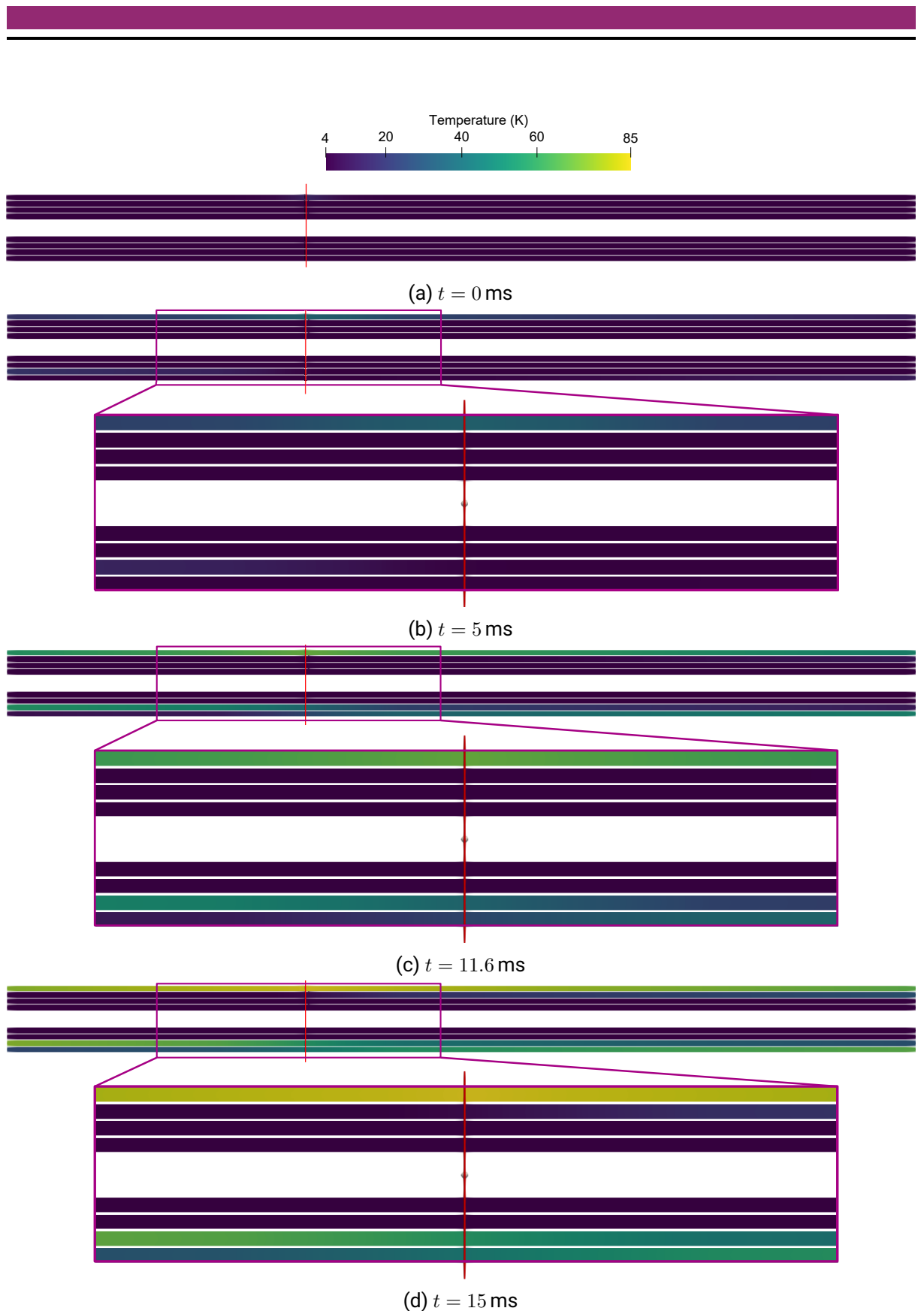


Figure 6.15.: Temperature development over time in the central half-turns V_9, \dots, V_{16} (see Fig. 3.2) from a xz -plane view ($y = 0$) for a low transversal-longitudinal thermal conductivity ratio. The initial temperature increase in V_{15} (top half-turn) primarily leads to a heat conduction in longitudinal direction. The red line marks the quench hot-spot z_q .

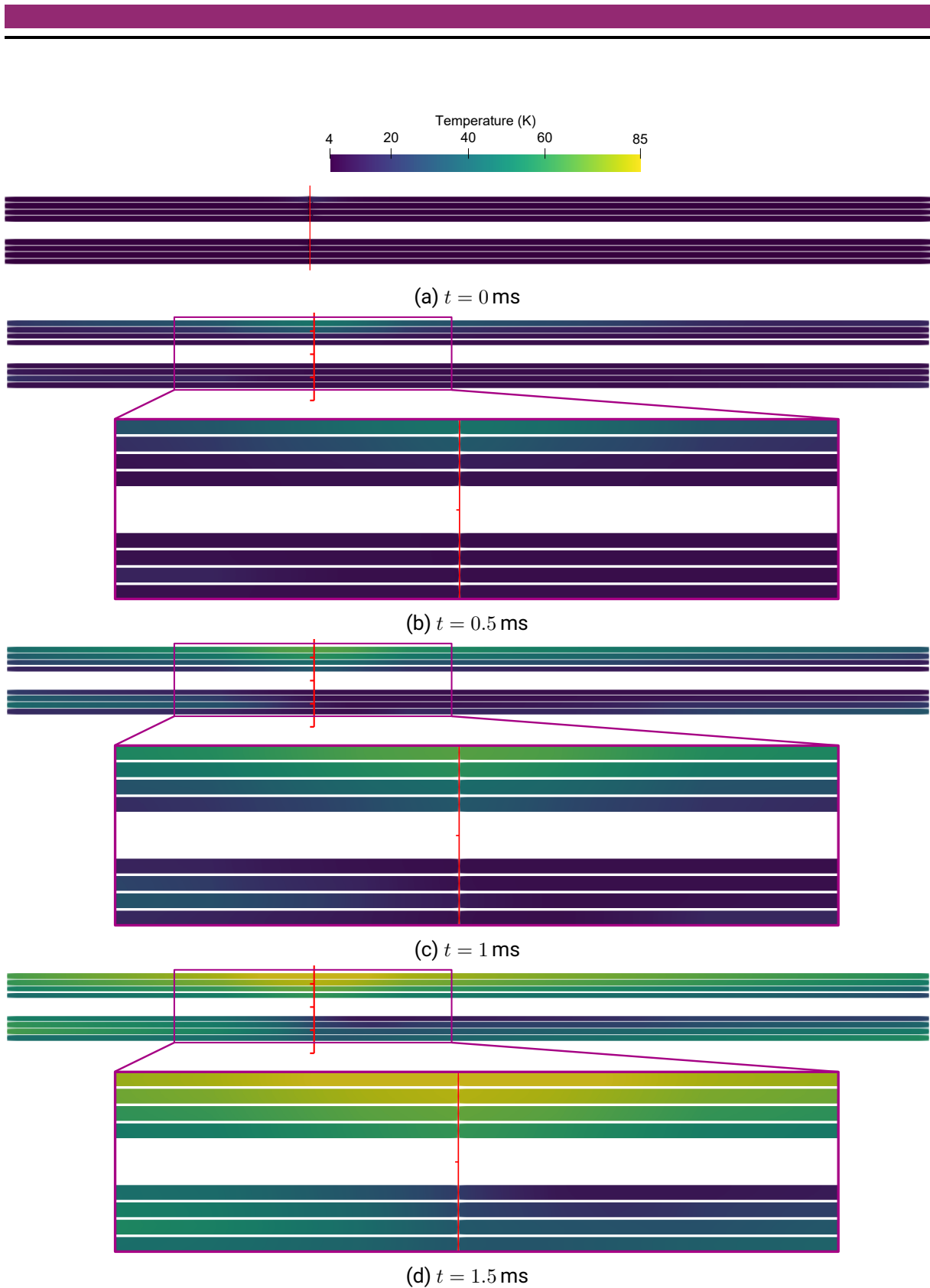


Figure 6.16.: Temperature development over time in the central half-turns V_9, \dots, V_{16} (see Fig. 3.2) from a xz -plane view ($y = 0$) for a high transversal-longitudinal thermal conductivity ratio. The initial temperature increase in V_{15} (top half-turn) leads to an ellipsoidal heat conduction with its major axis in the longitudinal direction. The red line marks the quench hot-spot z_q .

7. Summary, Conclusions and Outlook

Geschichten haben nie ein Ende [...], auch wenn uns die Bücher das gern vorgaukeln. Die Geschichten gehen immer weiter, sie enden ebenso wenig mit der letzten Seite, wie sie mit der ersten beginnen.

Cornelia Funke, *Tintenblut*

7.1. Summary

This thesis was dedicated to the improvement of the spatial resolution for the multi-scale problem of quench simulation of superconducting accelerator magnets. This is necessary to determine sharp but reliable thresholds for quench detection and to design secure shutdown processes in the case of quench scenarios. A quasi-3D method with hybrid shape functions was developed, which combined 2D finite elements in the transversal cross-section of the magnet with 1D spectral elements in the longitudinal dimension. In this way, the method was able to resolve all geometrical details in the magnet cross-section as well as the steep temperature gradients due to the quench phenomenon along the magnet's length.

For the quasi-3D quench simulation, the magnetic and thermal models were derived. Herein, the interfilament current coupling phenomenon was included by an additional term in the magnetoquasistatic formulation representing the magnetization current density in the superconducting material induced by an external magnetic field. Furthermore, a smooth quench state model was introduced, which was based on the current sharing phenomenon. In this way, the convergence of nonlinear iteration schemes was secured. To take the coil end effects into account, this thesis developed end winding models for the thermal and magnetic sub-problems by means of floating boundary conditions and electrical field-circuit coupling, respectively.

For the spectral element component of the quasi-3D method, this thesis investigated the suitability of several orthogonal polynomial bases with respect to computational efficiency. In the end, the modified Lobatto polynomials proved to be the ideal polynomial basis for this quasi-3D method. Moreover, this thesis developed an efficient nonlinear iteration scheme for the SE part using Chebyshev polynomials and tensor contraction. In doing so, the computational effort for the assembly of the nonlinear spectral element matrices and, thus, nonlinear quasi-3D matrices was optimized.

The magneto-thermal model for quench simulation was discretized by means of quasi-3D nodal and edge shape functions. The arising sub-terms of the discrete quasi-3D quantities were identified with 2D finite element and 1D spectral element matrices and vectors. The treatment of the boundaries of the quasi-3D computational model was discussed, and several boundary

conditions, which are relevant for quench simulation, were formulated for the quasi-3D setting. The whole quasi-3D simulation approach was implemented in an object-oriented MATLAB framework.

Convergence studies and reference simulations verified the numerical correctness of the quasi-3D method. The quasi-3D simulation approach was then successfully employed in a thermal and magnetic simulation study of superconducting cables. Furthermore, strongly coupled nonlinear magneto-thermal simulations of a superconducting multi-filamentary wire and a superconducting coil were conducted. Comparisons with conventional 3D finite element solvers showed that the quasi-3D method achieved excellent accuracy while also attaining a higher computational efficiency.

7.2. Conclusions

This thesis raised the following conclusions and findings:

- As already known from axisymmetric quasi-3D methods [DD17; DSD19], the discrete quantities of the translational quasi-3D method presented in this dissertation could be written in a concise way using the Kronecker tensor product notation. Thanks to the mixed nodal-modal nature of the modified Lobatto polynomials, boundary and continuity conditions could be easily imposed without increasing the system of equations.
- The implementation of the quasi-3D solver is particularly cumbersome. All details have to be considered very carefully. Every possibility for structuring the algorithm, and by that also the implementation, e.g. the Kronecker product structure, is helpful and necessary. Comparing to a standard 3D finite element solver, the coding of the quasi-3D solver is significantly larger and more vulnerable.
- The quasi-3D discretization technique is motivated by the translational symmetry of the considered magnet models. Moreover, it has been shown that the resolution in the longitudinal direction has to be adapted to the quench hot-spot and even adapted to its development over time. This indicates a tighter link between model and solver than is the case in a standard 3D finite element simulation procedure. The employment of the computationally beneficial quasi-3D method necessitates a tighter connection between solver and pre- and post-processing routines, which is a disadvantage in the working flow of a computational engineer.
- In comparison to standard finite element solvers, the treatment of nonlinearities is not straightforward in the quasi-3D method. This problem was partially unforeseen. However, the introduction of tensor contractions could alleviate the problem.
- Because of the spectral element parts, the resulting systems of equations have comparably high condition numbers. As a consequence, a high-quality algebraic solver is needed. In this work, for larger problems, the standard sparse direct solver of MATLAB did not suffice and had to be replaced with MUMPS [ADL00].
- Convergence studies of the quasi-3D method confirmed the expected polynomial convergence of the transversal discretization (from finite element theory [Bra12]) as well as the expected exponential convergence of the longitudinal discretization (from spectral element theory [STW11]).

-
- The quasi-3D method has confirmed the anticipated improvement in spatial resolution for the case of superconducting accelerator magnets. This effect is more pronounced, the higher the multi-scale ratio is, i.e. the longer the magnet is compared to its width.

In total, the quasi-3D simulation approach demands for a very careful implementation as well as a tighter connection between model and solver than a standard 3D finite element simulation would need. However, this overhead is rewarded with a promising tool to study strongly coupled nonlinear 3D magneto-thermal quench scenarios especially in long superconducting accelerator magnets, where the multi-scale ratio is very high.

7.3. Outlook

The results presented in this thesis raise new research proposals to be tackled in future work:

- For a precise and numerically stable simulation of the quench development in longitudinal dimension, the spectral mesh in the quasi-3D simulation approach has not only to be carefully chosen, but to be adapted over time in order to resolve the moving quench fronts. Otherwise, inaccurate results and numerical instabilities can occur as demonstrated in Sec. 6.2 and Sec. 6.5. Thus, adaptive quasi-3D mesh strategies could be adopted, which efficiently adapt the quasi-3D discretization to the quench state of the model and ensure a high computational accuracy.
- The Kronecker tensor product structure of the quasi-3D matrices leads to special matrix properties as discussed in Sec. 5.2. In analogy to the Kronecker product matrices arising in Runge-Kutta time integration [Boo+07] or in stochastic collocation [RV10] for partial differential equations, these matrix structures could be exploited to develop dedicated algebraic techniques for solving quasi-3D systems of equations based on multilevel solvers.
- The quasi-3D matrix structures could be also investigated for the construction of a customized preconditioner, which enables the efficient usage of iterative methods for the solution of the quasi-3D systems of equations. In this way, the currently employed explicit Coulomb gauge could be omitted in favor of the implicit gauging provided by iterative methods [Ren96]. Alternatively, a tree-cotree gauging method [MC95] for the quasi-3D discretization could be designed. Both alternatives would reduce the size of the magnetic system and, thus, could improve the overall computational efficiency.

As a numerical technique for spatial discretization, the quasi-3D method is not constrained to low-temperature superconducting magnet models or quench simulation, but can be adapted for other applications fulfilling the translational symmetry condition, e.g. for electrical machines [Jor+12]. In particular, the quench simulation of high-temperature superconducting tapes represents a natural application field for the quasi-3D method: Due to the presence of several thin layers of different materials and a high multi-scale ratio, conventional three-dimensional quench simulations of superconducting tapes are computationally very demanding, and have been carried out only for very simple models up to now [Gri16]. The quasi-3D simulation approach could be able to solve this multi-scale problem, thus becoming a promising alternative to the semi-analytical and two-dimensional simulation approaches used so far.

Moreover, analogously to other spatial discretization techniques, the quasi-3D method can be combined with other numerical methods in order to complement each other in their respective

roles and to reach even higher levels of computational efficiency. Candidates for such joint approaches are:

- **Domain decomposition:** This work modeled the magnet's end windings by a circuit model, which was monolithically coupled to the quasi-3D model. As an alternative, the end part could be modeled by a 3D finite element method and attached to the quasi-3D model by a domain decomposition approach [SBG96]. In this way, the quench development in the end windings could be resolved more accurately.
- **Higher-order time integrators:** An improvement of the temporal resolution and the computational efficiency can be achieved by introducing higher-order time integrators, e.g. Runge-Kutta methods [ND96; Boo+07], preferably with error-controlled adaptive time stepping [CWW02].
- **Data-driven solvers:** The properties of superconducting materials impose a huge challenge both modeling-wise and simulation-wise. First, the material characteristics are highly nonlinear or even discontinuous. For example, the electrical conductivity and the volumetric heat capacity of superconducting materials jump upon shifting from superconducting to normalconducting state and vice versa [Rus10]. Numerically, this induces convergence problems for the nonlinear iteration scheme. This thesis remedied that issue by introducing a smooth quench state model in Sec. 3.4. Second, measuring the material characteristics at the very low temperatures, in which superconducting magnets are operated, is extremely challenging. This already uncertain measurement data is then piece-wise polynomially fitted to obtain a material curve for quench simulation [Rus10]. In order to avoid these inaccurate measurement data approximations, future work could look into the fusion of a quasi-3D simulation approach with a data-driven solver, which skips the fiddly material modeling and directly works with the measurement data [GLD20]. Thus, highly nonlinear and discontinuous material characteristics could be handled in a genuine way, leading to a further increase of both the computational accuracy and the computational efficiency.
- **Reduced magnetic vector potential formulations:** In this thesis, the superconducting cable is spatially resolved by the combination of the 2D finite element mesh and a 1D spectral element grid. Herein, the superconducting wires are not explicitly modeled but a homogenization technique is employed. A promising alternative is to use a reduced magnetic vector potential formulation, where the superconducting wires in the cable are explicitly resolved [Pau97]. This approach has been implemented in the ROXIE software [Rus98], which has been particularly advantageous for optimizing the magnet's winding geometry [AR04] and for modeling the occurring induced effects [VAR00; ARV02]. In ROXIE, the wires are embedded in a boundary element domain, which is coupled to a finite element domain dealing with the permeable magnet parts. A similar approach, which embedded the wires in a finite element domain, exists as well [DAn+22]. Here, a replacement of the 3D finite element approach by a quasi-3D method would bring decisive advantages.
- **LEDET:** LEDET (lumped-element dynamic electro-thermal) is an efficient solver for quench phenomena, employing coupled electric and thermal circuits [Rav+16]. A hybridization of LEDET and a field solver, e.g., including the quasi-3D approach, would make sense to adapt the spatial resolution to the problem at hand, e.g., by coupling highly resolved field model parts in smaller, particularly vulnerable parts to electro-thermal circuits of the overall coil. The mechanism of field-circuit coupling developed in this thesis can be extended to that purpose.

A. Matrix Calculations

A.1. 2D FE Matrices

In the following, all 2D FE matrices occurring in Sec. 4.3 are calculated in detail. To this end, it is more convenient to not use the global shape function (4.34) on the image element T but the local shape functions \hat{N}_j defined on the reference element \hat{T} . The reference triangle is depicted in Fig. A.1. For the reference triangle, the reference nodal shape functions read

$$\hat{N}_1(\hat{x}, \hat{y}) = 1 - \hat{x} - \hat{y}, \quad (\text{A.1a})$$

$$\hat{N}_2(\hat{x}, \hat{y}) = \hat{x}, \quad (\text{A.1b})$$

$$\hat{N}_3(\hat{x}, \hat{y}) = \hat{y}, \quad (\text{A.1c})$$

where (\hat{x}, \hat{y}) are the spatial coordinates in the reference coordinate system. The reference transversal edge functions read

$$\hat{w}_1^{(t)}(x, y) = \hat{w}_{(1,2)}^{(t)}(x, y) = \begin{bmatrix} 1 - \hat{y} \\ \hat{x} \end{bmatrix}, \quad (\text{A.2a})$$

$$\hat{w}_2^{(t)}(x, y) = \hat{w}_{(1,3)}^{(t)}(x, y) = \begin{bmatrix} \hat{y} \\ 1 - \hat{x} \end{bmatrix}, \quad (\text{A.2b})$$

$$\hat{w}_3^{(t)}(x, y) = \hat{w}_{(2,3)}^{(t)}(x, y) = \begin{bmatrix} -\hat{y} \\ \hat{x} \end{bmatrix}. \quad (\text{A.2c})$$

With the affine mapping $F_T(\hat{x}, \hat{y}) \mapsto (x, y)$,

$$F_T(\hat{x}, \hat{y}) = B_T \begin{bmatrix} \hat{x} \\ \hat{y} \end{bmatrix} + a_T, \quad (\text{A.3})$$

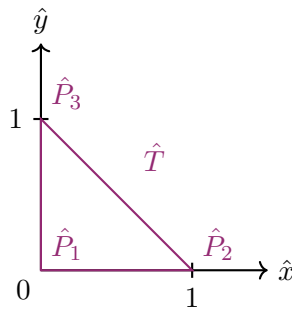


Figure A.1.: Reference triangle for standard 2D FEM [ZTT05].

it is possible to map coordinates from the reference system into the image system (x, y) , and vice versa with the inverse F_T^{-1} [Bra12]. The mapping matrix B_T and mapping vector a_T are readily obtained from the node coordinates forming the image element T [ZTT05]. In the context of matrix assembly, one has also to map integrals and gradients involving nodal shape functions. To this end, the transformation rules

$$\int_{T=F_T(\hat{T})} u(x, y) \, dx dy = \int_{\hat{T}} \hat{u}(\hat{x}, \hat{y}) |\det B_T| \, d\hat{x} d\hat{y}, \quad (\text{A.4})$$

$$\nabla u(x, y) = B_T^{-T} \hat{\nabla} \hat{u}(\hat{x}, \hat{y}) \quad (\text{A.5})$$

are utilized [Bra12]. In the context of edge shape functions, it is crucial to use a $H(\text{curl})$ -conforming mapping to map between reference and image coordinates, which is provided by the Piola transformation [RKL09]

$$\vec{v}(x, y) = B_T^{-T} \hat{v}(\hat{x}, \hat{y}), \quad (\text{A.6})$$

$$\nabla \times \vec{v}(x, y) = \frac{1}{\det B_T} B_T \hat{\nabla} \times \hat{v}(\hat{x}, \hat{y}). \quad (\text{A.7})$$

Thermal Conductance Matrix

For the thermal conductance matrix (4.17), the integral transformation rule (A.4) and the gradient transformation (A.5) are used to obtain

$$\begin{aligned} \left(\mathbf{K}_\lambda^{\text{FE,n}} \right)_{ij}^{(T)} &= \int_T \lambda^{(T)} \nabla N_j^{(T)} \cdot \nabla N_i^{(T)} \, dx dy \\ &= \int_{\hat{T}} \lambda^{(T)} \left(B_T^{-T} \hat{\nabla} \hat{N}_j \right) \cdot \left(B_T^{-T} \hat{\nabla} \hat{N}_i \right) |\det B_T| \, d\hat{x} d\hat{y} \\ &= |\hat{T}| |\det B_T| \lambda^{(T)} \left(B_T^{-T} \hat{\nabla} \hat{N}_j \right) \cdot \left(B_T^{-T} \hat{\nabla} \hat{N}_i \right). \end{aligned} \quad (\text{A.8})$$

Note that for linear nodal shape functions, the gradients are constants. Therefore, no numerical integration is necessary.

Thermal Capacitance Matrix

For the thermal capacitance matrix (4.18), the integral transformation rule (A.4) and exact integration are used to obtain

$$\begin{aligned} \left(\mathbf{M}_{C_V}^{\text{FE,n}} \right)_{ij}^{(T)} &= \int_T C_V^{(T)} N_j^{(T)} N_i^{(T)} \, dx dy \\ &= \int_{\hat{T}} C_V^{(T)} \hat{N}_j \hat{N}_i |\det B_T| \, d\hat{x} d\hat{y} \\ &= \frac{|\hat{T}| |\det B_T|}{12} C_V^{(T)} \begin{bmatrix} 2 & 1 & 1 \\ 1 & 2 & 1 \\ 1 & 1 & 2 \end{bmatrix}. \end{aligned} \quad (\text{A.9})$$

Thermal Load Vector

For the thermal load vector (4.19), the integral transformation rule (A.4) and numerical integration on the triangle [Dun85] of order Q are used to obtain

$$\begin{aligned}
 (\mathbf{q}_V^{\text{FE}})_i^{(T)} &= \int_T q_V N_i \, dx dy \\
 &= \int_{\hat{T}} q_V \hat{N}_i | \det B_T | \, d\hat{x} d\hat{y} \\
 &= |\hat{T}| | \det B_T | \sum_{q=1}^{N_Q} \omega_q q_V(x_q, y_q) \hat{N}_i(\hat{x}_q, \hat{y}_q),
 \end{aligned} \tag{A.10}$$

where N_Q is the number of quadrature samples for an integration of order Q , ω_q are the quadrature weights and (x_q, y_q) and (\hat{x}_q, \hat{y}_q) are the quadrature samples in the image and reference coordinate system, respectively. For $Q = 1$, the volumetric heat flux is assumed to be element-wise constant.

Transversal Magnetic Reluctance Matrix

For the transversal magnetic reluctance matrix (4.45), the integral transformation rule (A.4) and the curl transformation (A.7) are used to obtain

$$\begin{aligned}
 (\mathbf{K}_\alpha^{\text{FE,t}})_{de}^{(T)} &= \int_T \alpha^{(T)} \nabla \times \vec{w}_e^{(T,t)}(x, y) \cdot \nabla \times \vec{w}_d^{(T,t)}(x, y) \, dx dy \\
 &= \int_{\hat{T}} \alpha^{(T)} \frac{1}{| \det B_T |} \hat{\nabla} \times \hat{w}_e^{(t)}(\hat{x}, \hat{y}) \cdot \frac{1}{| \det B_T |} \hat{\nabla} \times \hat{w}_d^{(t)}(\hat{x}, \hat{y}) | \det B_T | \, d\hat{x} d\hat{y} \\
 &= \alpha^{(T)} \frac{|\hat{T}|}{| \det B_T |} \begin{bmatrix} 4 & -4 & 4 \\ -4 & 4 & -4 \\ 4 & -4 & 4 \end{bmatrix}.
 \end{aligned} \tag{A.11}$$

Transversal Electrical Conductance Matrix

For the transversal electrical conductance matrix, the integral transformation rule (A.4) and the Piola transformation (A.6) is used to obtain

$$\begin{aligned}
 (\mathbf{M}_\sigma^{\text{FE,t}})_{de}^{(T)} &= \int_T \sigma^{(T)} \vec{w}_e^{(T,t)}(x, y) \cdot \vec{w}_d^{(T,t)}(x, y) \, dx dy \\
 &= \int_{\hat{T}} \sigma^{(T)} \left(B_T^{-\top} \hat{w}_e^{(t)}(\hat{x}, \hat{y}) \right) \cdot \left(B_T^{-\top} \hat{w}_d^{(t)}(\hat{x}, \hat{y}) \right) | \det B_T | \, d\hat{x} d\hat{y}.
 \end{aligned} \tag{A.12}$$

Here, the integrand is a function of second order which is calculated using exact numerical integration on the reference triangle [Dun85].

Node-Edge Coupling Matrix

For the node-edge coupling matrix, the integral transformation rule (A.4), the gradient transformation (A.5) and the Piola transformation (A.6) are used to obtain

$$\begin{aligned}
 (\mathbf{C}_\alpha^{\text{FE},t})_{ie}^{(T)} &= \int_T \alpha^{(T)} \vec{w}_e^{(T,t)}(x, y) \cdot \nabla N_i^{(T)}(x, y) \, dx dy \\
 &= \int_{\hat{T}} \alpha^{(T)} \left(B_T^{-\top} \hat{w}_e^{(t)}(\hat{x}, \hat{y}) \right) \cdot \left(B_T^{-\top} \hat{\nabla} \hat{N}_i(\hat{x}, \hat{y}) \right) |\det B_T| \, d\hat{x} d\hat{y}.
 \end{aligned} \tag{A.13}$$

Here, the integrand is a function of first order which is calculated using exact numerical integration on the reference triangle [Dun85].

Longitudinal Magnetic Reluctance Matrix

For the longitudinal magnetic reluctance matrix, the integral transformation rule (A.4) and the gradient transformation (A.5) are used to obtain

$$\begin{aligned}
 (\mathbf{K}_\alpha^{\text{FE},\ell})_{ij}^{(T)} &= \int_T \alpha^{(T)} \nabla N_j^{(T)}(x, y) \cdot \nabla N_i^{(T)}(x, y) \ell_z^{-2} \, dx dy \\
 &= \int_{\hat{T}} \alpha^{(T)} \left(B_T^{-\top} \hat{\nabla} \hat{N}_j(\hat{x}, \hat{y}) \right) \cdot \left(B_T^{-\top} \hat{\nabla} \hat{N}_i(\hat{x}, \hat{y}) \right) |\det B_T| \ell_z^{-2} \, d\hat{x} d\hat{y} \\
 &= |\hat{T}| |\det B_T| \alpha^{(T)} \left(B_T^{-\top} \hat{\nabla} \hat{N}_j(\hat{x}, \hat{y}) \right) \cdot \left(B_T^{-\top} \hat{\nabla} \hat{N}_i(\hat{x}, \hat{y}) \right) \ell_z^{-2}.
 \end{aligned} \tag{A.14}$$

Note that for linear nodal shape functions, the gradients are constants. Therefore, no numerical integration is necessary.

Alternatively, one can retain the curl formulation and use the curl transformation (A.7),

$$\begin{aligned}
 (\mathbf{K}_\alpha^{\text{FE},\ell})_{ij}^{(T)} &= \int_T \alpha^{(T)} \left(\nabla \times \frac{N_j^{(T)}(x, y)}{\ell_z} \vec{e}_z \right) \cdot \left(\nabla \times \frac{N_i^{(T)}(x, y)}{\ell_z} \vec{e}_z \right) \, dx dy \\
 &= \int_{\hat{T}} \frac{\alpha^{(T)}}{\ell_z^2} \left(\frac{1}{\det B_T} B_T \hat{\nabla} \times \hat{N}_j(\hat{x}, \hat{y}) \vec{e}_z \right) \cdot \left(\frac{1}{\det B_T} B_T \hat{\nabla} \times \hat{N}_i(\hat{x}, \hat{y}) \vec{e}_z \right) |\det B_T| \, d\hat{x} d\hat{y} \\
 &= \frac{\alpha^{(T)}}{\ell_z^2} \frac{|\hat{T}|}{|\det B_T|} \left(B_T \begin{bmatrix} \partial_{\hat{y}} \hat{N}_j(\hat{x}, \hat{y}) \\ -\partial_{\hat{x}} \hat{N}_j(\hat{x}, \hat{y}) \end{bmatrix} \right) \cdot \left(B_T \begin{bmatrix} \partial_{\hat{y}} \hat{N}_i(\hat{x}, \hat{y}) \\ -\partial_{\hat{x}} \hat{N}_i(\hat{x}, \hat{y}) \end{bmatrix} \right),
 \end{aligned} \tag{A.15}$$

which is equivalent to (A.14).

Longitudinal Winding Matrix

For the longitudinal winding matrix, the integration transformation rule (A.4) is used to obtain

$$\begin{aligned}
 (\mathbf{X}^{\text{FE},\ell})_{is}^{(T)} &= \int_T T_s(x, y) N_i^{(T)}(x, y) \ell_z^{-1} dx dy \\
 &= \int_{\hat{T}} T_s(x, y) \hat{N}_i(\hat{x}, \hat{y}) |\det B_T| d\hat{x} d\hat{y} \\
 &= \begin{cases} \frac{|\hat{T}| |\det B_T|}{6\ell_z} [1, 1, 1]^\top, & T \in S_s, \\ 0, & T \notin S_s, \end{cases}
 \end{aligned} \tag{A.16}$$

where S_s is the subregion of the s -th winding or strand.

A.2. 1D SE Modified Lobatto Matrices

In the following, the closed forms of all 1D SE matrices with modified Lobatto polynomial basis are presented [FD15]. To this end, the reference interval \hat{I} is mapped to the image interval I_k using a linear mapping

$$\hat{z} = b_k z + a_k \tag{A.17}$$

with mapping coefficients

$$a_k = \frac{z_{k+1} + z_k}{2}, \tag{A.18}$$

$$b_k = \frac{z_{k+1} - z_k}{2}. \tag{A.19}$$

This leads to the transformation rules

$$\int_{I_k} u(z) dz = \int_{\hat{I}} u(\hat{z}) b_k d\hat{z}, \tag{A.20}$$

$$\phi_q^{(k)}(z) = b_k^{-1} \hat{\phi}_q(\hat{z}). \tag{A.21}$$

Spectral Stiffness Matrix

Using (A.20) and (A.21), the spectral stiffness matrix (4.77) results to

$$\begin{aligned}
 (\mathbf{K}_\alpha^{\text{SE}})_{pq}^{(k)} &= \frac{\alpha^{(k)}}{b_k} \left\{ \frac{p^2(p-1)^2}{8(2p-1)} \delta_{pq} \right. \\
 &\quad \left. + \frac{1}{2} (\delta_{p,1} \delta_{q,1} + \delta_{p,N+1} \delta_{q,N+1} - \delta_{p,1} \delta_{q,N+1} - \delta_{p,N+1} \delta_{q,1}) \right\}.
 \end{aligned} \tag{A.22}$$

Spectral Damping Matrix

Using (A.20) and (A.21), the spectral damping matrix (4.78) results to

$$\begin{aligned}
 (\mathbf{D}_{\beta}^{\text{SE}})^{(k)}_{pq} = \beta^{(k)} & \left\{ \frac{p^2(p+1)(p-1)}{8(2p+1)(2p-1)} \delta_{p,q+1} \right. \\
 & - \frac{p(p-2)(p-1)^2}{8(2p-3)(2p-1)} \delta_{p,q-1} \\
 & + \frac{1}{2} (\delta_{p,1} \delta_{q,N+1} + \delta_{p,N+1} \delta_{q,N+1} - \delta_{p,1} \delta_{q,1} - \delta_{p,N+1} \delta_{q,1}) \\
 & \left. + \frac{1}{6} (\delta_{p,1} \delta_{q,2} + \delta_{p,2} \delta_{q,N+1} - \delta_{p,2} \delta_{q,1} - \delta_{p,N+1} \delta_{q,2}) \right\}. \tag{A.23}
 \end{aligned}$$

Spectral Mass Matrix

Using (A.20), the spectral mass matrix (4.79) results to

$$\begin{aligned}
 (\mathbf{M}_{\gamma}^{\text{SE}})^{(k)}_{pq} = \gamma^{(k)} b_k & \left\{ \frac{1}{4} \frac{p^2(p-1)^2}{(2p-3)(2p-1)(2p+1)} \delta_{pq} \right. \\
 & - \frac{1}{8} \frac{p(p-1)(p+1)(p+2)}{(2p-1)(2p+1)(2p+3)} \delta_{p,q-2} \\
 & - \frac{1}{8} \frac{p(p-3)(p-2)(p-1)}{(2p-5)(2p-1)(2p+1)} \delta_{p,q+2} \\
 & + \frac{1}{3} (2\delta_{p,1} \delta_{q,1} + 2\delta_{p,N+1} \delta_{q,N+1} + \delta_{p,1} \delta_{q,N+1} + \delta_{p,N+1} \delta_{q,1}) \\
 & + \frac{1}{6} (\delta_{p,1} \delta_{q,2} + \delta_{p,2} \delta_{q,1} + \delta_{p,2} \delta_{q,N+1} + \delta_{p,N+1} \delta_{q,2}) \\
 & \left. + \frac{1}{10} (\delta_{p,3} \delta_{q,N+1} + \delta_{p,N+1} \delta_{q,3} - \delta_{p,1} \delta_{q,3} - \delta_{p,3} \delta_{q,1}) \right\}. \tag{A.24}
 \end{aligned}$$

B. Physical Data

This chapter provides the physical data used for the superconducting coil lead example simulation in Sec. 6.5.

B.1. Magnetic Properties

Electrical Conductivity

The effective electrical conductivity of the cables is modeled as a temperature-dependent function

$$\sigma_{\text{Cable}}(\vartheta) = q_{\text{qs}}(\vartheta) (\kappa_{\text{Cu}} \rho_{\text{Cu}}(\vartheta, B = 0) + \kappa_{\text{SC}} \rho_{\text{NbTi}}(\vartheta))^{-1} \quad (\text{B.1})$$

with ρ_{Cu} being the electrical resistivity of copper following the National Institute of Standards and Technology (NIST) [Rus10; SDR92], and ρ_{NbTi} as the electrical resistivity of NbTi based on the material data compilation of the European Fusion Development Agreement (EFDA) [Rus10; BRS07]. Figure B.1a shows the relation (B.1) in the temperature range [4, 25] K. Note that in the fully superconducting state ($\vartheta \leq \vartheta_{\text{cs}} = 6.5$ K), $\sigma_{\text{Cable}} = 0$ due to the characteristics of the quench state function q_{qs} (see Sec. 3.4). This does not mean that the cable is viewed as non-conducting, but that the Ohmic eddy current effects and losses are disregarded in that state.

For the insulation wrapped around the individual cables as well as the air domain around the coil, the electrical conductivity is set to zero.

Characteristic Time Constant

The IFCC time constant of the cables is modeled as a temperature-dependent function

$$\tau_{\text{Cable}}(\vartheta) = (1 - q_{\text{qs}}(\vartheta)) \tau_{\text{SC}} \quad (\text{B.2})$$

with $\tau_{\text{SC}} = 20$ ms.

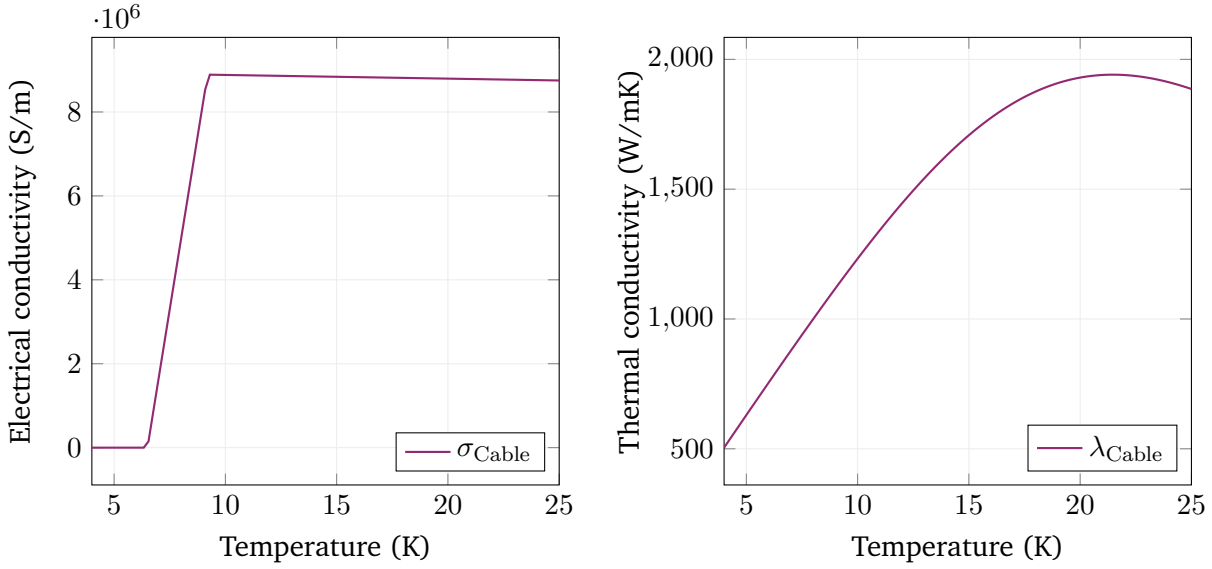
B.2. Thermal Properties

Thermal Conductivity

The thermal conductivity of the cables is modeled as a temperature-dependent function

$$\lambda_{\text{Cable}}(\vartheta) = \kappa_{\text{Cu}} \lambda_{\text{Cu}}(\vartheta, \text{RRR} = 100) + \kappa_{\text{SC}} \lambda_{\text{NbTi}}(\vartheta) \quad (\text{B.3})$$

with λ_{Cu} being the thermal resistivity of copper for a residual-resistance ratio (RRR) of 100 following NIST [Rus10; SDR92], and λ_{NbTi} as the thermal conductivity of NbTi based on the



(a) Effective electrical conductivity of the cable (B.1) for $B = 0$. (b) Effective thermal conductivity of the cable (B.3) for $RRR = 100$.

Figure B.1.: Effective temperature-dependent electrical and thermal conductivity of the cables.

material data compilation of EFDA [Rus10; BRS07]. Figure B.1b shows the relation (B.3) in the temperature range $[4, 25]$ K.

For the insulation, the thermal conductivity is modeled as a temperature-dependent function in the case of the lower ratio between transversal and longitudinal thermal conductivity (see Fig. 6.15),

$$\lambda_{\text{Ins,low}}(\vartheta) = 10^{p(\vartheta)} \quad \text{with} \quad p(\vartheta) = \sum_{n=0}^7 a_n (\log \vartheta)^n, \quad (\text{B.4})$$

with empirical parameters a_n taken from [Rus10]. Figure B.2 shows this relation in the temperature range $[4, 25]$ K. In the case of the higher transversal-longitudinal-ratio (see Fig. ...), the thermal conductivity is set to a constant value,

$$\lambda_{\text{Ins,high}} = 2.5 \text{ W/mK}. \quad (\text{B.5})$$

Volumetric Heat Capacity

The volumetric heat capacities of the cable and the insulation are set to constant values,

$$C_{V,\text{Cable}} = 500 \text{ J}/(\text{m}^3\text{K}), \quad (\text{B.6})$$

$$C_{V,\text{Ins}} = 750 \text{ J}/(\text{m}^3\text{K}). \quad (\text{B.7})$$

Robin Boundary Data

The Robin BC is mimicking the cooling helium fluid surrounding the coil. The helium's very high thermal conductivity is taken into account by a very high heat transfer coefficient in the Robin

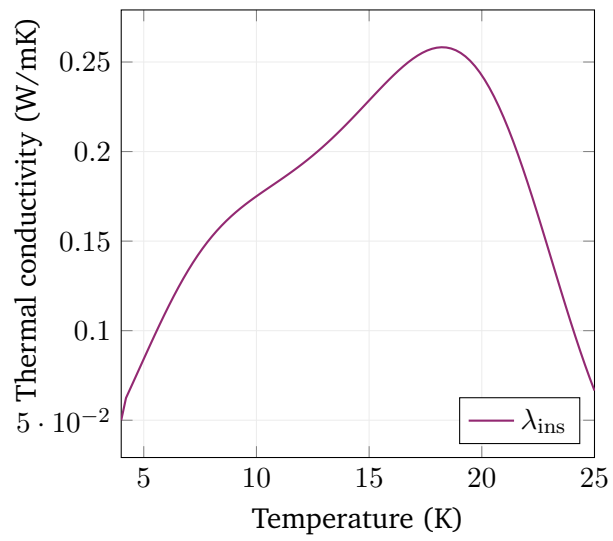


Figure B.2.: Thermal conductivity of the cable insulation (B.4) in the low transversal-longitudinal-ratio case.

boundary data,

$$\alpha_{\text{He}} = 8000 \text{ W/m}^2\text{K}. \quad (\text{B.8})$$

The temperature of the helium fluid is set to a constant value of $\vartheta_{\text{He}} = 4 \text{ K}$, which is identical to the initial temperature condition and the Dirichlet BC data on the isothermal boundaries of the coil model.

Bibliography

- [ARV02] M. ALEKSA, S. RUSSENSCHUCK, and C. VÖLLINGER. “Magnetic field calculations including the impact of persistent currents in superconducting filaments”. In: *IEEE Transactions on Magnetics* 38.2 (Mar. 2002), pp. 825–828. ISSN: 0018-9464. DOI: 10.1109/20.996213.
- [ADL00] P. R. AMESTOY, I. S. DUFF, and J.-Y. L’EXCELLENT. “Multifrontal parallel distributed symmetric and unsymmetric solvers”. In: *Computer Methods in Applied Mechanics and Engineering* 184.2–4 (Apr. 2000), pp. 501–520.
- [ASW96] T. APEL, A.-M. SÄNDIG, and J. R. WHITEMAN. “Graded Mesh Refinement and Error Estimates for Finite Element Solutions of Elliptic Boundary Value Problems in Non-smooth Domains”. In: *Mathematical Methods in the Applied Sciences* 19 (1996).
- [Apo15] A. APOLLONIO. “Machine Protection: Availability for Particle Accelerators”. PhD thesis. Wien: Technische Universität Wien, Mar. 2015.
- [ATL12] ATLAS COLLABORATION. “Observation of a new particle in the search for the Standard Model Higgs boson with the ATLAS detector at the LHC”. In: *Physics Letters B* 716.1 (2012), pp. 1–29.
- [AR04] B. AUCHMANN and S. RUSSENSCHUCK. “Coil end design for superconducting magnets applying differential geometry methods”. In: *IEEE Transactions on Magnetics* 40.2 (Mar. 2004), pp. 1208–1211. ISSN: 0018-9464. DOI: 10.1109/TMAG.2004.824710.
- [BS94] I. BABUŠKA and M. SURI. “The p and h-p Versions of the Finite Element Method, Basic Principles and Properties”. In: *SIAM Review* 36.4 (Dec. 1994), pp. 578–632.
- [BK07] B. W. BADER and T. G. KOLDA. “Efficient MATLAB computations with sparse and factored tensors”. In: *SIAM Journal on Scientific Computing* 30.1 (Dec. 2007), pp. 205–231. DOI: 10.1137/060676489.
- [BK+17] B. W. BADER, T. G. KOLDA, et al. *MATLAB Tensor Toolbox Version 3.0-dev*. Available online. Aug. 2017. URL: https://gitlab.com/tensors/tensor_toolbox.
- [BRS07] P. BAUER, H. RAJAINMAKI, and E. SALPIETRO. *EFDA Material Data Compilation for Superconductor Simulation*. EFDA CSU, Garching. 2007.
- [Boo+07] T. BOONEN et al. “Algebraic Multigrid for Implicit Runge-Kutta Discretizations of the Eddy Current Problem”. In: *IEEE Transactions on Magnetics* 43.4 (Apr. 2007), pp. 1265–1268.
- [Bor17] F. BORDRY. “LHC Status and Outlook”. In: *EPS-HEP 2017 conference*. 2017.
- [Bor+18] L. BORTOT et al. “A 2-D Finite-Element Model for Electro-Thermal Transients in Accelerator Magnets”. In: *IEEE Transactions on Magnetics* 54.3 (Mar. 2018).
- [Bos98] A. BOSSAVIT. *Computational Electromagnetism*. San Diego, USA: Academic Press, 1998.

-
- [Bot14] L. BOTTURA. “Cable Stability”. In: *CERN Yellow Report CERN-2014-005*, pp.401-451 5 (Dec. 17, 2014), pp. 401–405. DOI: 10.5170/CERN-2014-005.401. arXiv: 1412.5373v1 [physics.acc-ph].
- [Bra12] D. BRAESS. *Finite Elements*. Cambridge University Press, 2012. 384 pp.
- [BS08] S. BRENNER and R. SCOTT. *The Mathematical Theory of Finite Element Methods*. New York: Springer, 2008. ISBN: 978-0-387-75933-3.
- [Bru+04] O. S. BRUNING et al. *LHC Design Report Vol. 1: The LHC Main Ring*. Geneva: CERN, 2004.
- [BK13] W. BUCKEL and R. KLEINER. *Supraleitung – Grundlagen und Anwendungen*. Seventh. Weinheim, Germany: Wiley-VCH, 2013.
- [BDD21] J. BUNDSCHUH, L. A. M. D’ANGELO, and H. DE GERSEM. “Quasi-3-D Spectral Wavelet Method for a Thermal Quench Simulation”. In: *Journal of Mathematics in Industry* 11.17 (2021).
- [Can+06] C. CANUTO et al. *Spectral Methods – Fundamentals in Single Domains*. Scientific Computation. Berlin-Heidelberg, Germany: Springer, 2006.
- [CWW02] M. CLEMENS, M. WILKE, and T. WEILAND. “3-D Transient Eddy-Current Simulations Using FI²TD Schemes With Variable Time-Step Selection”. In: *IEEE Transactions on Magnetics* 38.2 (Mar. 2002), pp. 605–608.
- [CW01] M. CLEMENS and T. WEILAND. “Discrete Electromagnetism with the Finite Integration Technique”. In: *Progress In Electromagnetics Research* 32 (2001), pp. 65–87.
- [COM] COMSOL AB. *COMSOL Multiphysics®v. 5.4*. Stockholm, Sweden.
- [Cor+17] I. CORTES GARCIA et al. “Optimized Field/Circuit Coupling for the Simulation of Quenches in Superconducting Magnets”. In: *IEEE Journal on Multiscale and Multiphysics Computational Techniques* 2 (2017).
- [Cor20] I. CORTES GARCIA. “Mathematical Analysis and Simulation of Field Models in Accelerator Circuits”. PhD dissertation. Darmstadt, Germany: Technische Universität Darmstadt, 2020.
- [CDN18] E. CREUSÉ, P. DULAR, and S. NICAISE. “About the gauge conditions arising in Finite Element magnetostatic problems”. In: *Computers & Mathematics with Applications* 77.6 (Mar. 2018), pp. 1563–1582.
- [DCD20] L. A. M. D’ANGELO, J. CHRIST, and H. DE GERSEM. “Quasi-3D Discretization of Thermal Hot-Spot Propagation in Superconducting Models”. In: *IEEE Transactions on Applied Superconductivity* 30.4 (June 2020).
- [DD17] L. A. M. D’ANGELO and H. DE GERSEM. “Quasi-3D Finite-Element Method for Simulating Cylindrical Induction-Heating Devices”. In: *IEEE Journal on Multiscale and Multiphysics Computational Techniques* 2 (2017).
- [DD21] L. A. M. D’ANGELO and H. DE GERSEM. “Quasi-3D Magnetic Field Simulation of Superconducting Devices with Translational Symmetry”. In: *IET Science, Measurement & Technology* 15.3 (May 2021), pp. 319–327.
- [DSD19] L. A. M. D’ANGELO, Y. SPÄCK-LEIGSNERING, and H. DE GERSEM. “Electroquasistatic quasi-3D finite element simulation of a graded surge arrester”. In: *International Journal of Numerical Modelling: Electronic Networks, Devices and Fields* (2019).

-
- [DSD22] L. A. M. D'ANGELO, Y. SPÄCK-LEIGSNERING, and H. DE GERSEM. "Quasi-3D Magneto-Thermal Quench Simulation Scheme for Superconducting Accelerator Magnets". In: *IEEE Transactions on Applied Superconductivity* 32.6 (2022), pp. 1–5. DOI: 10.1109/TASC.2022.3159302.
- [DAn+22] L. A. M. D'ANGELO et al. "A Reduced Vector Potential Formulation for Superconducting Accelerator Magnets". In: *20th International IGTE Symposium 2022*. Graz University of Technology, Institute of Fundamentals and Theory in Electrical Engineering. Graz, Austria, Sept. 2022.
- [Das19] DASSAULT SYSTEMES. *CST Studio Suite – Electromagnetic Field Simulation Software*. Brochure. 2019.
- [DBH03] H. DE GERSEM, R. BELMANS, and K. HAMEYER. "Floating potential constraints and field-circuit couplings for electrostatic and electrokinetic finite element models". In: *COMPEL* 22.1 (2003), pp. 20–29.
- [Dul+98] P. DULAR et al. "A general environment for the treatment of discrete problems and its application to the finite element method". In: *IEEE Transactions on Magnetics* 34.5 (Sept. 1998), pp. 3395–3398.
- [DG19] P. DULAR and C. GEUZAINÉ. *GetDP Reference Manual*. University of Liège, Institut d'Électricité Montefiore. Liège, Belgium, July 2019.
- [Dun85] D. A. DUNAVANT. "High Degree Efficient Symmetrical Gaussian Quadrature Rules for the Triangle". In: *International Journal for Numerical Methods in Engineering* 21 (1985), pp. 1129–1148.
- [FD15] F. FAKHAR-IZADI and M. DEGHAN. "A spectral element method using the modal basis and its application in solving second-order nonlinear partial differential equations". In: *Mathematical Methods in Applied Sciences* 38 (2015), pp. 478–504. DOI: 10.1002/mma.3082.
- [GLD20] A. GALETZKA, D. LOUKREZIS, and H. DE GERSEM. "Data-Driven Solvers for Strongly Nonlinear Material Response". In: *International Journal for Numerical Methods in Engineering* 122.6 (Mar. 2020), pp. 1538–1562.
- [GR09] C. GEUZAINÉ and J.-F. REMACLE. "Gmsh: a three-dimensional finite element mesh generator with built-in pre- and post-processing facilities". In: *International Journal for Numerical Methods in Engineering* 79.11 (2009), pp. 1309–1331.
- [Gri16] F. GRILLI. "Numerical Modeling of HTS Applications". In: *IEEE Transactions on Applied Superconductivity* 26.3 (Apr. 2016).
- [GN07] M. GUPTA and S. G. NARASHIMHAN. *Legendre polynomials Triple Product Integral and lower-degree approximation of polynomials using Chebyshev polynomials*. Tech. rep. Pittsburgh, Pennsylvania: Carnegie Mellon University, May 2007.
- [Ham99] P. HAMMOND. "The Role of the Potentials in Electromagnetism". In: *ICS Newsletter* (June 1999).
- [Hau09] J. R. HAUSER. *Numerical Methods for Nonlinear Engineering Models*. The Netherlands: Springer, 2009.
- [He93] A. HE, ed. *Quench and Quench Protection for the SSC Collider Correctors*. Proceedings of International Conference on Particle Accelerators. Washington, DC, USA: IEEE, May 1993.

-
- [Jac98] J. D. JACKSON. *Classical Electrodynamics*. Third edition. Hoboken, NJ, USA: John Wiley & Sons, 1998.
- [Jan+21] M. JANITSCHKE et al. “A Simplified Approach to Simulate Quench Development in a Superconducting Magnet”. In: *IEEE Transactions on Applied Superconductivity* 31.5 (Aug. 2021).
- [Jor+12] H. V. JORKS et al. “Three-dimensional simulations of an induction motor including eddy current effects in core laminations”. In: *IET Science, Measurement and Technology* 6.5 (2012).
- [Kam12] H. KAMERLINGH-ONNES. “Further experiments with Liquid Helium G. On the electrical resistance of Pure Metals etc. VI. On the Sudden Change in the Rate at which the Resistance of Mercury Disappears”. In: *KNAW Proceedings* 14.2 (1912), pp. 818–821.
- [KL07] R. C. KIRBY and A. LOGG. “Efficient Compilation of a Class of Variational Forms”. In: *ACM Transactions on Mathematical Software* 33.3 (Aug. 2007).
- [KT99] D. KOMATITSCH and J. TROMP. “Introduction to the spectral element method for three-dimensional seismic wave propagation”. In: *Geophysical Journal International* 139.3 (Dec. 1999), pp. 806–822.
- [Kop09] D. A. KOPRIVA. *Implementing Spectral Methods for Partial Differential Equations – Algorithms for Scientists and Engineers*. Springer, 2009.
- [Let78] F. G. LETHER. “On the construction of Gauss-Legendre quadrature rules”. In: *Journal of Computational and Applied Mathematics* 4.1 (1978), pp. 47–52.
- [Loa00] C. F. V. LOAN. “The ubiquitous Kronecker product”. In: *Journal of Computational and Applied Mathematics* 123 (2000), pp. 85–100.
- [Mak80] J. MAKHOUL. “A Fast Cosine Transform in One and Two Dimensions”. In: *IEEE Transactions on Acoustics, Speech and Signal Processing* ASSP-28.1 (Feb. 1980).
- [MC95] J. B. MANGES and Z. J. CENDES. “A Generalized Tree-Cotree Gauge for Magnetic Field Computation”. In: *IEEE Transactions in Magnetics* 31.3 (May 1995).
- [MAT20] MATLAB. *version 9.8.0.1417392 (R2020a) Update 4*. Natick, Massachusetts: The MathWork Inc., 2020.
- [Mav92] C. MAVRIPLIS. *Adaptive Mesh Strategies for the Spectral Element Method*. Research rep. 189686. Hampton, VA, USA: NASA, July 1992.
- [Mur+94] J. MURATORE et al. “Quench Propagation Study for Full-Length RHIC Dipole Magnets”. In: *IEEE Transactions on Magnetics* 30.4 (July 1994), pp. 1726–1729.
- [ND96] A. NICOLET and F. DELINCÉ. “Implicit Runge-Kutta Methods for Transient Magnetic Field Computation”. In: *IEEE Transactions on Magnetics* 32.3 (May 1996), pp. 1405–1408.
- [OB90] J. T. ODEN and J. M. BASS. “New Developments in Adaptive Methods for Computational Fluid Dynamics”. In: *International Conference on Computational Methods for Applied Sciences and Engineering*. Ed. by R. GLOWINSKI and A. LICHNEWSKY. Philadelphia, USA: Society for Industrial and Applied Mathematics, 1990. Chap. 9, pp. 180–211.
- [Pat84] A. T. PATERA. “A Spectral Element Method for Fluid Dynamics: Laminar Flow in a Channel Expansion”. In: *Journal of Computational Physics* 54 (1984), pp. 468–488.

-
- [Pau97] C. PAUL. “Numerical Calculation of the Saturation Induced Field Errors in the Main Dipole of CERN’s future Large Hadron Collider”. PhD thesis. Technische Universität Graz, Sept. 1997.
- [PMS19] J. PIOTROWSKA, J. M. MILLER, and E. SCHNETTER. “Spectral methods in the presence of discontinuities”. In: *Journal of Computational Physics* 390 (Aug. 2019), pp. 527–547.
- [Poz14] C. POZRIKIDIS. *Introduction to Finite and Spectral Element Methods Using MATLAB*. Second Edition. CRC Press, 2014. ISBN: 978-1-4822-0915-0.
- [Qua17] A. QUARTERONI. *Numerical Models for Differential Problems*. Third Edition. Cham, Switzerland: Springer, 2017.
- [Qui19] C. QUIGG. “Dream Machines”. In: *Reviews of Accelerator Science and Technology* 10.1 (2019), pp. 3–12.
- [Rav+14] E. RAVAIOLI et al. “New, Coupling Loss Induced, Quench Protection System for Superconducting Accelerator Magnets”. In: *IEEE Transactions on Applied Superconductivity* 24.3 (June 2014).
- [Rav+16] E. RAVAIOLI et al. “Lumped-element dynamic electro-thermal model of a superconducting magnet”. In: *Cryogenics* 80.3 (Dec. 2016), pp. 346–356. ISSN: 0011-2275. DOI: 10.1016/j.cryogenics.2016.04.004.
- [Ren96] Z. REN. “Influence of the R.H.S. on the Convergence Behaviour of the Curl-Curl Equation”. In: *IEEE Transactions on Magnetics* 32.3 (May 1996).
- [RKL09] M. E. ROGNES, R. C. KIRBY, and A. LOGG. “Efficient Assembly of H(div) and H(curl) Conforming Finite Elements”. In: *SIAM Journal of Scientific Computing* 31.6 (2009).
- [RV10] E. ROSSEEL and S. VANDEWALLE. “Iterative Solvers for the Stochastic Finite Element Method”. In: *SIAM Journal of Scientific Computing* 32.1 (Feb. 2010), pp. 372–397.
- [Rüd+18] U. RÜDE et al. “Research and Education in Computational Science and Engineering”. In: *SIAM Review* 60.3 (2018), pp. 707–754.
- [Rus98] S. RUSSENSCHUCK, ed. *ROXIE: Routine for the Optimization of Magnet X-Sections, Inverse Field Calculation and Coil End Design – First International ROXIE Users Meeting and Workshop*. 1998.
- [Rus10] S. RUSSENSCHUCK. *Field Computation for Accelerator Magnets*. Weinheim: Wiley-VCH Verlag, 2010. ISBN: 978-3-527-40769-9.
- [SWS22] E. SCHNAUBELT, M. WOZNIAK, and S. SCHÖPS. “Thermal Thin Shell Approximation for Finite Element Quench Simulation”. In: *Superconductor Science and Technology* (2022).
- [SZ19] D. SCHOERLING and A. V. ZLOBIN, eds. *Nb₃Sn Accelerator Magnets – Designs, Technologies and Performance*. Springer Open, 2019. ISBN: 978-3-030-16117-0.
- [SDW13] S. SCHÖPS, H. DE GERSEM, and T. WEILAND. “Winding functions in transient magnetoquasistatic field-circuit coupled simulations”. In: *COMPEL* 32.6 (2013), pp. 2062–2082.
- [Sch10] J. N. SCHWERG. “Numerical Calculation of Transient Field Effects in Quenching Superconducting Magnets”. PhD thesis. Berlin: Fakultät IV – Elektrotechnik und Informatik, Technische Universität Berlin, 2010.

-
- [SJ17] J. P. SENEAL and W. JI. “Approaches for mitigating over-solving in multiphysics simulations”. In: *International Journal for Numerical Methods in Engineering* 112.6 (Feb. 2017), pp. 503–528. DOI: 10.1002/nme.5516.
- [Sha15] R. G. SHARMA. *Superconductivity – Basics and Applications to Magnets*. Springer Series in Materials Science 214. Cham, Switzerland: Springer, 2015.
- [STW11] J. SHEN, T. TANG, and L.-L. WANG. *Spectral Methods – Algorithms, Analysis and Applications*. Springer Series in Computational Mathematics. Springer, 2011. ISBN: 978-3-540-71040-0.
- [SDR92] N. J. SIMON, E. S. DREXLER, and R. P. REED. *Properties of Copper and Copper Alloys at Cryogenic Temperatures*. National Institute of Standards and Technology, Feb. 1992.
- [SBG96] B. F. SMITH, P. E. BJØRSTAD, and W. D. GROPP. *Domain Decomposition: Parallel Multilevel Methods for Elliptic Partial Differential Equations*. Cambridge University Press, 1996. ISBN: 978-0-521-49589-9.
- [Ste+19] J. STECKERT et al. “Application of the New Generic Quench Detection System for LHC’s 11 T Dipole Magnet”. In: *IEEE Transactions on Applied Superconductivity* 29.5 (Aug. 2019).
- [Ten+88] H. H. J. TEN KATE et al. “Development of a Superconducting Protection Switch for the HERA P-ring: Design Study and Demonstration Models”. In: *IEEE Transactions on Magnetics* 24.2 (Mar. 1988), pp. 1178–1181.
- [Ten13] H. TEN KATE. “Superconducting Magnets Quench Propagation and Protection”. In: *CERN Accelerator School on Superconductivity for Accelerators*. Erice, 2013.
- [TTS18] D. TOMMASINI, F. TORAL, and D. SCHÖRLING. *Cost model for dipole magnet*. Grant agreement No. 654305, European Circular Energy-Frontier Collider Study. Oct. 2018.
- [Tro+19] J. F. TROITINO et al. “3-D Thermal-Electric Finite Element Model of a Nb₃Sn Coil During a Quench”. In: *IEEE Transactions on Applied Superconductivity* 29.5 (Aug. 2019).
- [Tur+56] M. J. TURNER et al. “Stiffness and Deflection Analysis of Complex Structures”. In: *Journal of the Aeronautical Sciences* 23.9 (Sept. 1956), pp. 805–854.
- [VD09] G. VAN ROSSUM and F. L. DRAKE. *Python 3 Reference Manual*. Scotts Valley, CA: CreateSpace, 2009. ISBN: 1441412697.
- [VDI10] VDI-GESELLSCHAFT VERFAHRENSTECHNIK UND CHEMIEINGENIEURWESEN, ed. *VDI Heat Atlas*. Second Edition. Berlin-Heidelberg, Germany: Springer, 2010.
- [Ver95] A. P. VERWEIJ. “Electrodynamics of Superconducting Cables in Accelerator Magnets”. PhD thesis. Universiteit Twente, 1995.
- [VAR00] C. VÖLLINGER, M. ALEKSA, and S. RUSSENSCHUCK. “Calculation of persistent currents in superconducting magnets”. In: *Physical Review Accelerators and Beams* 3.12 (2000), p. 122402. ISSN: 2469-9888. DOI: 10.1103/PhysRevSTAB.3.122402.
- [Wil83] M. N. WILSON. *Superconducting Magnets*. New York, USA: Oxford University Press, 1983. ISBN: 0-19-854810-9.
- [ZTT05] O. C. ZIENKIEWICZ, R. L. TAYLOR, and J. Z. THU. *The Finite Element Method: Its Basis & Fundamentals*. Sixth edition. Burlington, MA, USA: Elsevier Butterworth-Heinemann, 2005.

Danksagung

An dieser Stelle möchte ich all jenen würdigend danken, die zum Gelingen dieser Dissertation beigetragen haben.

Finanziell wurde diese Arbeit unterstützt von dem Bundesministerium für Bildung und Forschung der Bundesrepublik Deutschland im Rahmen des Projektes „Quenchsimulation für Supraleitende Magnete: Steigerung der Auflösung in Zeit und Raum“ (BMBF-05P19RDRB1), von der Graduiertenschule Computational Engineering der Technischen Universität Darmstadt, und dem Graduiertenkolleg 2128 „Accelence: Beschleunigerphysik und -technologie für Teilchenbeschleuniger mit Energierückgewinnung“ der Deutschen Forschungsgesellschaft.

Mein tiefster Dank gilt meinem Doktorvater Prof. Dr.-Ing. Herbert De Gersem, der die Bearbeitung dieses spannenden Themas überhaupt möglich gemacht hat und mich bereits im Jahr 2016 im Rahmen meiner Bachelorarbeit mit quasi-3D Methoden bekannt gemacht hat. Seit dieser Zeit hat er mich unentwegt auf meinem akademischen Weg unterstützt und mir so das Sammeln vieler wertvoller Erfahrungen im akademischen Bereich sowie für meine Persönlichkeitsentwicklung ermöglicht.

Ein großer Dank geht an Dr.-Ing. Yvonne Späck-Leigsnering, die mir während der schwierigen Zeit der Pandemie als Zweitbetreuerin zur Seite sprang. Ihre praktischen Sichtweisen eröffneten mir neue Perspektiven, die meine Arbeit positiv geprägt haben.

Ich danke Elisabeth Horz, Jonas Bundschuh, Melina Merkel und Erik Schnaubelt, die Teile meiner Dissertation gegengelesen haben. Ihre Kritiken und Verbesserungsvorschläge waren sehr hilfreich. Weiterhin danke ich allen Kolleginnen und Kollegen am Institut TEMF für eine äußerst angenehme und produktive Arbeitsatmosphäre und für die fachlichen wie nicht-fachlichen Intermezzi in der Kaffeeküche.

Neben finanzieller und fachlicher Unterstützung wäre diese Dissertation sicherlich nicht so reibungslos vonstatten gegangen, hätte ich nicht auch noch umfassende emotionale Unterstützung meiner Familie und meines Freundeskreises genossen. Hierbei danke ich insbesondere meiner Mutter Lucia Höser, die in mir überhaupt die Begeisterung für Bildung pflanzte und mich bei jedem Schritt bis hin zur Promotion zu 100% unterstützte, sowie ihrem Ehemann Kurt Höser.

Evelyn Kary, Elisabeth Horz, Rahel Schmitz, Stanislav Macko und Melina Merkel danke ich für ihre herzerfrischende Freundschaft und mentale Unterstützung in dieser anspruchsvollen Zeit, ihr entgegengebrachtes Verständnis insbesondere in den intensiven Phasen meiner Arbeit, sowie ihre beflügelnde Wertschätzung für mich und meine Forschung.

Mein herzlichster Dank gilt schließlich meinem Partner Stefan Patsch, der meine Ambitionen von Anfang an unterstützte und in allen Höhen und Tiefen dieser Dissertation mein Fels in der Brandung war.

Laura Anna Maria D'Angelo
Darmstadt, im Januar 2023

Scientific Contributions

Scientific Publications

1. Laura A. M. D'Angelo, Yvonne Späck-Leigsnering and Herbert De Gersem: "Quasi-3D Magneto-Thermal Quench Simulation Scheme for Superconducting Accelerator Magnets". In: *IEEE Transactions on Applied Superconductivity*, vol. 32, no. 6, 2022.
2. Laura A. M. D'Angelo and Herbert De Gersem: "Quasi-3D Magnetic Field Simulation of Superconducting Devices with Translational Symmetry". In: *IET Science, Measurement & Technology*, vol. 15, pp. 319-327, 2021.
3. Jonas Bundschuh, Laura A. M. D'Angelo and Herbert De Gersem: "Quasi 3-D Spectral Wavelet Method for a Thermal Quench Simulation". In: *Journal of Mathematics in Industry*, vol. 11, no. 17, 2021.
4. Herbert De Gersem and Laura A. M. D'Angelo: "Modeling Skew by Single- and Multi-Slice 2-D Machine Models". In: *IEEE Transactions on Magnetics*, vol. 57, no. 6, 2021.
5. Laura A. M. D'Angelo, Jonas Christ and Herbert De Gersem: "Quasi-3D Discretization of Thermal Hot-Spot Propagation in Superconducting Models". In: *IEEE Transactions on Applied Superconductivity*, vol. 30, no. 4, 2020.
6. Laura A. M. D'Angelo, Zeger Bontinck, Sebastian Schöps and Herbert De Gersem: "Robust Optimization of a Permanent-Magnet Synchronous Machine Considering Uncertain Driving Cycles". In: *NAFEMS – Zeitschrift für numerische Simulationsmethoden und angrenzende Gebiete*, vol. 1, pp. 71-80, 2020.
7. Laura A. M. D'Angelo, Yvonne Späck-Leigsnering and Herbert De Gersem: "Electroquasistatic Quasi-3D Finite Element Simulation of a Graded Surge Arrester". In: *International Journal of Numerical Modelling: Electronic Networks, Devices and Fields*, 2019.
8. Laura A. M. D'Angelo and Herbert De Gersem: "Quasi-3-D Finite-Element Method for Simulating Cylindrical Induction-Heating Devices". In: *IEEE Journal on Multiscale and Multiphysics Computational Techniques*, vol. 2, pp. 134-141, 2017.

Conference Contributions

1. Laura A. M. D'Angelo, Yvonne Späck-Leigsnering and Herbert De Gersem: "Quasi-3D Simulation Approach for Quench Simulation of Superconducting Magnets". In: *28th International Conference on Magnet Technology (MT28)*. Aix-en-Provence, France, September 2023. Accepted for presentation.
2. Laura A. M. D'Angelo, Yvonne Späck-Leigsnering and Herbert De Gersem: "Quasi-3D Method for Quench Simulation of Superconducting Coils". In: *24th International Conference on*

the Computation of Electromagnetic Fields (COMPUMAG 2023). Kyoto, Japan, May 2023. Accepted for presentation.

3. Laura A. M. D'Angelo, Yvonne Späck-Leigsnering, Herbert De Gersem, Nicolas Marsic, Bernhard Auchmann, Sebastian Schöps, Michał Maciejewski and Jasmin Smajic: "Quasi-3D Magneto-Thermal Quench Simulation of Superconducting Magnet Coils". In: *Kleinheubacher Tagung 2022*. Miltenberg, Germany, September 2022.
4. Laura A. M. D'Angelo, Yvonne Späck-Leigsnering and Herbert De Gersem: "A Reduced Vector Potential Formulation for Superconducting Accelerator Magnets". In: *20th International IGTE Symposium 2022 (IGTE 2022)*. Graz, Austria, September 2021.
5. Laura A. M. D'Angelo and Herbert De Gersem: "Quasi-3D Magneto-Thermal Quench Simulation of Superconducting Magnets". In: *27th International Conference on Magnet Technology (MT27)*. Fukuoka, Japan, November 2021.
6. Laura A. M. D'Angelo and Herbert De Gersem: "Quasi-3D Magnetic Field Simulation of Superconducting Devices with Translational Symmetry". In: *European Consortium for Mathematics in Industry 2021 (ECMI)*. Wuppertal, Germany, April 2021.
7. Laura A. M. D'Angelo, Jonas Christ and Herbert De Gersem: "Quasi-3D Thermal Simulation of Quench Propagation of Superconducting Magnets". In: *26th International Conference on Magnet Technology (MT26)*. Vancouver, Canada, September 2019.
8. Laura A. M. D'Angelo, Yvonne Späck-Leigsnering and Herbert De Gersem: "Quasi-3D Finite-Element Model of a High-Voltage Surge Arrester". In: *11th International Symposium on Electric and Magnetic Fields (EMF)*. Darmstadt, Germany, September 2018.

Awards

1. Laura A. M. D'Angelo, Yvonne Späck-Leigsnering and Herbert De Gersem: "Quasi-3D Magneto-Thermal Quench Simulation of Superconducting Magnet Coils". In: *Kleinheubacher Tagung 2022*. Miltenberg, Germany, September 2022. Awarded with Young Scientist Award and Young Scientist Best Paper Award (1st place).

Supervised Student Theses

1. Laurenz Ziegler: "Thin-Shell Approximation of Insulation Layers in Superconducting Coils". Master's Thesis. Technische Universität Darmstadt, 2022.
2. Sven Dunkel: "Finite-Element Simulation of a Magnetocaloric Refrigeration System". Bachelor's Thesis. Technische Universität Darmstadt, 2020.
3. Jonas Bundschuh: "Quasi-3D Quench Simulation Using a Spectral Wavelet Method". Master's Thesis. Technische Universität Darmstadt, 2020.
4. Jan-Magnus Christmann: "Thermal Modeling and Uncertainty Quantification for Superconducting Cables". Bachelor's Thesis. Technische Universität Darmstadt, 2020.
5. Jonas Christ: "Quasi-3D Thermal Simulation of Quench Propagation of Superconducting Magnets". Bachelor's Thesis. Technische Universität Darmstadt, 2019.